DEVELOPMENT OF HIGH-EFFICIENCY SILICON SOLAR CELLS AND MODELING THE IMPACT OF SYSTEM PARAMETERS ON LEVELIZED COST OF ELECTRICITY

A Dissertation
Presented to
The Academic Faculty

by

Moon Hee Kang

In Partial Fulfillment
of the Requirements for the Degree
Doctor of Philosophy in the
School of Electrical and Computer Engineering

Georgia Institute of Technology
May 2013

DEVELOPMENT OF HIGH-EFFICIENCY SILICON SOLAR CELLS AND MODELING THE IMPACT OF SYSTEM PARAMETERS ON LEVELIZED COST OF ELECTRICITY

Approved by:

Dr. Ajeet Rohatgi, Advisor
School of Electrical and Computer Engineering
Georgia Institute of Technology

Dr. Miroslav Begovic
School of Electrical and Computer Engineering
Georgia Institute of Technology

Dr. Thomas Gaylord
School of Electrical and Computer Engineering
Georgia Institute of Technology

Dr. Shreyes Melkote
School of Mechanical Engineering
Georgia Institute of Technology

Dr. Bernard Kippelen
School of Electrical and Computer Engineering
Georgia Institute of Technology

Date Approved: March 26, 2013

This work is dedicated to

My parents
Jongkeun Kang and Yeongheui Ko
for their love, support, and patience

ACKNOWLEDGEMENTS

"See, I have refined you, though not as silver; I have tested you in the furnace of affliction." (Isaiah 48:10)

I am most grateful for God who created the world and give permanent love to us. I also would like to thank from the bottom of my heart to my advisor, Dr. Ajeet Rohatgi, for giving me this research opportunity as well as financial support. I really appreciate his valuable mentoring and advising on research as well as communication skills. He has encouraged me to learn how to form well organized ideas and express my ideas. I also would like to thank Dr. Thomas Gaylord and Dr. Bernard Kippelen for serving my thesis reading committee and insightful comments and suggestions.

I also acknowledge the gratitude to my former and current colleagues at University Center of Excellence for Photovoltaics Research and Education (UCEP). It was my great pleasure to work at UCEP, and I never regretting time here. Special thanks to Dr. Dongseop Kim and Dr. Abasifreke Ebong for their support and valuable discussions. I am grateful to Dean Sutter, Ken Lamborn, Kenny Trotman, and Erik Westman for their extensive assistance with equipment maintenance. Thanks to Carla for her warm motherly care. Thanks to Aditya Kapoor, Ajay Upadhyaya, Dr, Alan Ristow, Dr. Arnab Das, Brian Rounsaville, Eunhwan Cho, Francesco Zimbardi, Dr. Ian Cooper, James Keane, Jiun-Hong Lai, John Renshaw, Keith Tate, Kenta Nakayashiki, Kyung Sun Ryu, Malka Kadish, Dr. Manav Shoeran, Dr. Pranav Anbalagan, Ricky Chen, Dr. Rishi Ramanathan, Sean Riordan, Steven Ning, Dr. Vijay Yelundur, Vijaykumar Upadhyaya,

and Dr. Young-Woo Ok for their true friendship, generous supports, and good teamwork. Special thank to Dr. Vichai Meemongkolkiat for his training and discussions during the early year of my Ph.D.

Special thanks to Dr. Junegie Hong, former CTO of SiXtron Inc., for his generous supports and friendship. Many of my research projects were done under the support from the SiXtron. Special also thanks to Saehan Presbyterian church for their sincere prayer, which has encouraged me when I have trouble.

TABLE OF CONTENTS

LIST OF TABLES

Page

LIST OF FIGURES

Page

LIST OF SYMBOLS AND ABBREVIATIONS

Al-BSF	Aluminum-back-surface field
ALD	Atomic layer deposition
AM	Air mass
AR	Antireflection
a-Si	Amorphous Si
BOS	Balance of system
BSR	Back surface reflection
BSRV	Back surface recombination velocity
c-Si	Crystalline silicon
Cz	Czochralski
DOE	Department of Energy
E_g	Bandgap energy
EVA	Ethylene vinyl acetate
FF	Fill factor
FSRV	Front surface recombination velocity
FTIR	Fourier transform infrared spectroscopy
FZ	Float zone
γ	Temperature coefficient
IQE	Internal quantum efficiency
IR	Infrared
I_{sc}	Short circuit current
ITC	Investment tax credit

J_{oe}	emitter saturation current
k	Extinction coefficient
LCOE	Levelized cost of electricity
LID	Light-induced degradation
MACRS	Modified accelerated cost recovery system
mc	Multi crystalline
n	Refractive index
NREL	National Renewable Energy Laboratory
O&M	Operation and maintenance
PECVD	Plasma-enhanced chemical-vapor deposition
PERC	Passivated emitter rear contact
PERL	Passivated emitter with rear locally diffused
PL	Photoluminescence
PV	Photovoltaics
Q_{fb}	Flat-band charge density
QSSPC	quasi-steady-state photo-conductance
R_{se}	Series resistance
R_{sh}	Shunt resistance
RTP	Rapid thermal processing
SAM	System Advisor Model
SEM	Scanning electron microscope
SIMS	Secondary ion mass spectrometry
SRV	Surface recombination velocity
STC	Standard Test Condition
T_{iwoct}	Irradiance weighted operating cell temperature

TMA	Trimethylaluminum
V_{oc}	Open circuit voltage
WACC	Weight average cost of capital

SUMMARY

Since the beginning of the industrial revolution, humans have primarily relied on fossil fuels to satisfy the rapid increase in energy demand. However, global warming caused by increased carbon dioxide emission due to burning of fossil fuels can lead to abnormal climate changes and natural disasters. Since carbon dioxide emission and corresponding global warming mostly comes from burning the fossil fuels, there is an urgent need to develop a new eco-energy source portfolio to replace fossil fuels. Among the various energy options available today, photovoltaics (PV) is most promising because solar energy is free, unlimited, and not localized, and solar cells can convert it into electricity with no undesirable impact on the environment. The surface of Earth receives about 1.2×10^{17} W power while the world energy consumption is ~1.1×10^{17} kWh/yr, indicating that incident sunlight on our globe in less than one hour equal to the world energy consumption for the whole year. In addition, PV produces no noise pollution, can be installed at the point of use to eliminate transmission losses, matches the utility load profile for peek shaving, and is modular so it can be scaled up to any size on the as-needed basis.

In spite of the many advantages listed above, PV accounts for less than 0.2% of the US portfolio for electricity generation because cost of electricity from PV is still higher than the current market price of electricity. Ultimate goal of PV is to reach grid parity where the price of electricity from PV in a given region is equal to or lower than the market price of electricity. In 2012, the installed system cost of a commercial-scale PV system was about $3/W which translates into a levelized cost of electricity (LCOE) in the range

of 10–20¢/kWh depending on the incident sunlight or the solar insolation. Therefore, current price of electricity from PV in most countries is still higher than the market price of electricity but is getting very close to grid parity. Therefore, further reduction is required in module or balance of system (BOS) cost to attain grid parity.

Overall objective of this thesis is to conduct silicon (Si) material and device research that can lead to low-cost high-efficiency solar cells. This should reduce both the module and BOS costs. The specific technical objectives deal with improving the optical and electrical performance of Si solar cells through process optimization, device modeling, clever cell design, fundamental understanding, and minimization of loss mechanisms. This is accomplished in the first five tasks of this thesis. In addition, another major objective is to develop cost and technology roadmaps by defining the right intersection of module cost and efficiency that can lead to grid parity in different parts of the world. Therefore, in the final chapters, detailed cost analysis is performed to quantify the impact of key system and financial parameters on the LCOE along with development of analytical models to assess the premium associated with efficiency, temperature coefficient, BOS cost, and incident sunlight or the solar insolation.

In the first task (Chapter 3) of this thesis, attempt is made to develop a new low-cost and safe dielectric material which can be used for antireflection (AR) coating as well as emitter surface passivation film. Plasma-enhanced chemical-vapor deposition (PECVD) of SiN_x film is widely used for fabrication of commercial Si solar cells. SiN_x film provides excellent surface passivation on phosphorus-doped emitters because of high positive-charge density. However, the deposition of SiN_x film typically requires highly pyrophoric and toxic silane (SiH_4) gas. This requires extensive care in handling, storage,

and transport and results in significant increase in cost. To eliminate the expense of storage and handling of silane, SiXtron Advanced Materials Inc. developed a novel silane-free apparatus and a solid polymer source for SiN_x deposition which contains atomic sources for silicon, carbon, and hydrogen. This allows deposition of SiC_xN_y films of different compositions by adjusting the source composition and the accompanying ammonia (NH_3) flow rate during the deposition. A detailed characterization and analysis of SiC_xN_y films was performed along with their impact on the Si solar cell performance. The ratio of carbon to nitrogen (C/N), hydrogen content, refractive index, and extinction coefficient of the SiC_xN_y films were found to decrease with the increase in the NH_3 flow rate. High surface charge density and hydrogen concentration of SiC_xN_y films provided comparable surface passivation and emitter saturation current density (J_{oe}) values on a 45 Ω/sq emitter cells. However, J_{oe} values were found to be slightly higher on high performance 80 Ω/sq emitter, resulting in 11 mV loss in open circuit voltage (V_{oc}) and ~0.2% loss in cell efficiency. Although there is a small tradeoff in efficiency at the high-end, the solid polymer source for SiC_xN_y deposition provides considerable safety and cost benefits compared to SiN_x films grown by silane gas.

Second task (Chapter 4) involved the investigation of bulk lifetime and efficiency degradation under illumination in boron-doped Czochralski (Cz) solar cells coated with conventional SiN_x and SiC_xN_y AR coatings. This light-induced degradation (LID) phenomenon is well known and is attributed to the formation of boron (B) and oxygen (O) complexes under illumination which leads to a factor of 2–5 reduction in bulk lifetime and as a consequence 0.2–0.6% loss in absolute cell efficiency. Limited data in the literature shows that carbon (C) in Si may retard LID because C likes to form

complexes with oxygen which may reduce the concentration of B-O complexes. Therefore, possible injection of C from the SiC_xN_y AR coating into the bulk Si was examined during high temperature deposition and contact firing by complete fabrication and analysis of commercial-ready B-doped Cz cells coated with conventional SiN_x coating as well as the novel SiC_xN_y films. LID in cell performance is generally examined after 24 hours of one Sun illumination because it saturates after that. It was found that SiC_xN_y-coated B-doped Cz solar cells indeed suffer less light-induced efficiency degradation compared to the conventional SiN_x-coated solar cells, which have no source of additional carbon. Traditional SiN_x-coated solar cells suffered an average loss of 0.3% in absolute efficiency due to LID compared to 0.1% efficiency for the SiC_xN_y-coated solar cells. PC1D device simulations showed that the observed efficiency loss is entirely consistent with the measured lower light-induced bulk-lifetime degradation from 250 to 130 μs in the SiC_xN_y-coated cells compared to the SiN_x-coated cells where bulk lifetime dropped to 74 μs.

Third task (Chapter 5) dealt with the investigation of possible improved performance of SiC_xN_y AR-coated solar cells under low illumination due to the observed higher shunt resistance (R_{sh}). Theoretical calculations were performed to demonstrate how and why R_{sh} value < 30 Ω can reduce the cell efficiency at lower solar insolation. It was found that cells coated with carbon-containing SiC_xN_y film have much higher R_{sh} value after contact firing compared to the carbon-free SiN_x film. In commercial solar cells, screen-printed Ag grid contacts are fired through the SiN_x AR coating. It is well known that this leads to the formation of Ag crystallites in the contact interface. Since junctions are quite shallow (< 0.5 μm), bigger crystallites often can lead to junction shunting. Therefore, contact

interface was examined by scanning electron microscope (SEM) and showed that the size of Ag crystallites at the contact interface were smaller in the case of carbon-containing SiC_xN_y AR coating, which reduced the parasitic shunting in the cell (high R_{sh} value). The exact reason for smaller crystallites is not well understood at this time. R_{sh} of SiC_xN_y-coated 239 cm^2 cells was found to be generally above 60 Ω compared to the SiN_x-coated cells, which averaged around 23 Ω. Model calculations and detailed cell analysis on the basis of higher R_{sh} value revealed and quantified the improved low-light performance of SiC_xN_y-coated cells. This makes up for the slightly lower starting efficiency of SiC_xN_y-coated cells due to higher J_{oe} compared to the SiN_x-coated cells. Threshold for R_{sh} was found in this study which showed that the impact of R_{sh} on low illumination efficiency decreases rapidly for $R_{sh} \geq 30$ Ω.

Fourth task (Chapter 6) in this thesis involved optimization of refractive index (n) and thickness of the conventional SiN_x based AR coating to provide best performance under a glass module. It is important to note that optimum index and thickness of AR coating could be different for Si solar cells tested in air and under glass. This is because n = 1 for air while glass has an index of 1.5. Generally a higher index film is preferred under glass, but higher index SiN_x films show considerable absorption. Degree of absorption can shift the optimum index under glass. The performance of various SiN_x films was investigated by a combination of geometrical ray tracing simulation program Sunrays and widely used PC1D device modeling program. Encapsulation loss is defined as loss in cell efficiency when it is moved from air ambient to under a glass cover. Better index match with glass will reduce the encapsulation loss. Simulations showed that SiN_x film with n = 2.03 and thickness of 78 nm provides the highest cell efficiency in air as well as under glass/EVA

(ethylene vinyl acetate) encapsulation for the pyramid textured Si solar cells. Even though index of 2.4 has the best match with glass (n = 1.5), it results in lower encapsulation cell efficiency. This is because a cell coated with an index of 2.4 SiN_x has a much lower starting efficiency in air due to the higher absorption and reflection. Identical optical analysis for planar cells showed that n = 2.20 and thickness of 68 nm gives the highest encapsulated cell efficiency.

Fifth task (Chapter 7) in this thesis involved passivation of Si surface with Al_2O_3 films grown by atomic layer deposition (ALD). Lower surface recombination velocity (SRV) is highly desirable for better cell performance. Deposition and annealing conditions for ALD Al_2O_3 films on Si were investigated for achieving stable and high-quality passivation for commercial ready solar cells. Recently, it has been reported that ALD Al_2O_3 can provide excellent passivation on p-type Si surface due to high negative charge, which creates an accumulation layer at the p-type Si surface to reduce recombination. This task shows that plasma-assisted ALD Al_2O_3 provides excellent surface passivation after optimized deposition, annealing, and firing. SRV of 57 cm/s was obtained after annealing and 150 cm/s after firing cycle on a textured Cz wafer which is superior to the traditional SiO_2 films on textured surfaces. In this task, commercial-ready screen-printed n^+-p Cz solar cells with textured back were fabricated with plasma-assisted ALD Al_2O_3 coating on p-surface and compared with the SiO_2 passivated solar cells. All these cells had local aluminum-back-surface field. About 0.9% absolute efficiency gain was observed for textured-back n^+-p cells with using plasma-assisted ALD Al_2O_3 compared to textured-back SiO_2 passivated cells. Such dielectric passivated p-type cells are generally fabricated with planar backs for higher efficiency where the absolute efficiencies is much

higher and the gap between Al_2O_3 and SiO_2 passivated cells is much smaller. This study shows that for textured-back n^+-p-p^+ solar cells, Al_2O_3 film is far superior to the SiO_2 film. In the case of n-base p^+-n-n^+ cells, textured boron-doped p^+ emitter was passivated with both Al_2O_3 and SiO_2, and the Al_2O_3passivated cells showed ~0.3% higher efficiency with maximum approaching 20%.

The above five tasks were conducted to improve Si solar cell performance by enhancing the optical and electrical properties of cells. The final task (Chapter 8, 9) involves the development and use of various cost models to assess the economical impact of cell efficiency enhancement on module cost and LCOE. Higher-efficiency modules not only produce more power, but they also reduce the BOS cost by decreasing the installation cost and the area of a given size (kW) system. However, it is also important to know how much more one should pay for higher-efficiency modules without increasing the LCOE. This is important when customers are faced with the choice of different PV modules, like thin films and Si with very different cost, temperature coefficients, and efficiencies. In this task, an analytical model was developed to provide a guide answer for this. Calculations from this model showed that a $1/W 16% efficient Si module is equivalent to a $0.86/W 14% efficient module as well as $1.11/W 18% efficient Si module because all three modules result in the same installed system cost and LCOE. Notice that lower efficiency modules cost less because of higher BOS cost. In addition, the analytical model was extended to incorporate the difference in temperature coefficient for efficiency degradation in order to compare different cell technologies. Model calculations were performed to show that in a hot climate like Phoenix, a $1/W 16% Si

module is equivalent to $0.83/W 12% CdTe, $0.77/W 12% CIGS, and $0.42/W 9% a-Si module resulting in same LCOE.

LCOE is the most important parameter to assess the cost effectiveness of a PV system. Ultimate goal of PV is to attain LCOE value equal to or lower than the current market price of electricity in a given location (grid parity). LCOE is dependent on the accuracy of multiple inputs which makes it challenging to assess the correct value. Therefore, extensive PV system modeling was conducted in this research to quantify the sensitivity and impact of key system parameters (installed system cost, BOS cost, module efficiency, operating performance loss, module cost, and system lifetime) as well as financial parameters (loan fraction, interest rate, and depreciation) on the value of LCOE. In addition, it is shown what installed system cost is required to attain grid parity in different parts of US and the world. For example, calculations show that the installed PV system cost needs to fall below $3/W to start encroaching grid parity in most regions. Certain locations like Denmark, Germany, and Hawaii, PV is already below grid parity today because of much higher price of electricity. It is shown that installed system cost of $2.8/W, $2.3/W, and $1.9/W is required to attain grid parity at LCOE of 10¢/kWh in Phoenix, Atlanta, and Detroit, respectively, due to very different solar insolation. Finally, calculations showed that to reach the grid parity in the entire US without incentives, installed system cost should be $1.25/W, which also happens to be the goal of SunShot initiative by 2020.

The objective of this thesis was to develop low-cost high-efficiency Si solar cells which are at the right intersection of cost and performance. The objective was addressed and achieved by improving the optical performance and electrical performance of Si solar

cells through process optimization, device modeling, clever cell design, fundamental understanding, and minimization of loss mechanisms. To improve the optical performance of solar cells, ray tracing and device simulation programs were used to find optimum index and thickness of SiN_x based AR coating under glass module. This should increase module power at no additional cost. Electrical performance of cell was improved by using the ALD Al_2O_3 passivation film. Optimization of deposition and annealing conditions of ALD Al_2O_3 film resulted in about 0.9% absolute efficiency gain for textured-back n^+-p cells compared to textured-back SiO_2 passivated cells. Light-induced degradation and low-illumination efficiency loss was improved by implementing carbon-containing SiC_xN_y AR coating with no additional processing cost in conjunction with the benefit of safety and material transport cost. Solar cells with carbon-containing AR coating showed ~0.2% lower light-induced efficiency degradation as well as ~0.2% lower efficiency loss at low illumination. Both these attributes will improve the energy output of the module. Finally, detailed cost analysis and PV system calculations were performed to provide guidelines and roadmaps for attaining grid parity with PV. More specifically, importance of efficiency was quantified and contour plots were generated to define the right intersection of cost and efficiency for various technologies to attain a desired LCOE.

CHAPTER 1

INTRODUCTION AND RESEARCH OBJECTIVES

1.1 Statement of the problem

Since the beginning of the industrial revolution, humans have primarily relied on fossil fuels to satisfy the rapid increase in energy demand. However, global warming caused by increased carbon dioxide emission due to burning of fossil fuels can lead to abnormal climate changes and natural disasters. In 1997, Kyoto Protocol [1] was adopted to tackle global warming by reducing the emission of greenhouse gases (Figure 1.1) such as carbon dioxide (CO_2), methane (CH_4), nitrous oxide (N_2O), and fluorinated gases (F-gases).

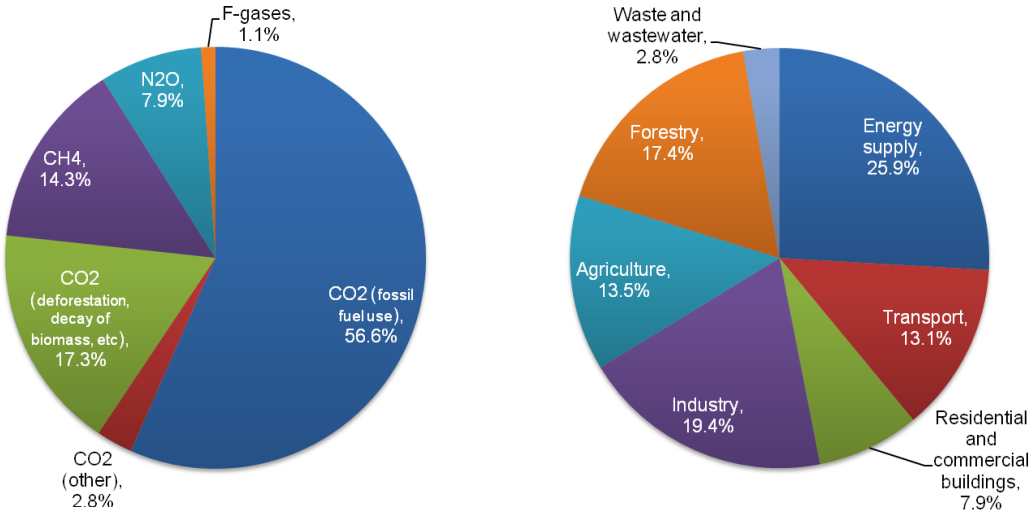

Figure 1.1: Global greenhouse gas emissions and emissions by sector [2].

Table 1.1 shows quantitatively the emission of greenhouse gases from the various promising energy sources. Notice that photovoltaics (PV) produces essentially zero greenhouse gases when generating energy and only 5.3 gC/kWh emission during the production of PV products. In addition, sunlight is the fuel for PV which is free, unlimited, and not localized in any part of the world. Nuclear also produces zero greenhouse gases when generating energy, but the projected exhaustion time of uranium is only 115 years (Table 1.2), in addition to, safety issues and very long lead time for building a nuclear power plant.

Table 1.1: Pollutant emission factors for the total and non-generating portion of the fuel cycle [3, 4].

Energy Source	SO_x (gSO_x/kWh)	NO_x (gNO_x/kWh)	C in CO_2 (gC/kWh)	C in CO_2 from non-generating portion of fuel cycle (gC/kWh)
Coal	3.4	1.8	322.8	50
Oil	1.7	0.88	258.5	50
Natural Gas	0.001	0.9	178	30
Nuclear	0.03	0.003	7.8	7.8
Photovoltaics	0.02	0.007	5.3	5.3

Table 1.2: Projected exhaustion of fuel reserves [5].

Fuel	(Oil Equivalents in Billions of Barrels)		Projected Exhaustion Time (years)
	World Annual Production	Proven Reserves	
Coal	17.0	5600	329
Oil	20.3	843	41.5
Natural Gas	11.7	1400	120
Nuclear (Uranium)	2.75	315	115

Therefore, among the various energy options available today, PV is one of the most promising candidate. The Earth's surface receives about 1.2×10^{17} W power while the world energy consumption is ~1.1×10^{17} kWh/yr, indicating that incident sunlight in less

than one hour is enough to satisfy the world energy consumption for the whole year. In addition, PV produces no noise pollution, can be installed at the point of use to eliminate transmission losses, matches the utility load profile for peek shaving, and is modular so it can be scaled up to any size on the as-needed basis.

In spite of the many advantages listed above, PV accounts for less than 0.2% of the US portfolio for electricity generation (Figure 1.2) because cost of electricity from PV is still higher than the current market price of electricity. Ultimate goal of PV is to reach grid parity where the price of electricity from PV is equal to or lower than market price of electricity. PV is already below grid parity in some parts of the world like Germany, Denmark, and Hawaii, and in many parts it is within the striking distance of grid parity (Figure 1.3). Adoption of PV is expected to grow rapidly as PV attains economical competitiveness to reach grid parity in various parts of the world. In 2012, the installed system cost of a state-of-art commercial-scale PV system was about $3/W [6-8] which translates into a levelized cost of electricity (LCOE) in the range of 10–20¢/kWh depending on the solar insolation (Figure 1.3). Therefore, price of electricity from PV is still higher than the market price of electricity (marked as circles) in most countries today but is getting very close to grid parity. Thus, further cost reduction is required to reduce the LCOE by reducing the module and balance of system (BOS) costs because the sum of the two is equal to the installed system cost.

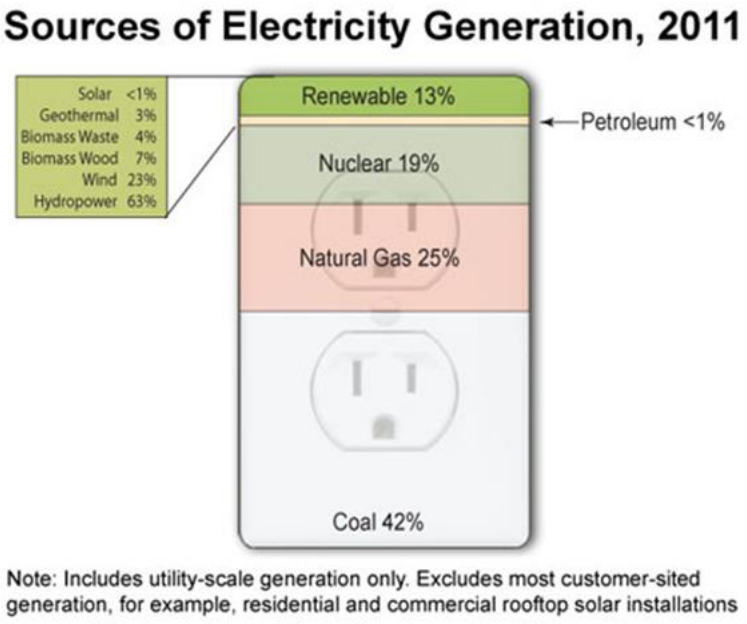

Figure 1.2: Sources of electricity generation at 2011 in US [9].

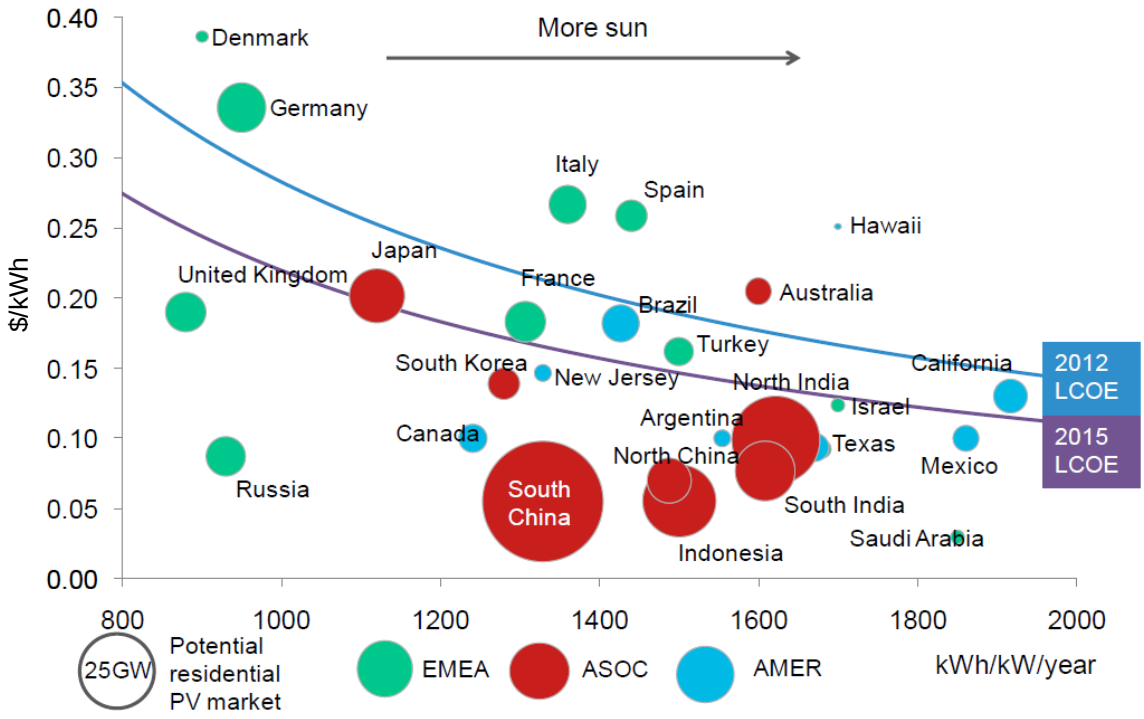

Source: Bloomberg New Energy Finance

Figure 1.3: Residential PV price parity – residential power price versus LCOE.

1.2 Overall objective of the research

The overall objective of this thesis is to reduce the installed system cost via module-cost reduction which accounts for about 35% of the total installed system cost. This will be accomplished by conducting materials and device research that will lead to low-cost high-efficiency solar cells and reduce the module as well as BOS cost. First strategy involves module-cost reduction by using low cost substrate silicon (Si) materials including mono-crystalline Czochralski (Cz) and multi-crystalline (mc) Si because Si substrate accounts for more than 30% of module cost. Second strategy for module-cost reduction involves developing cell designs and technologies that can provide better optical and electrical performance (higher efficiency) without additional processing steps or equipment. Higher efficiency modules also reduce the BOS cost because some BOS components are inversely related to module efficiency and system area. The third strategy involves developing roadmaps to define the right combination of module cost and efficiency to attain grid parity in different parts of the world. This involves extensive modeling to calculate levelized cost of electricity from PV as a function of all the key system and financial parameters.

1.3 Specific research objectives

The goal of this thesis is to develop low-cost high-efficiency crystalline Si (c-Si) solar cells which are at the right intersection of cost and efficiency to make PV affordable. The objective will be addressed by improving the optical and electrical performance of Si solar cells through process optimization, device modeling, clever cell design, fundamental understanding, and minimization of loss mechanisms. This is accomplished

through the following five technical tasks in this thesis. In addition, detailed cost analysis is performed to quantify the impact of key system and financial parameters in the LCOE along with development of analytical models to assess the premium or value associated with efficiency, temperature coefficient, BOS cost, and solar insolation. This is presented in the final chapters of this thesis.

1.3.1 Task 1: Deposition of silane-free SiC_xN_y film and assessment of its antireflection and passivation properties (Chapter 3)

Plasma-enhanced chemical-vapor deposition (PECVD) of silicon-nitride (SiN_x) film is widely used for fabrication of commercial Si solar cells. SiN_x film serves as antireflection (AR) coating and provides excellent surface passivation on phosphorus-doped emitters because of high-positive charge density [10]. The optimum refractive index for an AR coating layer is about 2.4 for solar cells encapsulated under glass [11]. This is achievable by growing Si-rich SiN_x films. However, the deposition of current SiN_x films typically require highly pyrophoric and toxic silane (SiH_4) gas. This requires extensive care in handling, storage, and transport which lead to significant increase in cost. This provided the motivation to investigate a novel silane-free source for depositing SiN_x based AR coating in this research. To eliminate the need for storage and handling of silane, SiXtron Advanced Materials Inc. developed a novel silane-free source and apparatus for SiN_x deposition which contains atomic sources such as silicon, carbon, and hydrogen. This allows deposition of silicon-carbon-nitride films (SiC_xN_y) with different compositions by adjusting the source composition or by changing the accompanying ammonia (NH_3) flow rate during the deposition. Another unique feature of this silane-free source is that it can

be adapted to the existing PECVD production line or reactor without any modification or cost. However, very little is known about the performance of such coatings. In this research, a detailed characterization and analysis of this film was performed along with its impact on the Si solar cell performance. Therefore, in Task 1, the feasibility of using SiC_xN_y films is explored for the first time in this thesis by depositing these films in a conventional PECVD reactor. For comparison, conventional SiN_x films were also grown in the same reactor using silane gas. Detailed optical and electrical properties of SiC_xN_y films are investigated and compared with conventional SiN_x films. Finally, high-efficiency commercial-ready solar cells are fabricated with SiC_xN_y AR coating and compared with the conventional SiN_x-coated solar cells to demonstrate the feasibility of novel SiC_xN_y films for PV application.

1.3.2 Task 2: SiC_xN_y-induced reduction of light-induced degradation in Cz Silicon solar cell efficiency (Chapter 4)

Bulk lifetime and efficiency degradation under illumination in widely used boron-doped Cz solar cells is well known and is attributed to the formation of boron and oxygen complexes ($B\text{-}O_{2i}$) [12, 13]. This could lead to a factor of 2–5 reduction in bulk lifetime and 0.2–0.6% loss in absolute cell efficiency. However, limited data in the literature shows that carbon (C) in Si may retard light-induced degradation (LID). This provided the motivation to investigate if the presence of C in the novel SiC_xN_y coatings can help in reducing the LID in Cz Si solar cells. Therefore, in Task 2, the injection of C from the SiC_xN_y AR coating (developed in Task 1) into the bulk Si is examined during high temperature deposition and contact firing. The idea behind this concept is to see if the

injected C into the bulk can compete with boron to reduce the formation of number of B-O_{2i} defects and the corresponding LID. Reduction in LID as a result of additional C from the AR coating into the bulk Si is investigated quantitatively by complete fabrication and analysis of commercial-ready boron-doped Cz cells coated with the conventional SiN_x coating deposited by silane as well as SiC_xN_y films deposited from an silane-free source. Injection of carbon in Si was examined by analytical techniques. LID in cell performance was examined after 72 hours of one Sun illumination of the cell.

1.3.3 Task 3: SiC_xN_y-induced retardation of fill factor degradation under low level illumination (Chapter 5)

It is well known that if shunt resistance (R_{sh}) of 239 cm^2 Cz solar cells is more than 7 Ω or ~1600 Ω-cm^2, R_{sh} does not hurt the cell performance under Standard Test Conditions (STC – 1000 W/m^2 intensity and 25°C cell temperature). However, a solar cell module under operation is rarely at STC. Instead, most of the day a module remains well below STC illumination, depending on the geographical location and the weather. It has been suggested that solar cell efficiency could decrease at lower than STC illumination [14] depending on the R_{sh} value even if the starting cell efficiency at STC is identical [15, 16]. This phenomenon is attributed to R_{sh}-induced fill factor (FF) degradation at low illumination. Cell efficiency is proportional to FF which is a measure of squareness of the I-V curve. During the preliminary investigation, it was found that SiC_xN_y-coated cell had higher R_{sh} than conventional SiN_x-coated cells. This provided the motivation to evaluate and quantify the cost and performance benefit associated with higher performance of silane-free SiC_xN_y-coated cells under low solar insolation. Therefore, in Task 3,

theoretical calculations are performed using appropriate models and analytical equations to explain the reason for the low illumination induced degradation of FF and then quantitatively assess its impact on cell efficiency and energy production. First, the effect of R_{sh} on FF and efficiency as a function of illumination level is calculated. Secondly, an attempt is made to achieve high R_{sh} values by carbon-containing AR coatings (SiC_xN_y) and tailoring the screen-printed contact firing conditions. Complete large area screen-printed cells are fabricated to demonstrate that SiC_xN_y coatings can indeed give higher FF than the traditional SiN_x films. Finally, the benefit of the high R_{sh} (or improved low illumination performance) on increased annual energy production and reduced LCOE is calculated by using a high level PV system modeling program, System Advisor Model (SAM).

1.3.4 Task 4: Modeling and optimization of index and thickness of SiN_x antireflection coating for the best performance of silicon solar cells placed in modules (Chapter 6)

PECVD SiN_x films are commonly used as an AR coating for Si solar cells because of their excellent optical properties. From the quarter-wavelength or Fresnel equation, one can calculate optimum film index and thickness to minimize the optical loss [17]. However, the quarter-wavelength equation assumes a planar surface and excludes parasitic absorption inside the film which can be quite large in high index SiN_x films. In addition, it is difficult to analyze various surface morphologies and film interface properties quantitatively using the Fresnel equation because surface texturing affects absorption as well as reflection of the film. In addition, cells are generally placed in a

module under a layer of ethylene vinyl acetate (EVA) and glass, which also influences the reflective properties of the cells. This provided the motivation to account for all these effects and come up with the design (thickness and index) of SiN_x based AR coating that can lead to maximum power output from the cells encapsulated in a module. Therefore, in Task 4, a Monte-Carlo geometrical ray tracing program, Sunrays, is used to perform accurate assessment of reflection and absorption losses as a function of surface morphology, bulk, and interface properties of the film. Each ray of light is traced according to the law of geometrical optics which enables one to characterize specific surface morphologies and cell structures with various dimensions. First, bulk properties of the SiN_x films with refractive index (n) in the range of 2.03–2.42 are compiled for modeling. Ray tracing simulations are performed on planar as well as standard pyramid like textured surfaces with various SiN_x AR coatings, and performance (reflection + absorption) of each film is evaluated in air (n = 1) as well as under encapsulated glass module (n = 1.5). Next, all the optical losses (reflection + absorption) from Sunrays modeling are translated into a reflectance file and used in PC1D device simulation program to calculate the expected cell efficiency in air and under glass along with the corresponding efficiency loss when the cell is placed in a glass module. Final calculated cell efficiency inside the module is used as the figure of merit to optimize the design of SiN_x AR coating because module efficiency dictates the energy output and LCOE.

1.3.5 Task 5: Investigation of ALD Al_2O_3 passivation dielectric to enhance cell efficiency (Chapter 7)

Solar cell is an opto-electronic device so both optical and electrical properties are critical. While AR coating and texturing is used for improving light trapping and optical properties of solar cells, dielectric passivation of surfaces is widely used to enhance the electrical properties of solar cells. Dielectric films can reduce surface recombination by reducing the dangling Si bonds or the number of defects on the surface and also by inducing an electric field to repel or attract carriers. Historically, silicon dioxide (SiO_2) or SiN_x films are deposited on the Si surface to accomplish this goal. However, recently, atomic layer deposition (ALD) aluminum oxide (Al_2O_3) has become a popular dielectric for Si surface passivation. Several investigators have reported excellent passivation quality Al_2O_3 [18-21] on the back surface of p-type solar cells. This is attributed to a large negative charge in the Al_2O_3 film which creates an accumulation layer on the p-type back surface to reduce recombination. However, Al_2O_3 is not yet being used in commercial cells because of certain issues related to deposition and annealing conditions, thermal stability, and degradation of passivation quality after firing of screen-printed contacts. This provided the motivation to understand and optimize the passivation quality, efficiency enhancement, and stability of Al_2O_3 films. Therefore, in this task, optimization of Al_2O_3 passivation for screen-printed cells is conducted by tailoring deposition and annealing conditions of Al_2O_3 in conjunction with contact firing. Surface recombination velocity (SRV) is calculated from quasi-steady-state photo-conductance (QSSPC) lifetime measurements, and its impact on cell efficiency and thermal stability is assessed

by fabricating commercial-ready large area (239 cm^2) Al_2O_3 passivated solar cells with screen-printed contacts.

1.3.6 Task 6: Cost modeling and numerical analysis to quantify the efficiency premium and the impact of key system and financial parameters on levelized cost of electricity (Chapter 8, 9)

While the above five tasks attempt to improve Si solar cell performance by enhancing the optical and electrical properties of cells, this task involves development and use of various cost models to assess the economical impact of cell efficiency enhancement on module cost and LCOE. Higher-efficiency modules not only produce more power, but they also reduce the BOS cost because labor and hardware costs decrease as the system area shrinks with module efficiency. It is also important to know how much more one should pay for higher-efficiency modules (efficiency premium) compared to a reference modules without impacting the LCOE. This is even more important when customers are faced with the choice of different PV modules (like thin films and Si) which have different cost, efficiency, and temperature coefficients for efficiency degradation. Task 6 quantifies the efficiency premium for higher-efficiency modules and provides guideline for how to choose the right combination of module cost and efficiency that can lead to a desired LCOE in a given location.

LCOE is the key parameter to assess the performance and cost effectiveness of a PV system. LCOE is a strong function of installed system cost, financial parameters, and solar insolation. In addition, installed system cost is dependent on module and BOS cost which are partly dependent on module efficiency. Extensive PV system modeling is

conducted in this task to quantify the sensitivity and impact of all key system parameters such as installed system cost, BOS cost, module efficiency, operating performance loss, module cost, and system lifetime as well as financial parameters such as loan fraction, interest rate, and depreciation on the LCOE. Novel contour plots and curves are generated that can provide excellent guidelines for creating roadmaps for grid parity and cost reduction in a given location. These plots are also very helpful in defining the right intersection of module cost and efficiency in a given location with different solar insolation, BOS cost, and financing. Finally, model calculations are extended to show what should be the installed system cost in different parts of the world to attain grid parity.

CHAPTER 2

LITERATURE REVIEW

2.1 Basic operation of silicon solar cells

Photovoltaics (PV) is the direct conversion of sunlight into electrical energy using a simple semiconductor device called solar cell. Photons are absorbed in a semiconductor by generating electron-hole pairs, which are separated by the electric field in p-n junction and are subsequently collected by metal contacts on the surface (Figure 2.1). To produce more electricity, generated carriers need to live long enough to avoid recombination and get to the p-n junction. Recombination of carriers can occur at the front surface (1), n-type silicon (Si) emitter (2), p-type Si bulk (3), and back surface (4) [22].

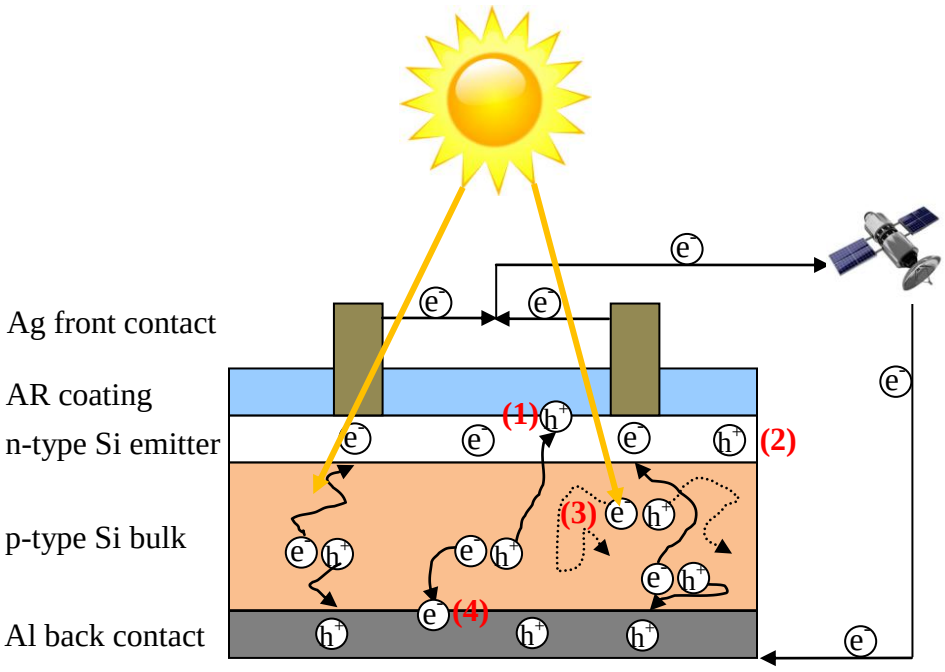

Figure 2.1: Operation of silicon solar cells.

Solar cells convert the incident sunlight into electrical energy. Conversion efficiency is most important parameter to account for the performance of solar cells. Conversion efficiency is defined as ratio of electrical power output (P_{out}) and the incident photon power (P_{in}) [11] and is expressed as

$$E_{ff}(\eta) = \frac{P_{out}}{P_{in}} = \frac{V_{mp} \cdot I_{mp}}{P_{in}} = \frac{V_{oc} \cdot I_{sc} \cdot FF}{P_{in}} \tag{2.1}$$

Where V_{mp} and I_{mp} is the voltage and current at maximum power point (P_{max}), and fill factor (FF) is the measure of squareness of the I-V curve (Figure 2.2) defined as

$$FF = \frac{V_{mp} \cdot I_{mp}}{V_{oc} \cdot I_{sc}} \tag{2.2}$$

Open circuit voltage (V_{oc}) and short circuit current (I_{sc}) are defined as

$$V_{oc} = \frac{kT}{q} \ln\left(\frac{I_{sc}}{I_o}\right) \tag{2.3}$$

$$I_{sc} = \int_{E_g}^{\infty} q \cdot N_{ph}(\lambda) \cdot [1 - R(\lambda)] \cdot IQE(\lambda) d\lambda \tag{2.4}$$

Where k (1.38×10^{-23} J/K) is Boltzmann constant, E_g is the bandgap of semiconductor material, $N_{ph}(\lambda)$ is the number of photon, and $R(\lambda)$ is reflectance. I_o is reverse saturation current [11, 23] of finite dimension p-n junction diode and it takes the form

$$I_o = I_{oe} + I_{ob} = A\left(\frac{qD_h n_i^2}{L_h N_D} \cdot F_N + \frac{qD_e n_i^2}{L_e N_A} \cdot F_P\right) = A\left(\frac{qn_i^2}{N_D} \cdot S_{eje} + \frac{qn_i^2}{N_A} \cdot S_{ejb}\right) \tag{2.5}$$

$$F_N = \frac{S_h \cosh(W_N / L_h) + D_h / L_h \sinh(W_N / L_h)}{D_h / L_h \cosh(W_N / L_h) + S_h \sinh(W_N / L_h)} \tag{2.6}$$

$$F_P = \frac{S_e \cosh(W_P / L_e) + D_e / L_e \sinh(W_P / L_e)}{D_e / L_e \cosh(W_P / L_e) + S_e \sinh(W_P / L_e)} \tag{2.7}$$

Where S_h and S_e are hole and electron surface recombination velocities, respectively. If front and back surfaces experience high recombination of carriers (S_h and $S_e \approx \infty$), F_N and F_P are reduced to

$$F_N = \coth\left(\frac{W_N}{L_h}\right),\ F_P = \coth\left(\frac{W_P}{L_e}\right) \tag{2.8}$$

In contrast, if front and back surfaces experience very low recombination of carriers (S_h and $S_e \approx 0$), F_N and F_P can be expressed as

$$F_N = \tanh\left(\frac{W_N}{L_h}\right),\ F_P = \tanh\left(\frac{W_P}{L_e}\right) \tag{2.9}$$

I_{oe} accounts for the recombination at front surface (*FSRV*) and in the n-type emitter ((1) + (2) in Figure 2.1), and I_{ob} accounts for the recombination in the p-type Si bulk and back surface (*BSRV*) ((3) + (4) in Figure 2.1). Unit of *FSRV* and *BSRV* is cm/s. Thus, reduction of *FSRV* or *BSRV* reduces I_o which in turns increases V_{oc} and conversion efficiency of solar cells.

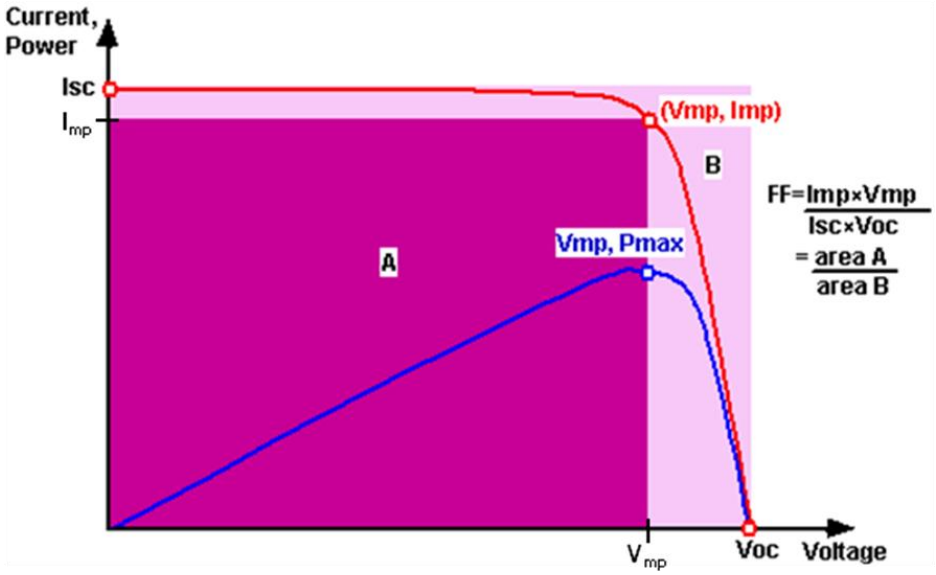

Figure 2.2: Current and voltage (I-V) curve of solar cells.

Basic structure of Si solar cell is a replace of a p-n junction diode. A more sophisticated double-diode model accounts for leakage current in the depletion region (I_{o2}) and shunt and series resistance which are neglected in an ideal single-diode model. Figure 2.3 shows the double-diode equivalent circuit of solar cell when it is illuminated.

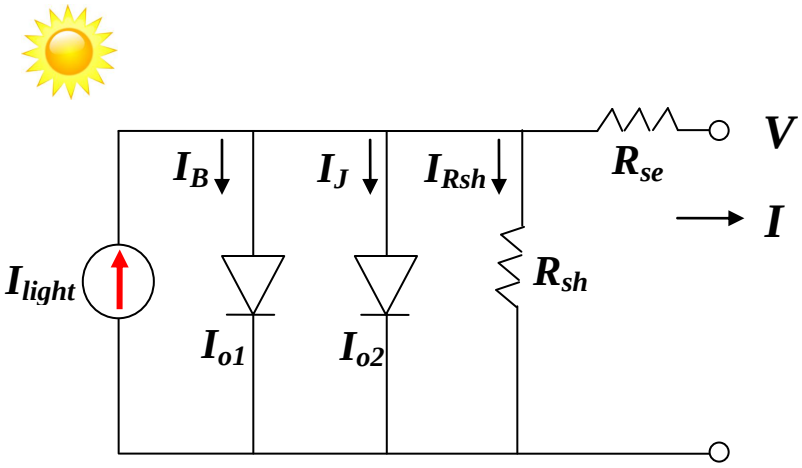

Figure 2.3: Solar cell equivalent circuit.

From the Figure 2.3, current from solar cell when it is illuminated can be expressed as

$$I = I_{light} - I_B - I_J - I_{Rsh} \tag{2.10}$$

$$I = I_{light} - I_{o1}\left\{\exp\left(\frac{q(V+IR_{se})}{kT}\right)-1\right\} - I_{o2}\left\{\exp\left(\frac{q(V+IR_{se})}{nkT}\right)-1\right\} - \frac{V+IR_{se}}{R_{sh}} \tag{2.11}$$

$$I_{light} = \int_{E_g}^{\infty} q \cdot N_{ph}(\lambda) \cdot [1 - R(\lambda)] d\lambda \tag{2.12}$$

2.2 Review of crystalline silicon solar cells

In 2012, more than 30 GW of PV was installed taking the cumulative installed PV to ~100 GW in the world. Crystalline silicon (c-Si) accounts for ~90% of the PV market share, and single crystalline silicon share is about half of that [6] (Figure 2.4). Multi-crystalline (mc) Si is lower in cost, but single crystal Czochralski (Cz) Si offers potential for higher efficiency cells.

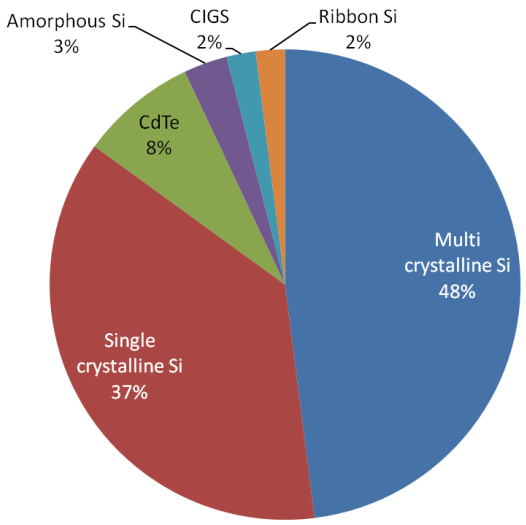

Figure 2.4: PV materials and technologies market share in 2010.

Pseudo square 180–200 μm thick boron doped p-type ~2 Ω-cm Cz wafers with an area of 239 cm^2 (156 × 156 cm) are widely used as industry standard. As-grown ~2 Ω-cm resistivity p-type Cz wafers typically provide bulk lifetime of ~200 μs, which is sufficient for achieving high efficiency on ~200 μm thick wafers. Model calculations in Figure 2.5 show that efficiency loss from bulk lifetime is below 0.3% compared to much higher cost float zone (FZ) wafer, which typically has a bulk life time of around 1 ms.

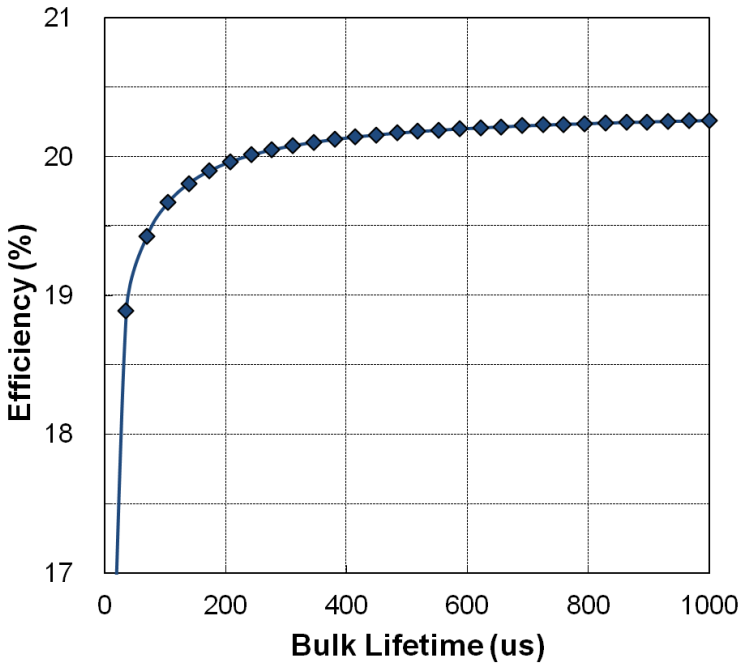

Figure 2.5: Solar cell efficiency as a function of bulk lifetime.

Current technologies in production achieve Cz solar cells efficiency in the range of 16–20% depending on the material quality, cell design, and technology. Mainstream mass production adopts screen-printing technique for front metallization and aluminum-back-surface field (Al-BSF) formation because of simplicity, high-throughput, and low manufacturing cost. Figure 2.6 shows the structure and process sequence of a typical baseline commercial cell. Process sequence involves surface texturing, $POCl_3$ gas diffusion for emitter formation, silicon-nitride (SiN_x) antireflection (AR) coating deposition, screen-printing of front silver (Ag) grid and full back Al, inline belt furnace co-firing to form front and back contacts and p^+ Al-BSF, and laser edge isolation to isolate the front and back sides.

Figure 2.7 shows a roadmap for achieving 20% efficient Cz solar cells. In this roadmap, baseline solar cells start with 18.2% efficiency and a 60 Ω/sq homogeneous emitter with

screen-printed full Al-BSF structure (Figure 2.6). This baseline structure has back surface recombination velocity (BSRV) of ~300 cm/s and back surface reflection (BSR) of ~70% [22]. Formation of selective emitter [24] in conjunction with higher emitter sheet resistance (100 Ω/sq) can result in 19% efficient screen-printing Al-BSF solar cells.

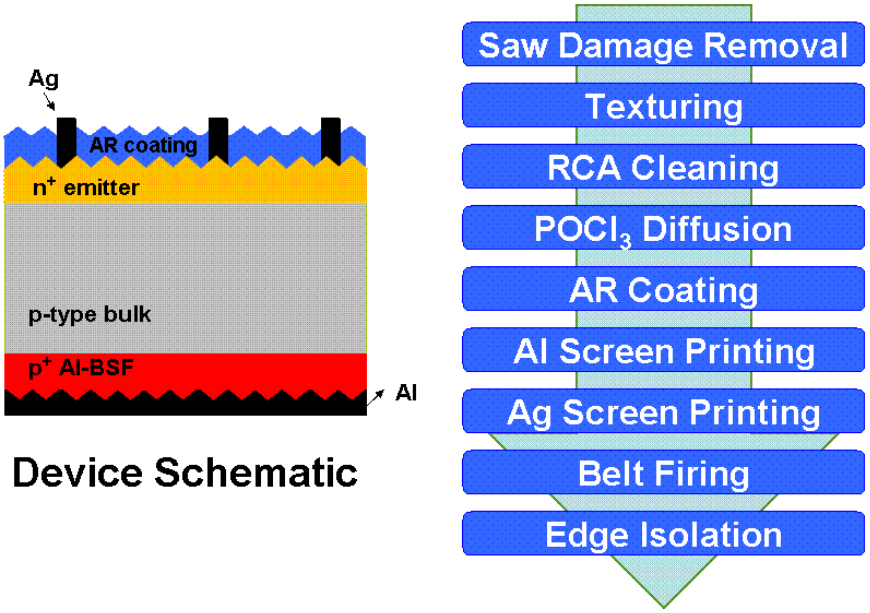

Figure 2.6: Structure and process sequence of a typical commercial cell.

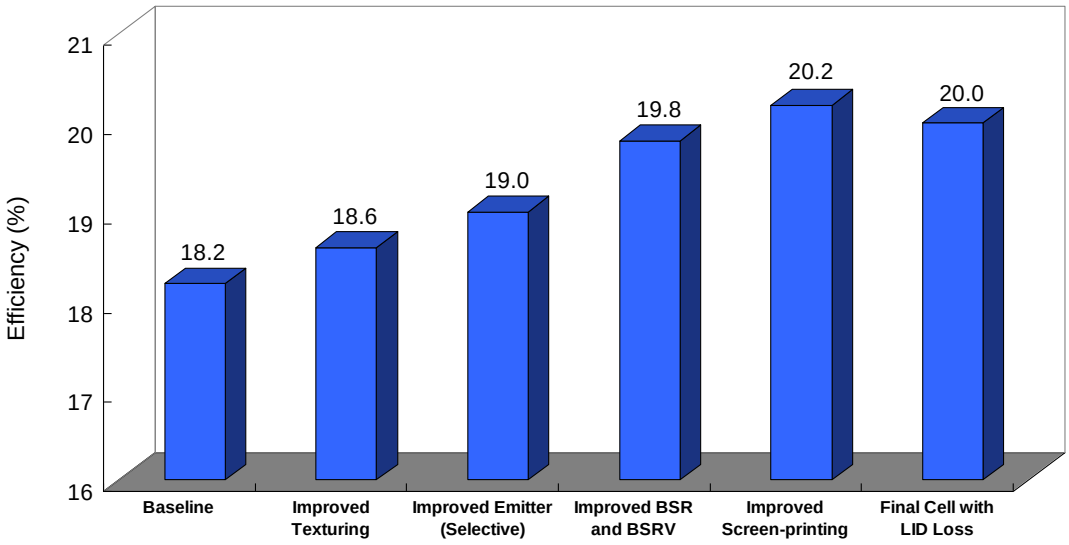

Figure 2.7: Roadmap to 20% efficiency p-type Cz solar cell.

However, to achieve 20% efficient solar cells, screen-printed full Al-BSF structure needs to be replaced by an improved back structure. Model calculation reveal that improved BSR from 70 to 95% and BSRV from 300 to 100 cm/s can provide additional 0.8% absolute efficiency gain [22]. A BSR value of 95% and 100 cm/s BSRV can be achieved simultaneously by a stack of dielectric with point contacts or local BSF, known as passivated emitter rear contact (PERC) cell (Figure 2.8) [25]. Some manufacturers have recently started manufacturing PERC cells with efficiency approaching 20%.

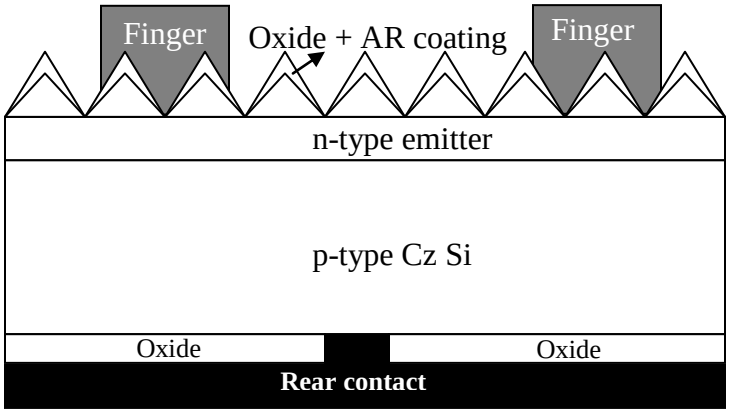

Figure 2.8: PERC cell structure.

More recently n-type cells have become popular with boron emitters, phosphorus front or back-surface fields (Figure 2.9) with efficiencies exceeding 20%. SunPower makes ~24% n-type cells [26] in production with interdigitated back contact cell (IBC). Sanyo Corporation makes amorphous heterojunction with intrinsic thin layer (HIT) cell with efficiency of ~23% [26, 27]. This cell has a-Si/c-Si heterojunction as well as BSF (Figure 2.10).

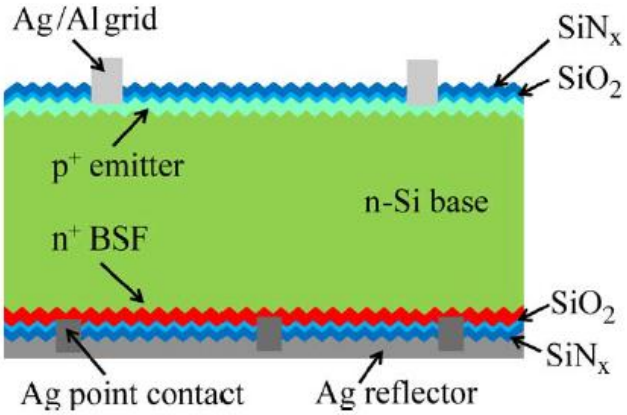

Figure 2.9: Structure of n-type solar cell (p^+-n-n^+) [28].

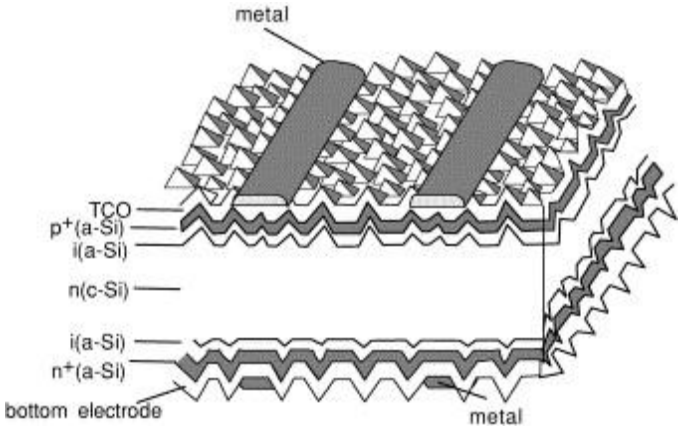

Figure 2.10: HIT solar cell [27].

Finally, Figure 2.11 shows the world highest efficiency (~25%) 4 cm^2 Si cells produced in laboratory [29]. This structure is called passivated emitter with rear locally diffused (PERL) cell. This has inverted pyramid texturing, selective emitter, front and back oxide passivation, excellent back surface reflector formed by dielectric capped with evaporated metal, FZ Si, and photolithography contacts. This structure requires eight high temperature steps and five photolithography masks and is, therefore, very expensive to manufacture. In this research, large area screen-printed baseline cells with full Al-BSF

will be fabricated on both single- and multi-crystalline silicon. In selected cases, when studying the Al_2O_3 passivation, screen-printed p-type PERC cells as well as front junction n-type cells will also be fabricated.

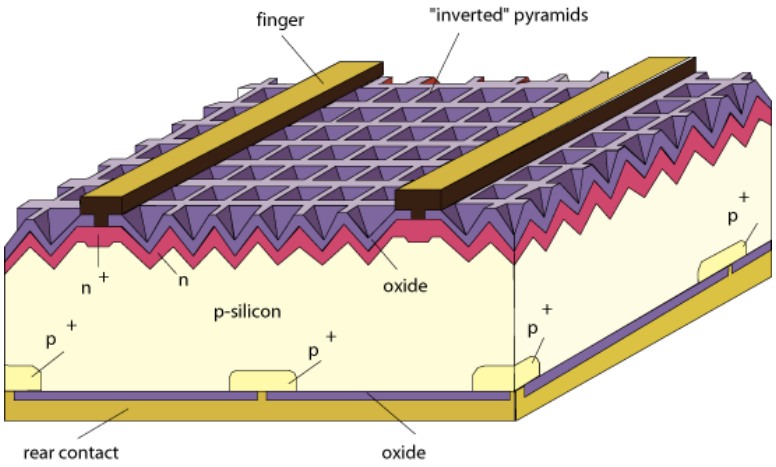

Figure 2.11: High cost 25% efficient PERL cell.

2.3 Antireflection coating

Antireflection (AR) coating is an integral part of a solar cell and will be investigated in this research for enhanced cell and module performance. Incident sunlight is reflected at a surface of solar cell where there is a discontinuity of refractive index. Silicon reflects 35% of the incident sunlight without AR coating [11] (Figure 2.12). Therefore, perfect AR coating, which makes $R(\lambda)$ zero, will increase short circuit current (I_{sc}) from $0.65I_{sc}$ to $1.0I_{sc}$. I_{sc} is expressed by following equation

$$I_{sc} = \int_{E_g}^{\infty} q \cdot N_{ph}(\lambda) \cdot \left[1 - R(\lambda)\right] \cdot IQE(\lambda) d\lambda \qquad (2.13)$$

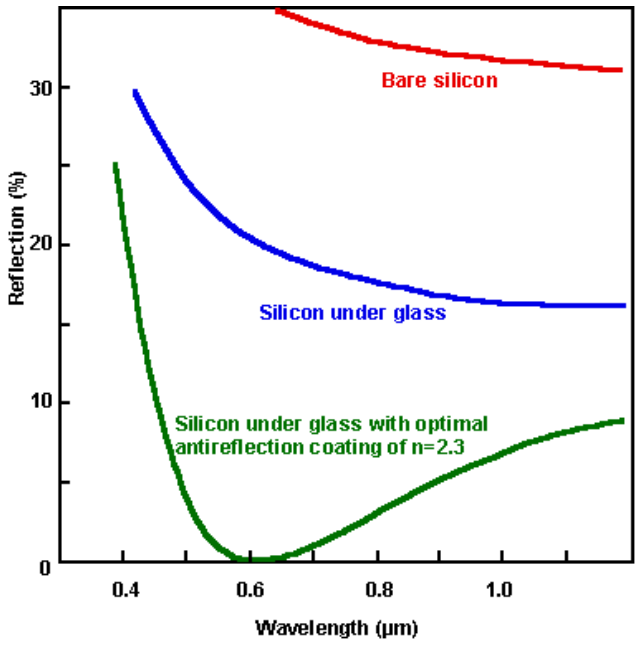

Figure 2.12: Reflectance of bare silicon and silicon with optimized AR coating.

The reflectance (R) is the fraction of the energy in a normally incident beam of light that is reflected from the surface covered by a transparent layer of thickness d_1 (Figure 2.13). R can be expressed by Fresnel's equation [11, 17].

$$R = \frac{r_1^2 + r_2^2 + 2r_1 r_2 \cos\theta}{1 + r_1^2 r_2^2 + 2r_1 r_2 \cos\theta},\ \theta = \frac{2\pi n_1 d_1}{\lambda},\ r_1 = \frac{n_0 - n_1}{n_0 + n_1},\quad r_2 = \frac{n_1 - n_2}{n_1 + n_2} \tag{2.14}$$

where n is the refractive index of a layer.

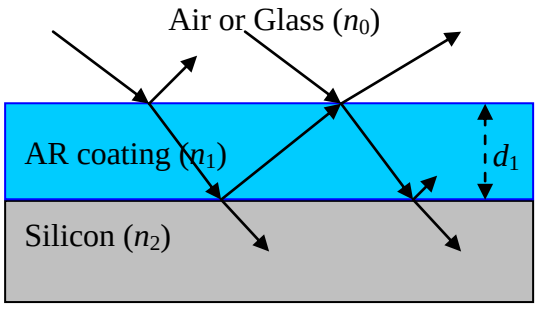

Figure 2.13: Interference effects created by a quarter-wavelength AR coating.

The reflectance has its minimum R_{min} when $n_1 d_1 = \lambda/4$ [17] (quarter-wavelength AR coating) and takes form of

$$R_{min} = \frac{(n_0 n_2 - n_1^2)^2}{(n_0 n_2 + n_1^2)^2} \tag{2.15}$$

With a quarter-wavelength AR coating, light reflected from the second interface arrives back at the first interface 180° out of phase with the light reflected from the first interface, resulting in a destructive interference (Figure 2.14). If $n_1^2 = n_0 n_2$ or $n_1 = \sqrt{n_0 n_2}$, $R_{min} = 0$ at the desired wavelength in destructive interference, $\lambda = 4 n_1 d_1$ which can be selected by tailoring the AR coating thickness.

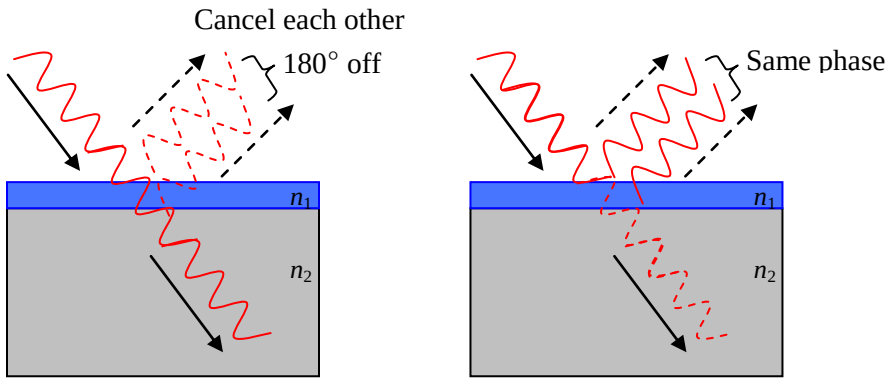

Figure 2.14: Schematic of destructive (left) and constructive interference (right).

Since, solar spectrum has maximum photon energy at a wavelength (λ) of 630 nm (Figure 2.15) [30], AR coating is generally designed to minimize the reflection at 630 nm. Using the above methodology and n_2 = 3.8 for Si, optimized AR coatings for Si solar cells gives n_1 = 1.95 and d_1 = 808 Å for air ambient (n_0 = 1) and n_1 = 2.39 and d_1 = 659 Å for glass ambient (n_0 = 1.5) (Table 2.1).

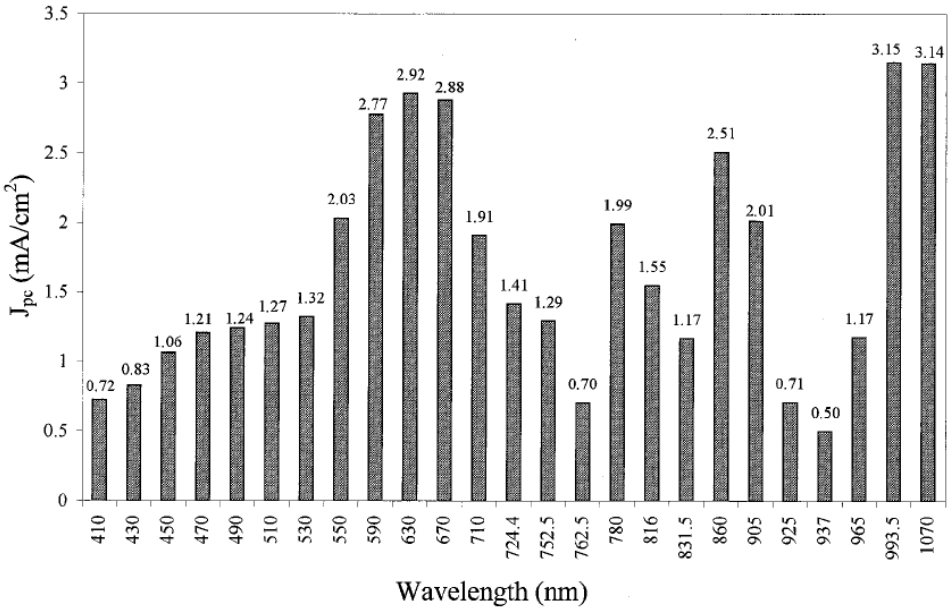

Figure 2.15: Photocurrent density of air mass (AM) 1.5G solar spectrum.

Table 2.1: Optimized AR coatings for Si solar cells.

Bulk (n_2)	Ambient (n_0)	AR coating (n_1)	d_1
Silicon (3.8)	Air (1)	(1.95)	808 Å
Silicon (3.8)	Glass (1.5)	(2.39)	659 Å

AR coating materials such as TiO_2, Ta_2O_5, ZnS, and ZnO offer similar refractive index [31, 32]. Among them, plasma-enhanced chemical-vapor deposition (PECVD) SiN_x film is most popular because of its low cost, capability of hydrogen passivation of the grain boundaries and defects in multi-crystalline solar cells [33], and stability under high temperature. In addition, refractive index of SiN_x film can be adjusted in the range of 1.9–2.4 by modifying deposition conditions [34].

However, SiN_x film with index of $n_1 = 2.39$ under glass does not work well as shown in Figure 2.12 because of high parasitic absorption in the high index SiN_x films which is neglected in the quarter-wavelength AR coating calculations and Figure 2.12–2.14.

Amount of parasitic absorption is determined from the extinction coefficient (k) of a dielectric film. High index SiN_x films have high extinction coefficient [35, 36] (Figure 2.16).

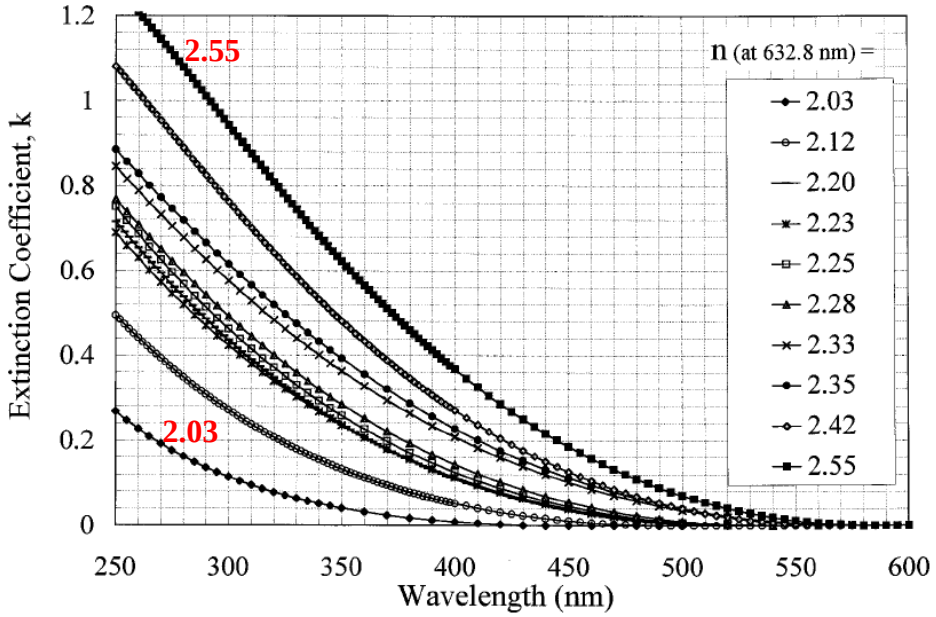

Figure 2.16: Extinction coefficient of SiN_x films.

Intensity of transmitted light is diminished when it passes through the dielectric film according to [11]

$$I(x) = I_o e^{-\alpha x} \tag{2.16}$$

Therefore, amount of parasitic absorption inside the dielectric film with a thickness of x can be expressed as

$$A(x) = I_o(1 - e^{-\alpha x}) \tag{2.17}$$

α is absorption coefficient, which determines the amount of parasitic absorption inside the dielectric film and expressed as

$$\alpha = \frac{4\pi f k}{c} \tag{2.18}$$

Where f is frequency of transmitted light and c is velocity of light. Therefore, dielectric films with higher value of k, such as high index SiN_x film, will absorb more light than the dielectric with lower k.

Doshi et al. [30] investigated SiN_x films in air and under glass for the planar Si surface accounting for parasitic absorption and concluded that n_1 = 2.23 is best under glass because it provides the right compromise between reflection and parasitic absorption (Figure 2.17).

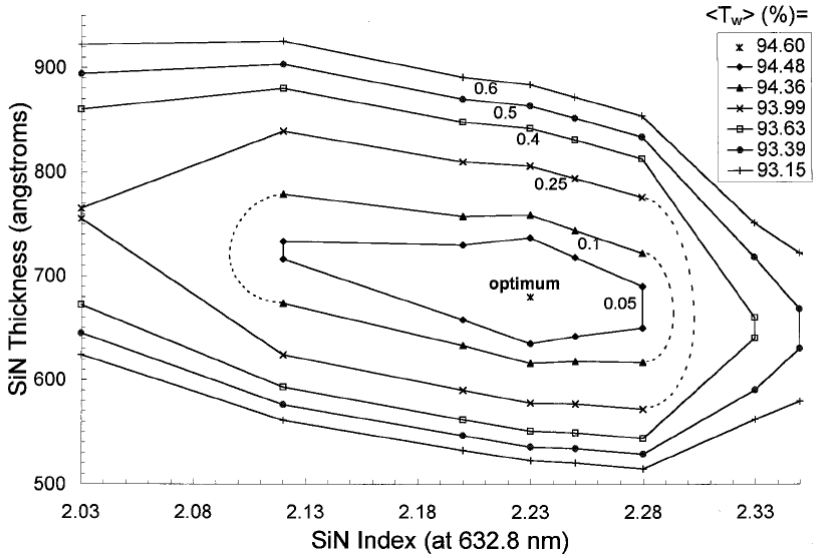

Figure 2.17: Optimization of SiN_x AR coating under glass. Labels in the curve represent the amount of additional photocurrent loss from the optimum.

Later, Grunow et al. [37] accounted for surface texturing by double bounce reflection because commercial c-Si solar cells have pyramid textured surface for optical confinement. Grunow et al. indicated that n_1 = 2.04 is best for both air and glass (Figure

2.18) because of reduced parasitic absorption. This is because reflection is too low for a textured surface to compete with the impact of parasitic absorption.

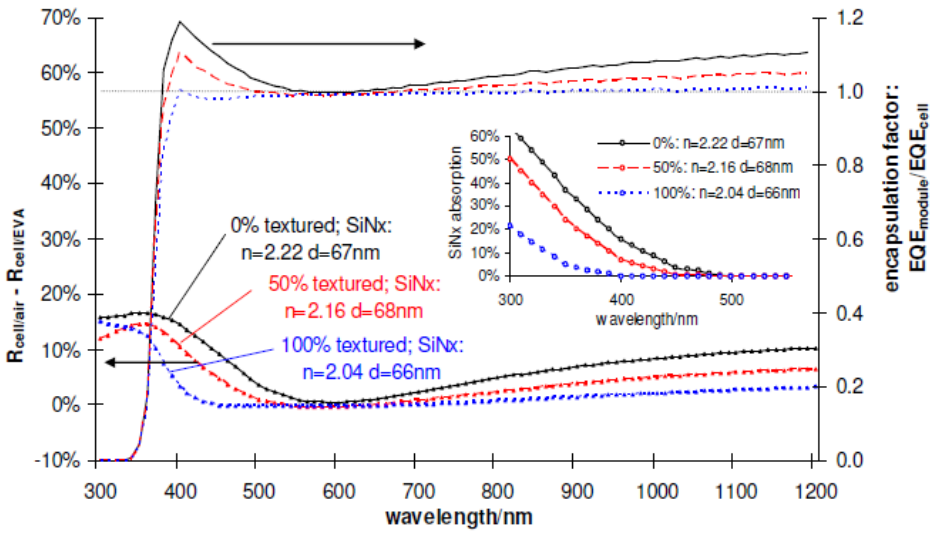

Figure 2.18: Degree of texturing and its impact on the optical losses.

Since module output power is most important for LCOE, detailed calculations are performed in this thesis using a combination of ray tracing and solar cell device modeling program to establish the best composition of SiN_x AR coating under glass that will produce lowest LCOE.

2.4 Surface passivation mechanisms

In a solar cell, photo generated electron-hole pairs can recombine at surfaces to reduce collection efficiency, current, and cell efficiency. As-cut wafers present large number of dangling bonds at the surface which give rise to deep levels or defect states within the forbidden gap [23, 38] (Figure 2.19). Thus, recombination can occur very efficiently at the surface if they are not passivated. Therefore, surface passivation is used extensively

in PV industry to reduce the recombination at the surfaces and in a topic of research in this thesis to enhance cell performance.

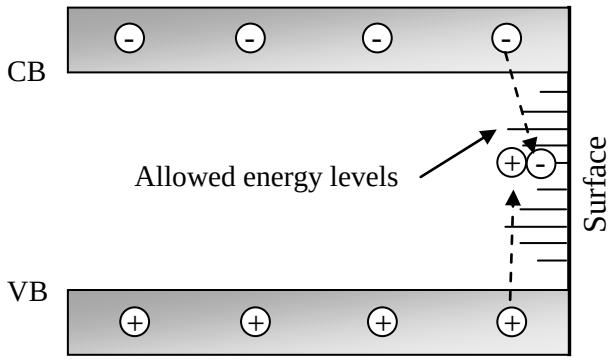

Figure 2.19: Schematic of surface recombination.

Passivation schemes can be divided in two groups. First scheme is chemical passivation, which involves deactivating the dangling bonds on the surface by use of a dielectric film. The second scheme involves field induced passivation, which uses a heavily doped region or charged dielectric to create an electric field to oppose the flow of minority carriers to the surface. In some instances, both schemes can be combined. These two schemes are described in more detail below.

2.4.1 Chemical passivation

Net recombination rate per unit area, *U*, for a single-level surface state is given by the following equation [23]

$$U = \frac{S_e S_h (np - n_i^{\,2})}{S_e (n + n_1) + S_h (p + p_1)} \tag{2.19}$$

Where n and p are electron and hole concentration at the surface, respectively, and n_1 and p_1 is described as

$$n_1 = N_c \exp\left(\frac{E_t - E_c}{kT}\right),\ p_1 = N_v \exp\left(\frac{E_v - E_t}{kT}\right),\ n_1 p_1 = n_i^2 \tag{2.20}$$

S_e and S_h are electron and hole surface recombination velocity (SRV), respectively and expressed as

$$S_e = \sigma_n V_{th} N_t,\ S_h = \sigma_p V_{th} N_t \tag{2.21}$$

Where N_t is number of trap density, and V_{th} is carrier thermal velocity which is equal to

$$V_{th} = \sqrt{\frac{3kT}{m^*}} \tag{2.22}$$

Value of V_{th} is about 1.2×10^7 cm/s at 300 K. σ_n and σ_p are electron and hole capture cross section, respectively, which determines how effectively each charge recombine. Since surface state is distributed rather than a single-level, net recombination rate per unit area, U, for distributed state can be expressed as [22]

$$U = \int_{E_v}^{E_c} \frac{\sigma_n(E) \cdot \sigma_p(E) \cdot V_{th} \cdot N_t(E) \cdot (np - n_i^2)}{\sigma_n(E) \cdot (n + n_1) + \sigma_p(E) \cdot (p + p_1)} dE \tag{2.23}$$

Chemical passivation reduces the S_e and S_h values by reducing the number of defect states (N_t) (Figure 2.20), which has less N_t compared to Figure 2.19. Dielectric films such as thermally grown silicon dioxide (SiO_2), SiN_x, and aluminum oxide (Al_2O_3) are commonly used for this purpose. Right combination of these dielectrics can provide excellent surface passivation with S_{eo} and S_{ho} < 50 cm/s [39], which are sufficient to attain 20% efficient solar cell.

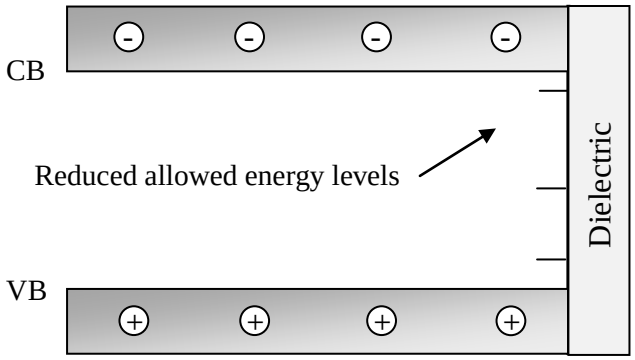

Figure 2.20: Schematic of a chemical passivated surface.

2.4.2 Field-induced passivation

Field-induced passivation is accomplished by attracting or repelling carriers by electric field. Electric field can be generated by a charged dielectric film, tailored doping profile, or a band gap discontinuity. Charge accumulation or inversion at the surface lowers recombination because recombination rate is maximum when $n = p$. Accumulation is generally preferred because inversion layer can be shunted by the contact giving rise to parasitic shunt [22]. Negatively charged dielectric on p-type surface or positively charged dielectric on n-type surface are desirable because they create accumulation below the silicon surface (Figure 2.21). A well known negatively charged dielectric is Al_2O_3 while positively charged dielectrics are SiN_x, silicon-carbide (SiC_x), and silicon-carbon-nitride (SiC_xN_y) [40].

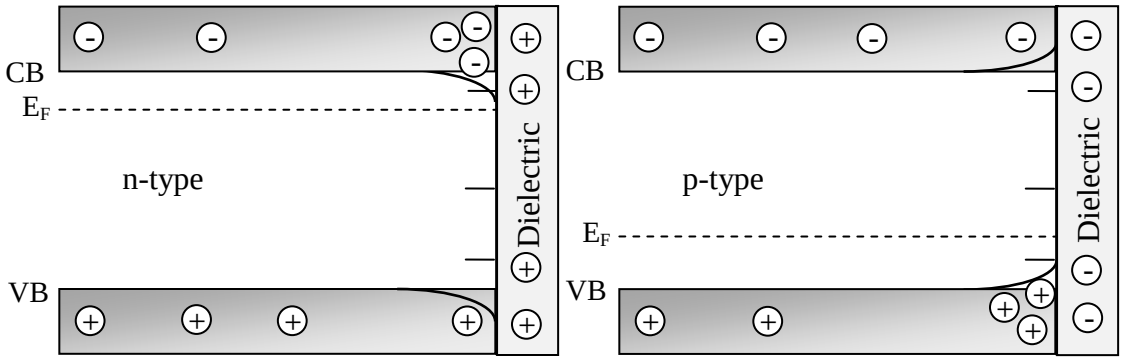

Figure 2.21: Schematic band diagrams for a positive charged dielectric on n-type Si and a negative charged dielectric on p-type Si.

For silicon surface passivation, stack of SiO_2/SiN_x is commonly used on the back surface of a PERC cell in industry which provides good SRV of ~100 cm/s after contact firing and a high cell efficiency of ~19.5%. In this stack, chemical passivation is used because there is not enough charge inside the SiO_2 to generate electric field. Enhanced passivation schemes involve both electrical and chemical passivation simultaneously. This is achieved by using high positively or negatively charged dielectrics [19]. For example, ALD Al_2O_3 has high negative charge (~1×10^{13} cm^{-3}) and provides the lowest SRV on boron (B)-doped Si surfaces (Figure 2.22) [40] compared to SiO_2, SiN_x, and a-Si because they have less charge than Al_2O_3.

Hoex et al. [18, 19] reported excellent passivation quality with SRV of below 10 cm/s using ALD Al_2O_3 on p-type Si surface. Schmidt et al. [21] reported solar cell efficiency close to 21% for PERC cell with ALD Al_2O_3 passivation. However, poor thermal stability of Al_2O_3 has prevented the widespread usage of ALD Al_2O_3 in industry. This is because industrial process frequently requires high temperature (~800°C) firing for screen-printed

metallization after the dielectric deposition which often degrades the Al_2O_3 passivation quality. This provided the motivation to study the Al_2O_3 passivated cells in this research.

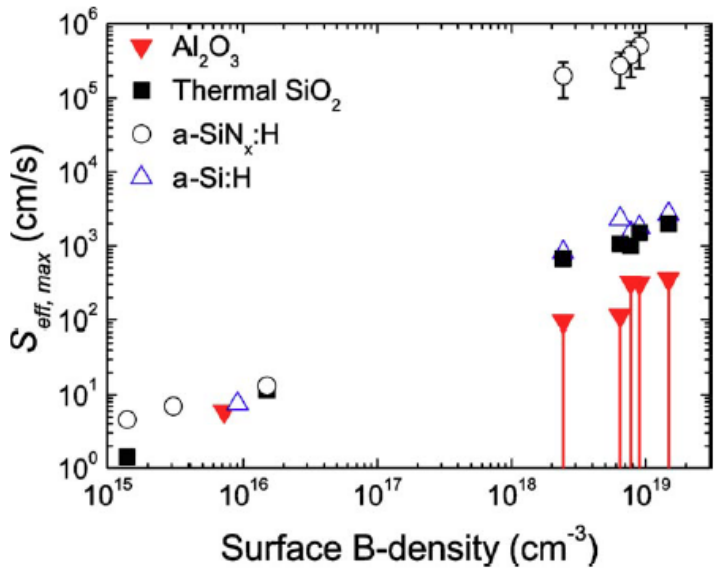

Figure 2.22: Effective SRV of passivated c-Si wafers as a function of boron concentration.

2.5 Light-induced degradation in boron-doped Cz solar cells

Single crystalline Si cells commands ~37% of the market share where B-doped Cz wafers are used. Cz ingots are grown from molten Si in quartz crucible which can inject 15–20 ppm oxygen into the ingot. Solar cells manufactured on B-doped Cz wafers show degradation in bulk lifetime and corresponding efficiency after several hours of illumination (Figure 2.23) prior to reaching a stable performance level [12, 13, 41]. This phenomenon is attributed to the formation of B-O complex. This led to the investigation of a novel SiC_xN_y AR coating in this thesis which has the potential of reducing B-O complex formation and light-induced degradation (LID).

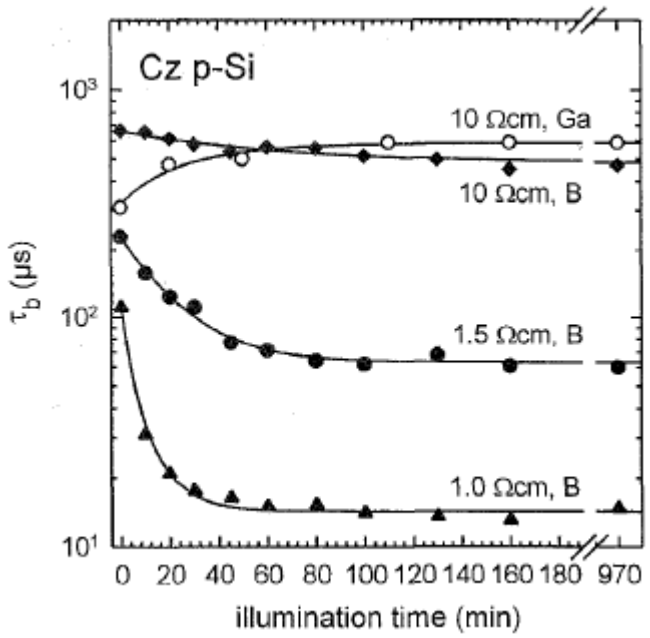

Figure 2.23: Bulk lifetime (τ_b) change of three boron doped and one gallium doped Cz wafers under several hours illumination.

LID phenomenon is reversible because degraded bulk lifetime can be restored (Figure 2.24) by annealing the sample in the dark for 10 min at temperature above 150℃.

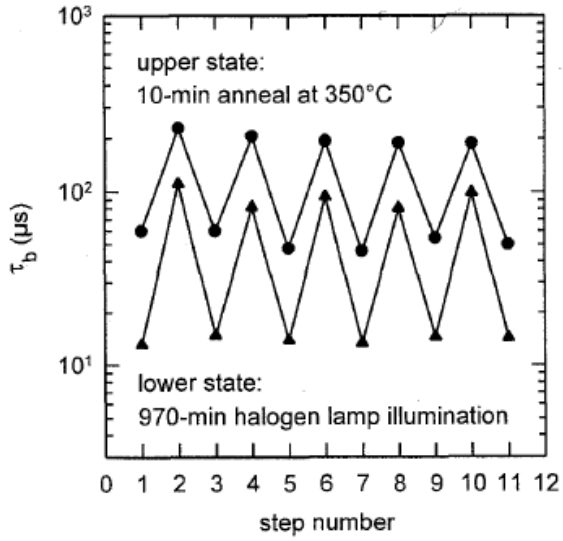

Figure 2.24: Bulk lifetime of B-doped 1 and 1.5 Ω-cm Cz wafers.

In addition, bulk lifetime degradation under illumination strongly depends on the oxygen and boron concentration as described in Figure 2.25 [42].

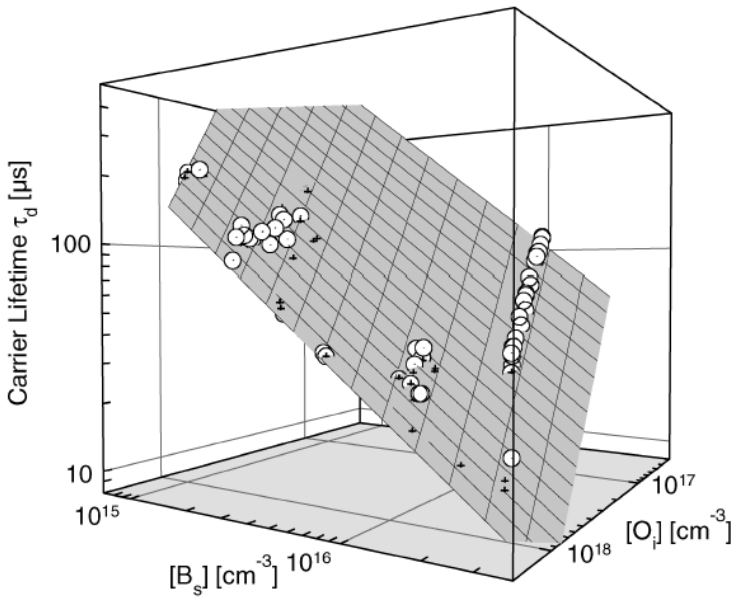

Figure 2.25: Carrier lifetime of Cz wafer as a function of substitutional boron and interstitial oxygen concentration.

LID phenomenon is known for more than 30 years and is attributed to the activation of a specific metastable defect, which is associated with a boron and oxygen complex [43] in Si. According to the current model and understanding, the fast-diffusing oxygen dimmers (O_{2i}) diffuse under illumination and are captured by substitutional boron to form B_s-O_{2i} complex (Figure 2.26), which acts as an effective recombination center and reduces the bulk lifetime of Cz wafers. Bulk lifetime of Cz wafers after LID is a strong function of B_s and O_i concentration and can be described as [42]

$$\tau_B(\mu s) = 7.675 \times 10^{45} \times [B_s]^{-0.824} \times [O_i]^{-1.748} \quad (2.24)$$

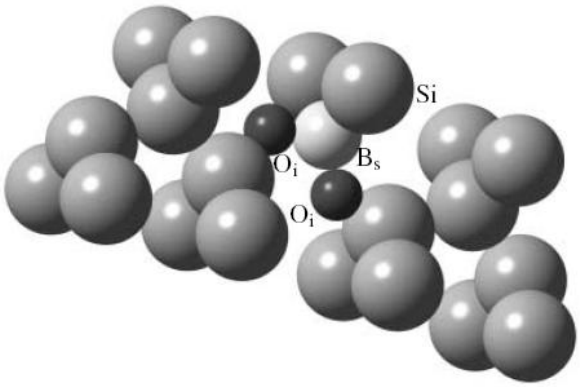

Figure 2.26: Possible configuration of the metastable B_s-O_{2i} complex in the B-doped Cz wafer.

Figure 2.27 shows the calculated bulk lifetime after LID using the above equation. After LID bulk lifetime in a 2 Ω-cm Cz wafers with bulk lifetime of ≥ 200 μs and oxygen concentrations of 7×10^{17}–1×10^{18} cm^{-3}, which is industry standard, is reduced to 42–23 μs. This leads to an appreciable efficiency degradation.

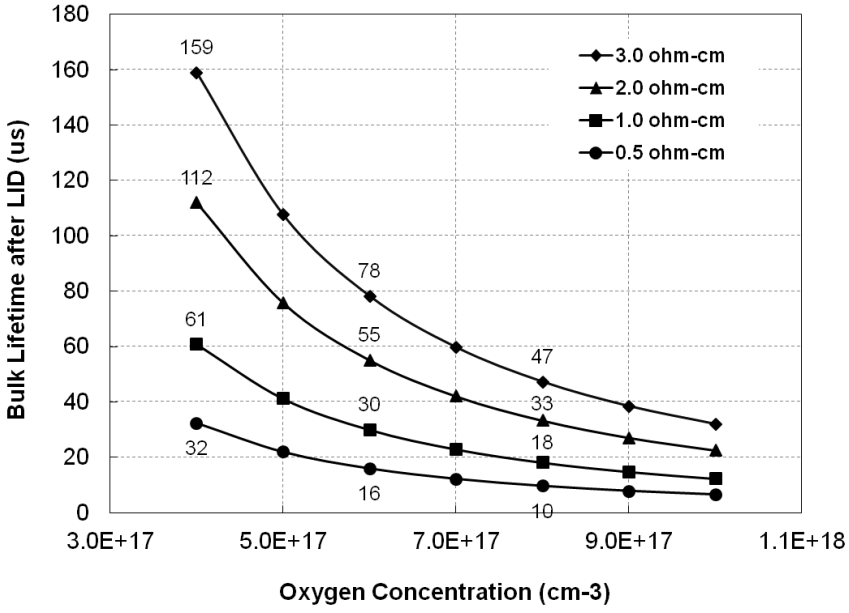

Figure 2.27: Bulk lifetime of B-doped Cz wafers after LID.

Based on this model, several methods for reducing LID in Cz solar cells have been proposed including (1) replacement of B with another p-type dopant element, such as gallium (Ga), (2) reduction of the oxygen concentration in the Cz material, (3) reduction of the B doping concentration, and (4) use of n-type Si wafer. However, the Ga doped Si solar cells generally show a large variation in J_{sc} and efficiency due to the resistivity variation from top to bottom of the ingot due to smaller segregation coefficient of Ga. This will require special care in binning the cells for modules. Attempt to reduce oxygen concentration by magnetically grown Cz requires a higher amount of energy consumption and becomes expensive. In addition, attempt to use higher base resistivity often lowers open V_{oc} and FF resulting in lower cell efficiency, therefore, most p-base cells in industry are made on 2 Ω-cm Si.

There have been some reports of reduced LID in carbon-rich Si materials. For example, Schmidt and Bothe reported a 30% reduction in the B-O_{2i} defects concentration in carbon-contaminated (C = (1.9–3.3) × 10^{17} cm^{-3}) Si material relative to conventional B-doped Si, which contains ~5 × 10^{16} cm^{-3} carbon [12, 13]. In 2006, Coletti et al. also found a reduced concentration of the B-O_{2i} defects in Si wafers in the presence of carbon [44]. They used multi-crystalline Si wafers with same interstitial oxygen (O_i) concentration (1.5–5.6) × 10^{17} cm^{-3} but different carbon concentrations (2–10 ppma). The wafers with a high carbon concentration (8–10 ppma) showed fewer B-O_{2i} defects and higher bulk lifetime after LID compared to the wafers with low (2–4 ppma) carbon concentration (Figure 2.28). This provided the motivation in this thesis to reduce LID by injecting carbon into Si by using a novel SiC_xN_y AR coating instead of the conventional SiN_x coating.

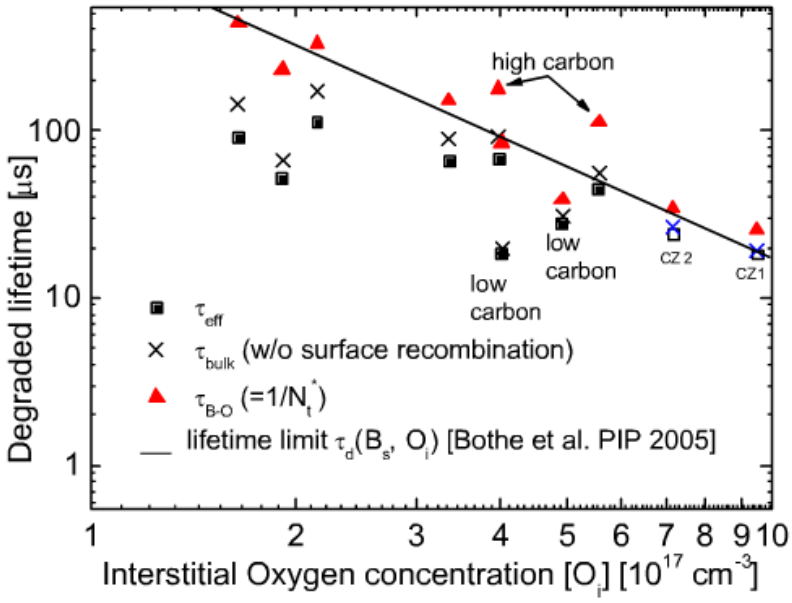

Figure 2.28: Degraded lifetime as a function of interstitial oxygen concentration.

2.6 Cell performance degradation under low level illumination

There have been recent reports [14-16] that solar cell efficiency can decrease under lower than one Sun illumination. In this thesis, attempt has been made to understand and quantify this phenomenon and provide guideline and solution to this problem. Solar cells are generally tested under one Sun illumination (1000 W/m^2), but their efficiency is often found to degrade under lower than Standard Test Condition (STC) illumination mainly because of the V_{oc} and FF degradation. Efficiency degradation happens because I_{sc} decreases linearly with photon flux (N_{ph})

$$I_{sc} \propto q \cdot N_{ph} \cdot IQE \tag{2.25}$$

, and V_{oc} decreases logarithmically with I_{sc}

$$V_{oc} = \frac{kT}{q} \ln\left(\frac{I_{sc}}{I_o} + 1\right) \tag{2.26}$$

Idealized FF_o decreases according to the following equation

$$FF_o = \frac{\upsilon_{oc} - \ln(\upsilon_{oc} + 0.72)}{\upsilon_{oc} + 1},\ \upsilon_{oc} = \frac{V_{oc}}{kT/q} \tag{2.27}$$

Therefore, the R_{CH} (V_{oc}/I_{sc}) value increases, and the normalized r_s and r_{SH} values decrease according to the following equations

$$R_{CH} = \frac{V_{oc}}{I_{sc}},\ r_s = \frac{R_{se}}{R_{CH}},\ r_{SH} = \frac{R_{sh}}{R_{CH}} \tag{2.28}$$

These changes can lower the final *FF* (2.30) [11] especially for devices with R_{sh} below 30 Ω because

$$FF_s = FF_o(1 - r_s) \tag{2.29}$$

$$FF = FF_s\left[1 - \frac{(\upsilon_{oc} + 0.7)FF_s}{\upsilon_{oc} \cdot r_{SH}}\right] \tag{2.30}$$

Theoretical calculations using above equations revealed that *FF* drops more rapidly at lower illuminations for cells with smaller values of R_{sh}. These calculations also show that R_{sh} should be > 8 Ω to reduce the initial sensitivity of efficiency (STC), and R_{sh} should be > 30 Ω to prevent any significant drop at lower illumination. Above 30 Ω degradation is not appreciable, even though higher value is always desirable.

2.7 Levelized cost of electricity from PV

2.7.1 Fundamentals and calculation of levelized cost of electricity

Levelized cost of electricity (LCOE) is the key figure of merit to compare different energy technologies including PV. However, it is a function of large number of variables including system, financial, and location parameters. In this section, attempt has been made to provide a comprehensive understanding of LCOE by reviewing its dependence

on many key parameters. LCOE is defined as cost per unit energy produced over the entire life of system [45-47] and is defined as

$$LCOE(cents/kWh) = \frac{Lifetime\ \ money\ \ spent}{Lifetime\ \ energy\ \ produced} \tag{2.31}$$

Therefore, LCOE is the most important parameter to assess the cost effectiveness of a PV system. Correct LCOE requires accurate assessment of money spent and energy produced (power) during the system lifetime. Money spent over system lifetime (n) consists of payment on the system installation (module, inverter, mounting, racking, labor, site preparation, engineering, and permitting, etc) and annual operation & maintenance ($O\&M$) costs.

$$Lifetime\ \ money\ \ spent = \sum_{0}^{n-1}(Payment + O\&M) \tag{2.32}$$

Lifetime energy produced is determined from the capacity factor. Capacity factor is the ratio of the actual output and the nameplate capacity output of a power plant over a specific period of time.

$$Lifetime\ \ energy\ \ produced = \sum_{0}^{n-1}(Capacity\ \ factor \times 24 \times 365) \tag{2.33}$$

For a PV system, capacity factor can be defined as [48]

$$Capacity\ \ factor = \frac{I_d}{24} \times (1 - derate) \times \frac{100 + \gamma \cdot (T - 25)}{100} \tag{2.31}$$

Where I_d is daily average solar insolation (kWh/m^2/day), and γ is temperature coefficient of module efficiency degradation which accounts for energy output loss when modules operate higher than the room temperature. System derate accounts for all other losses including inverter, transformer, mis-match, soiling, dust, and shading losses. Since

accurate assessment of LCOE involves consideration of time value of money and power which is affected by inflation and real or nominal discount rates [45-47], net present value, which recalls future value into present value with nominal or real discount rate, is used in the LCOE calculations. When nominal discount rate (*ND*) is used to calculate money and real discount rate (*RD*) for power, it is called as real LCOE [45, 49] and is given by

$$\mathrm{Re}al \quad LCOE = \frac{\sum_{0}^{n-1}\left[\left(Annual \quad payment + O\&M\right)\times\left(\frac{1}{1+ND}\right)^{n}\right]}{\sum_{0}^{n-1}\left[Capacity \quad factor\times 24\times 365\times\left(\frac{1-d}{1+RD}\right)^{n}\right]} \tag{2.31}$$

Where (*1 - d*) in the denominator dictates annual system power output degradation. When nominal discount rate is used for both money and power, it is called as nominal LCOE [45, 49] given by

$$No\min al \quad LCOE = \frac{\sum_{0}^{n-1}\left[\left(Annual \quad payment + O\&M\right)\times\left(\frac{1}{1+ND}\right)^{n}\right]}{\sum_{0}^{n-1}\left[Capacity \quad factor\times 24\times 365\times\left(\frac{1-d}{1+ND}\right)^{n}\right]} \tag{2.31}$$

Real discount rate accounts for inflation and relationship between *ND* and *RD* is given by $RD = \frac{(1+ND)}{(1+Inflation)} - 1$.

2.7.2 LCOE studies from Literature

LCOE is highly dependent on the accuracy of multiple inputs which makes it challenging to attain the accurate value. Darling et al. [49] approached from a probability distribution of input parameters feeding into a Monte-Carlo simulation and then provided

LCOE (Figure 2.29) distribution for Boston (9.3¢/kWh), Chicago (9.7¢/kWh), and Sacramento (6.9¢/kWh). In addition, they provided sensitivity of input parameters on the LCOE and concluded that real discount rate and module conversion efficiency are most significant parameters for LCOE.

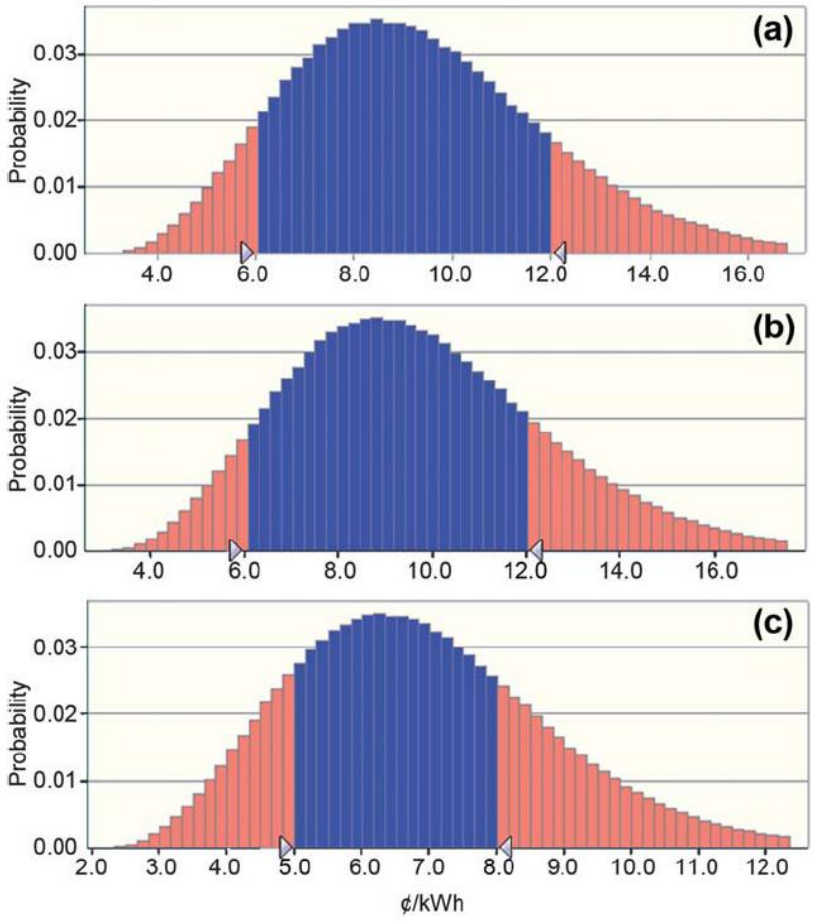

Figure 2.29: LCOE distribution for (a) Boston, (b) Chicago, and (C) Sacramento.

Branker et al. [50] performed sensitivity analysis (Figure 2.30) of key input parameters to represent actual variable input distributions and reduce uncertainty of input parameters.

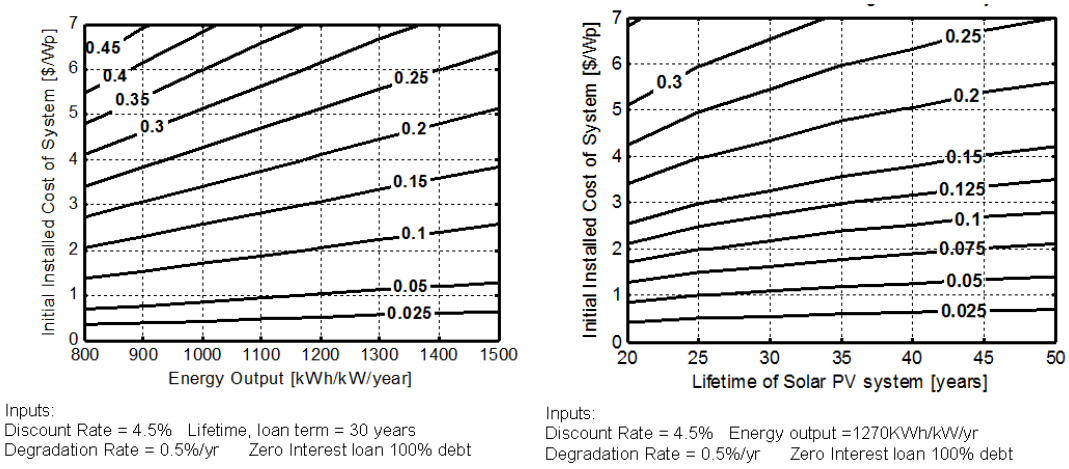

Figure 2.30: LCOE contour plot as a function of key input parameters.

Powell et al. provided a roadmap for lowering the cost of various components of a module to attain grid parity [51] and advanced concept which concluded that c-Si module cost should be around $0.50–0.75/W (Figure 2.31) for corresponding LCOE of 6¢/kWh, which will bring PV at or below grid parity in most parts of the world.

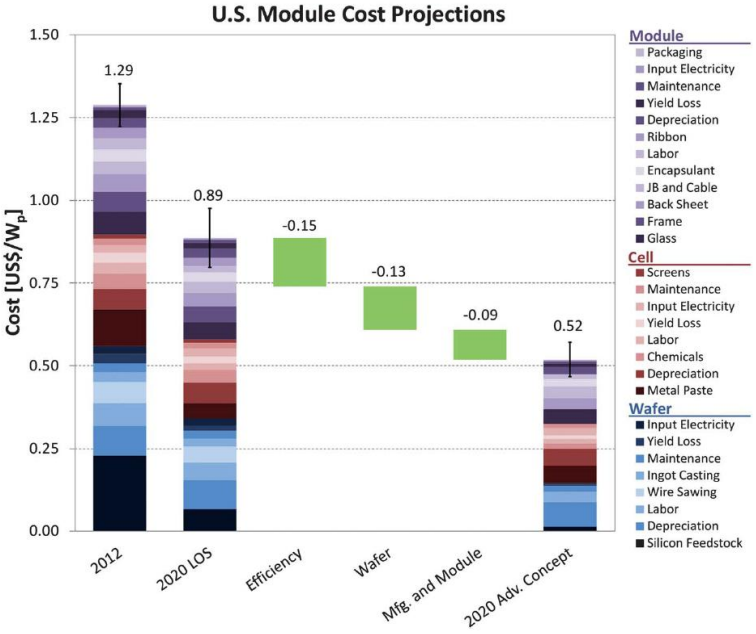

Figure 2.31: Estimated cost structure of mc-Si module.

SunShot vision study [6] from United State Department of Energy (DOE) showed all the components of installed system cost for residential, commercial, and utility PV systems in 2010 (Figure 2.32). The study pointed out that there is a huge uncertainty or distribution in the installed system price in the US.

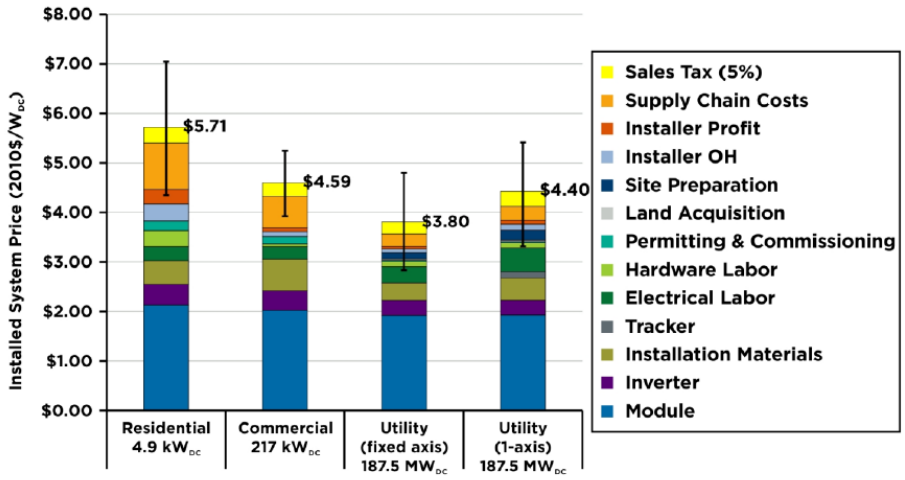

Figure 2.32: Benchmarked 2010 installed PV system costs.

Finally, Figure 2.33 from the SunShot vision study shows the LCOE values in 2010 in Phoenix and New York with and without 30% federal investment tax credit (ITC). According to this study, LCOE value in Phoenix was 21¢/kWh, 25¢/kWh, and 18¢/kWh in 2010 for residential, commercial, and utility scale PV system without federal ITC. This numbers were declined dramatically in the last two years (2011–2012) because of more than a factor of two reduction in the module price. SunShot goal is to attain an LCOE of 6¢/kWh by 2020 without any subsidies.

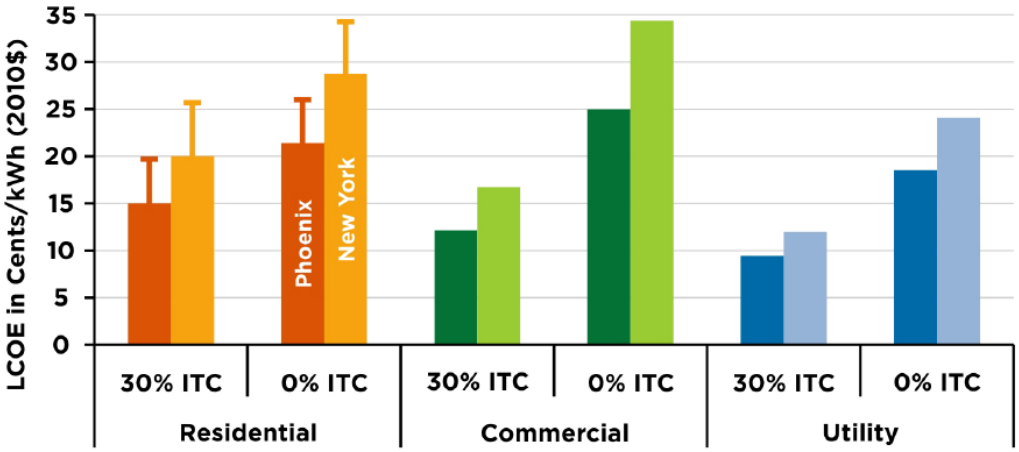

Figure 2.33: LCOE in Phoenix and New York in 2010 with and without federal ITC.

CHAPTER 3

DEPOSITION OF SILANE-FREE SiC_xN_y FILM AND ASSESSMENT OF ITS ANTIREFLECTION AND PASSIVATION PROPERTIES

In this chapter, a novel silicon-carbon-nitride (SiC_xN_y) antireflection (AR) coating was deposited from a silane-free source in an effort to reduce cost and enhance performance of silicon solar cells. Benefit of using the silane-free source is cost reduction that stems from safety and ease of handling the source. Silane (SiH_4) is dangerous, toxic, and pyrophoric and involves lots of attention and additional cost during the use and transport. SiH_4 and ammonia (NH_3) gas mixture is widely used in solar cell industry to deposit silicon-nitride (SiN_x) AR coatings for silicon solar cells. The deposition of SiC_xN_y uses a solid polymer source (Figure 3.1) developed at SiXtron Advanced Materials Inc. The solid source consists of a safe and stable polymer that is heated inside a sealed pressure vessel (SunBox).

The polymer undergoes a thermally activated exothermic decomposition at a specific temperature and pressure. During this decomposition, a gas is produced which pressurizes the vessel. The vessel is then used as a gas reservoir, and the gas delivery is controlled by a standard gas panel. The gas evolved contains various molecular species including silicon (Si), carbon (C), and hydrogen (H). The gas is supplied to a standard plasma-enhanced chemical-vapor deposition (PECVD) reactor, in place of silane, through a standard silane mass flow controller assuming the same correction factor as used for silane. It was found that neither a gas condensation nor a liquid formation problem occurred in the gas delivery system.

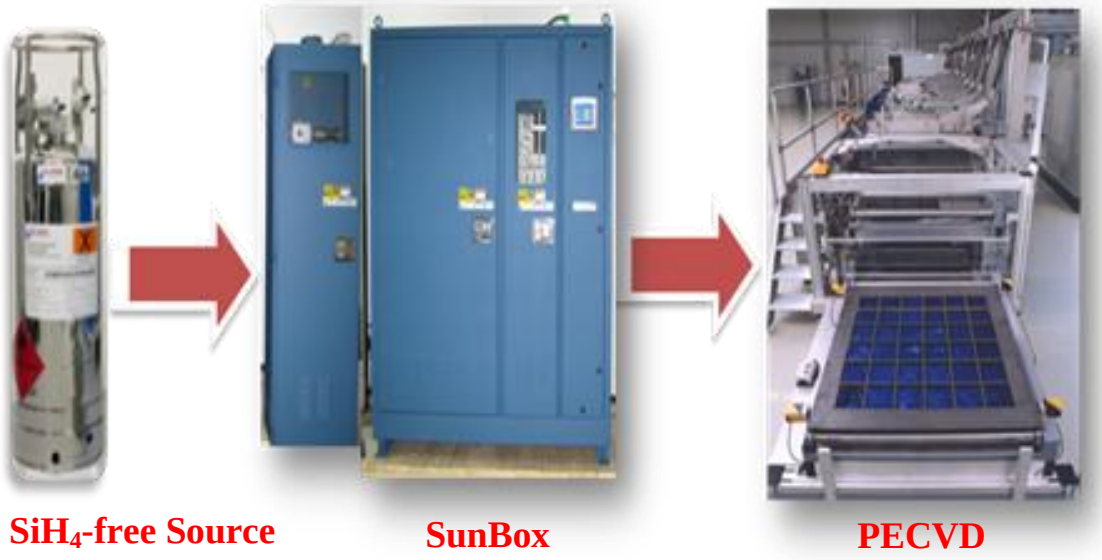

Figure 3.1: SiXtron's technology consists of SiH_4-free source, SunBox gas generation/delivery system, and deposition processing at the existing PECVD platform.

This chapter deals with optimization of deposition parameters and electrical and optical properties of the novel SiC_xN_y films for Si solar cell applications. The SiC_xN_y films were deposited in a low frequency (50 kHz) PECVD reactor with NH_3 and gas produced from a solid polymer source. Counterpart SiN_x films used in photovoltaics industry were also deposited in the same chamber using SiH_4 and NH_3 gases for comparison. Hundreds solar cells were fabricated with SiC_xN_y AR coating on 2 Ω-cm p-type textured Czochralski (Cz) Si wafers as well as 1 Ω-cm lower-cost and defective multi-crystalline (mc) Si wafers, which are known to benefit from SiN_x-induced hydrogen passivation of defects.

3.1 Effect of NH_3 gas flow rate on composition of SiC_xN_y films

Figure 3.2 shows the Si/C/N/O chemical composition of SiC_xN_y films as a function of NH_3 gas flow rate. These films were analyzed by Auger X-ray photoelectron

spectroscopy. Other deposition parameters including the flow rate of polymer gas source (300 sccm), deposition temperature (425℃), pressure (2 torr), and plasma power (150 W) were fixed. Figure 3.2 shows that no carbon was detected in the SiN_x film formed with the conventional SiH_4 gas. However, in the case of SiC_xN_y films deposited with the solid polymer source, the nitrogen (N) composition in the film increases with the increase in NH_3 gas flow rate while the carbon content decreases. The Si fraction in the SiC_xN_y films remains constant (around 31%), irrespective of the NH_3 gas flow rate. Thus, the carbon composition can be changed without affecting the Si composition by adjusting the NH_3 gas flow rate. Therefore the NH_3 flow rate serves as a tool to adjust the chemical composition of the SiC_xN_y film.

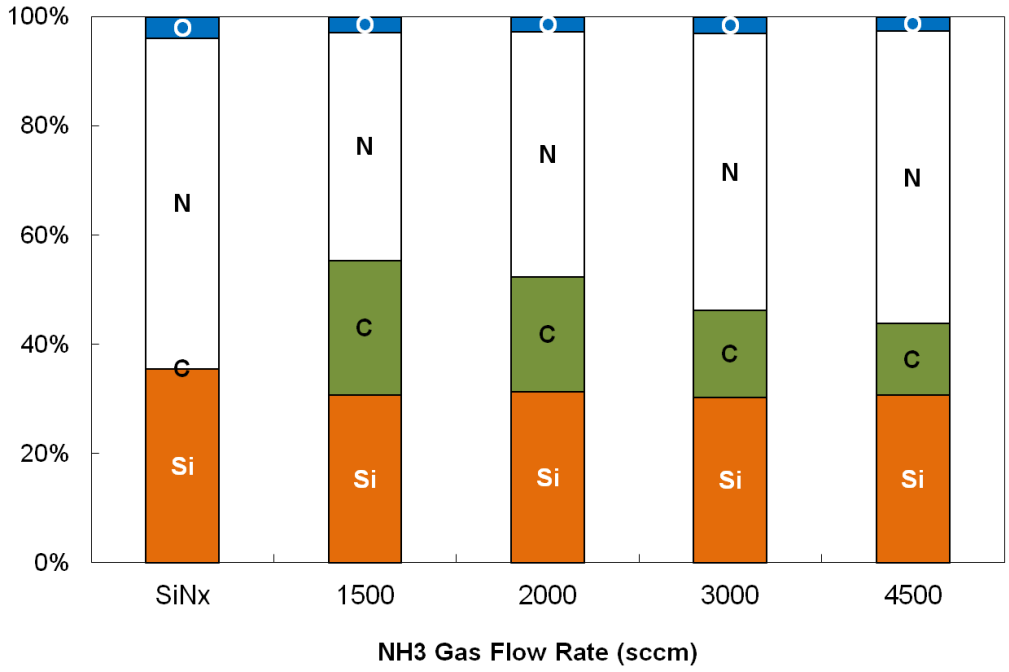

Figure 3.2: Chemical composition of SiC_xN_y films as a function of NH_3 flow rate.

Figure 3.3 shows hydrogen concentration of SiC_xN_y films as a function of NH_3 gas flow rate measured by elastic recoil detection. Figure 3.3 shows higher hydrogen content in conventional SiN_x film than the SiC_xN_y films deposited with the 3000 sccm NH_3 flow rate. Hydrogen content decreases in the SiC_xN_y films with increasing NH_3 gas flow rate. Although the SiN_x films show higher hydrogen content at the same NH_3 flow rate, SiC_xN_y films should be able to supply enough hydrogen to passivate defects in the bulk and Si/SiC_xN_y interface during the contact firing.

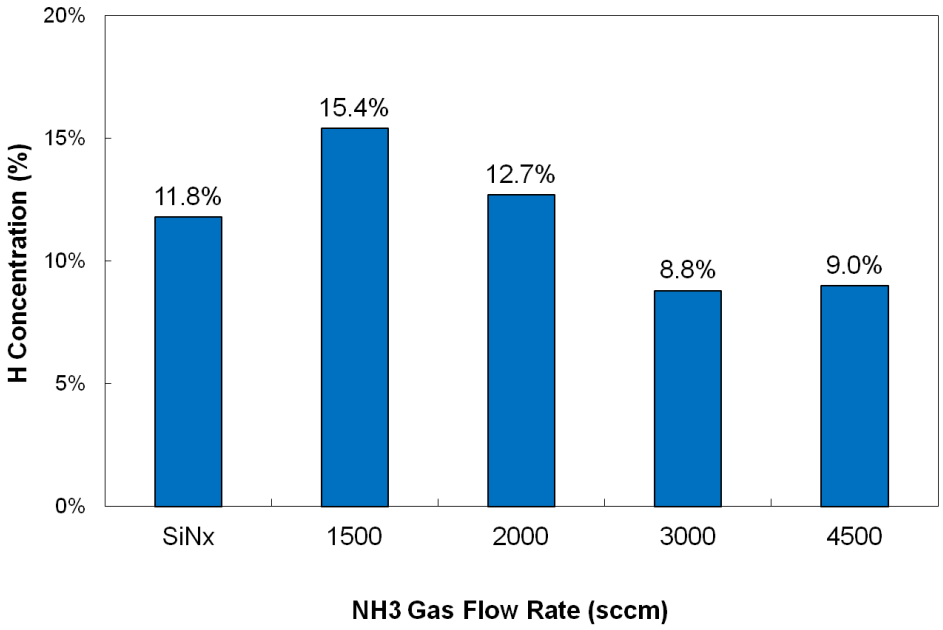

Figure 3.3: Hydrogen concentration of SiC_xN_y films as a function of NH_3 flow rate.

3.2 Optical properties of SiC_xN_y films

Both refractive index (n) and extinction coefficient (k) are important for antireflection properties. Index and thickness combination determines reflection, and extinction coefficient determines absorption inside the film. Figure 3.4 shows that both n and k of the SiC_xN_y films decrease with an increase in NH_3/Polymer gas flow rate ratio, and

higher deposition temperature provides higher index. J. A. Woollam Co. Inc. variable angle spectroscopic ellipsometer was used to measure the n and k values. The n and k values were measured at the wavelengths of 630 and 300 nm, respectively. By adjusting the NH_3/Polymer gas flow rates, SiC_xN_y films with a refractive index in the range of 1.93–2.00 at a wavelength of 630 nm can be obtained [52] which is required for a good AR coating.

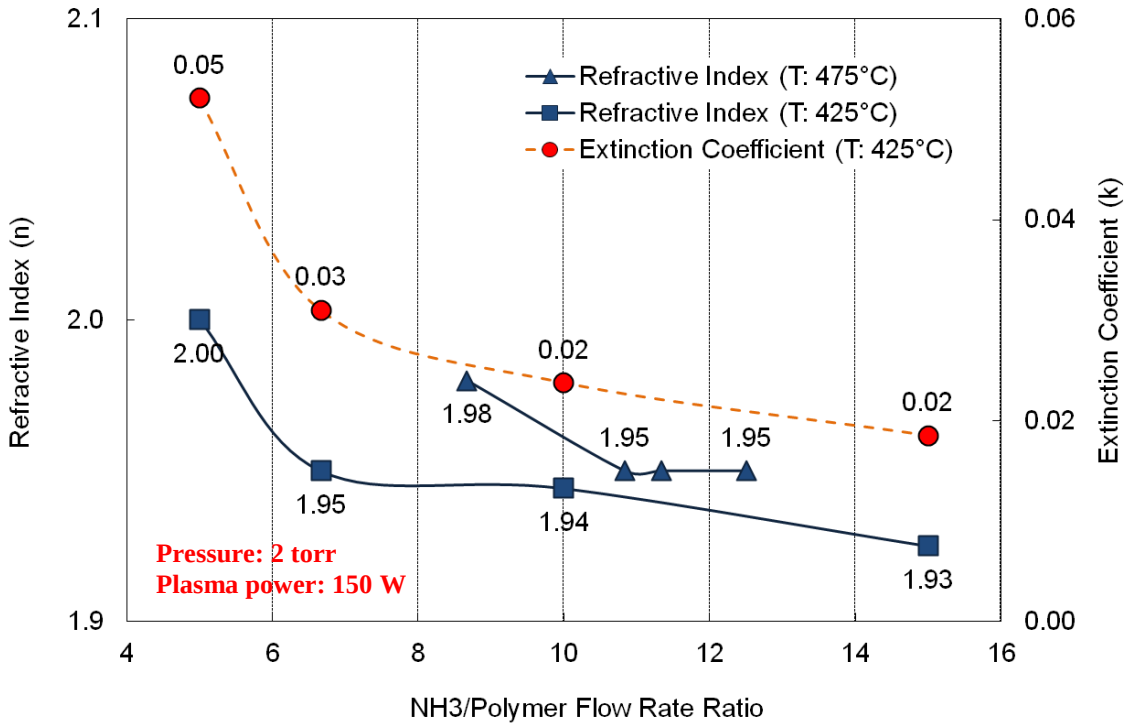

Figure 3.4: Refractive indexes (n) and extinction coefficient (k) of SiC_xN_y films as a function of NH_3/polymer flow rate ratio.

Investigation of optical properties of SiC_xN_y films was also done as a function of plasma power (Figure 3.5). It was observed that there was no significant difference in optical properties for plasma power in the range of 150–250 W which provides n of ~1.94 and k of ~0.01 in that range.

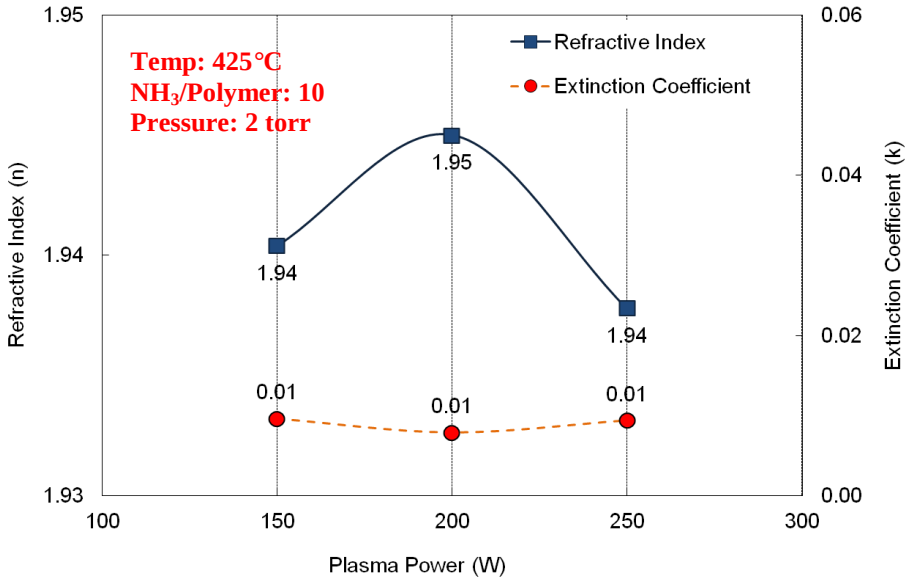

Figure 3.5: Refractive index (n) and extinction coefficient (k) of SiC_xN_y films as a function of plasma power.

3.3 Emitter passivation quality of SiC_xN_y films

Besides low reflection and absorption, AR coating should also provide a good emitter surface passivation for achieving high-efficiency solar cells. Better surface passivation improves short wavelength response and also lowers emitter saturation current (J_{oe}) to provide higher short circuit current (J_{sc}) and open circuit voltage (V_{oc}). Figure 3.6 compares the J_{oe} values for the silane-deposited SiN_x film and the silane-free SiC_xN_y film on 45, 60, and 80 Ω/sq emitters on planar wafers. Samples were annealed in a rapid thermal processing (RTP) chamber at 800°C for 2 sec. Both films show similar J_{oe} values for the 45 and 60 Ω/sq emitters, but the conventional SiN_x showed a lower value of J_{oe} than the SiC_xN_y for the 80 Ω/sq emitter [53]. This suggests the presence of carbon in the SiC_xN_y films may interfere with the hydrogen release from the film and negatively affect the passivation quality of the Si surface. However, with a thin thermally grown SiO_2 at

the interface prior to SiN_x deposition which is often done for good passivation, the J_{oe} gap decreased for the 80 Ω/sq emitter. This also suggests that the hydrogen released from the SiC_xN_y film can decrease the interface trap density at the Si/SiO_2 interface during the contact firing, as is the case for conventional SiN_x films.

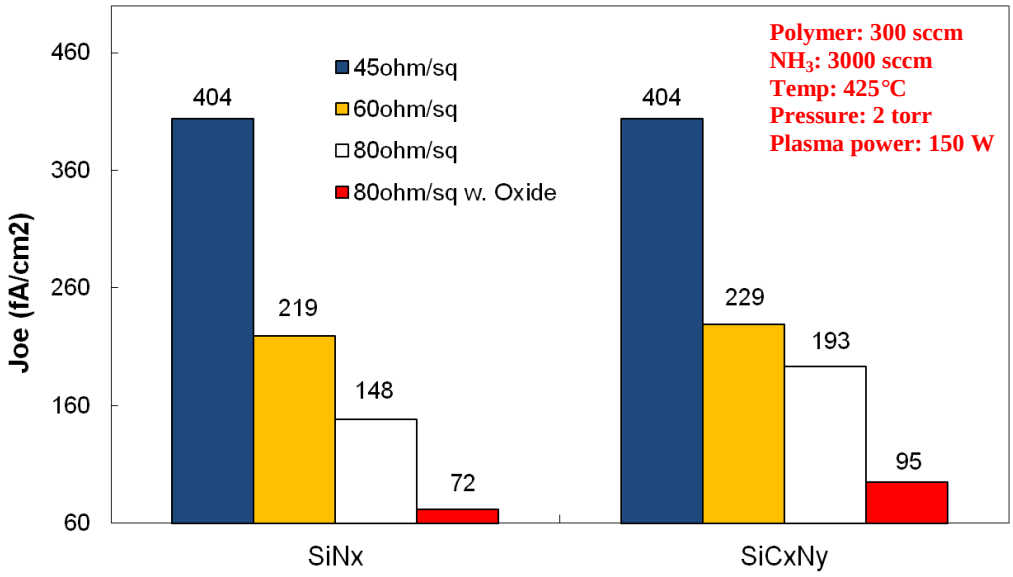

Figure 3.6: J_{oe} values of 45, 60, and 80 Ω/sq emitters.

3.4 Surface charge and interface trap densities in SiC_xN_y films

High charge and low interface defect density is desirable for good surface passivation. Therefore, an investigation was carried out to study these two parameters in both SiN_x and SiC_xN_y films. SemiTest SCA-2500 surface charge analyzer was used to measure the charge density in the dielectrics. This tool allowed contactless and nondestructive measurement of the flat-band charge density (Q_{fb}, the total charge density for the flat-band condition) in the dielectric of interest. The surface charge density in dielectrics

plays a critical role in controlling the surface passivation and solar cell performance [54]. Figure 3.7 shows the surface charge density (Q_{fb}) as a function of NH_3 flow rate after annealing in an RTP chamber at 800℃ for 2 sec. The surface charge density in SiC_xN_y films was found to be strongly depended on the NH_3 gas flow and is positive in nature. Figure 3.7 shows that the positive surface charge density was in the range of (1.58–1.77) × 10^{12} cm^{-2}, which is slightly lower than that of the conventional SiN_x film (1.86 × 10^{12} cm^{-2}) for these specific samples but high enough to provide equivalent passivation quality with SiN_x film.

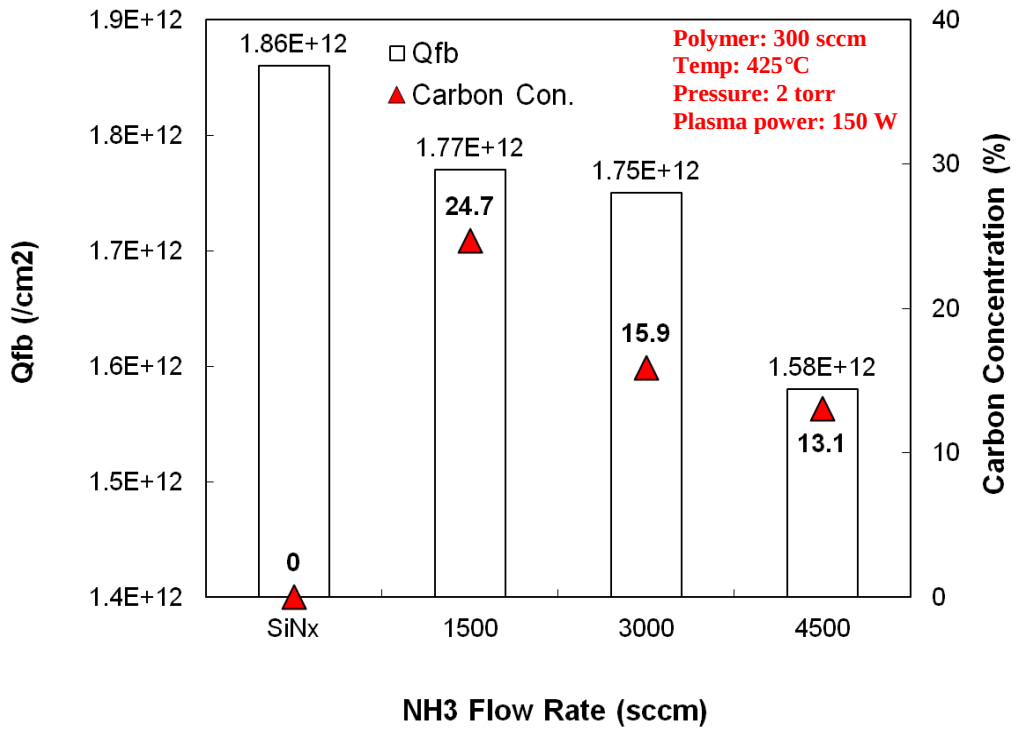

Figure 3.7: Surface charge density in SiC_xN_y films as a function of NH_3 gas flow rate.

Figure 3.8 shows the surface charge density is also a strong function of plasma power. The positive surface charge density in the SiC_xN_y films varied in the range of (1.81–2.10)

× 10^{12} cm^{-2} but was again slightly lower than that of the conventional SiN_x film (2.41 × 10^{12} cm^{-2}) for these specific samples. It is important to recognize that the positive charge density was high enough to provide good quality surface passivation.

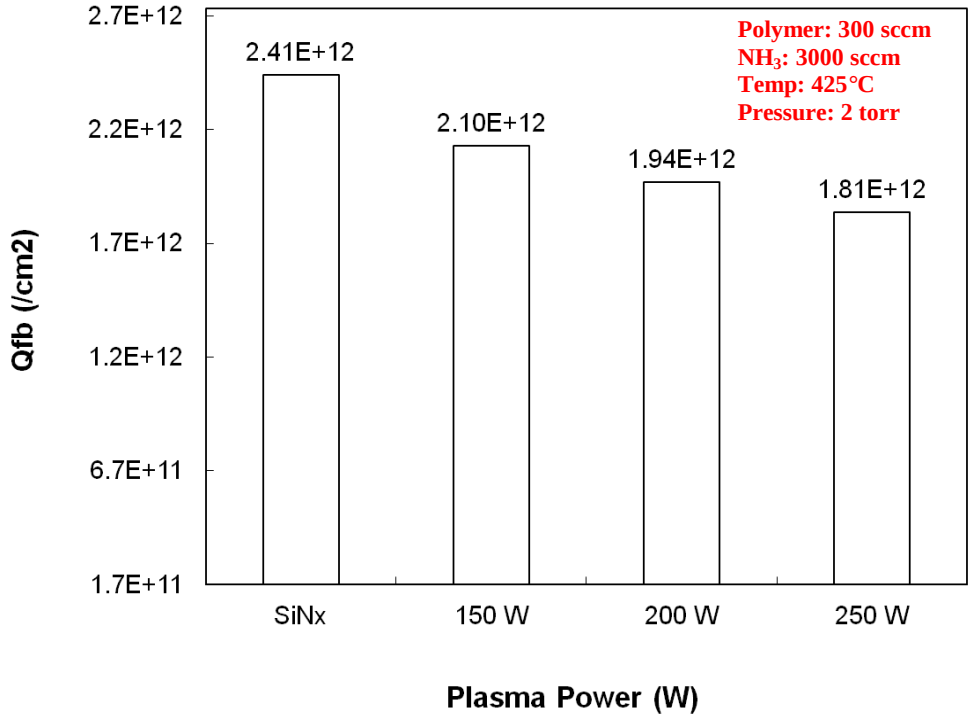

Figure 3.8: Surface charge density in SiC_xN_y films as a function of plasma power.

Figure 3.9 shows the interface trap density (D_{it}) at the Si/dielectric film interface as a function of NH_3 flow rate after annealing in an RTP chamber at 800℃ for 2 sec. It was found that the trap density decreases as carbon content decreases. This suggests that a low carbon concentration is desirable to achieve a good surface passivation. However, increasing the NH_3 flow rate to reduce the carbon content increases the nitrogen content and decreases the refractive index below the desirable range (< 2). This resulted in an optimum NH_3 flow rate of ~3000 sccm which gave the right compromise between

refractive index and trap density which in turn control the reflection and passivation, respectively.

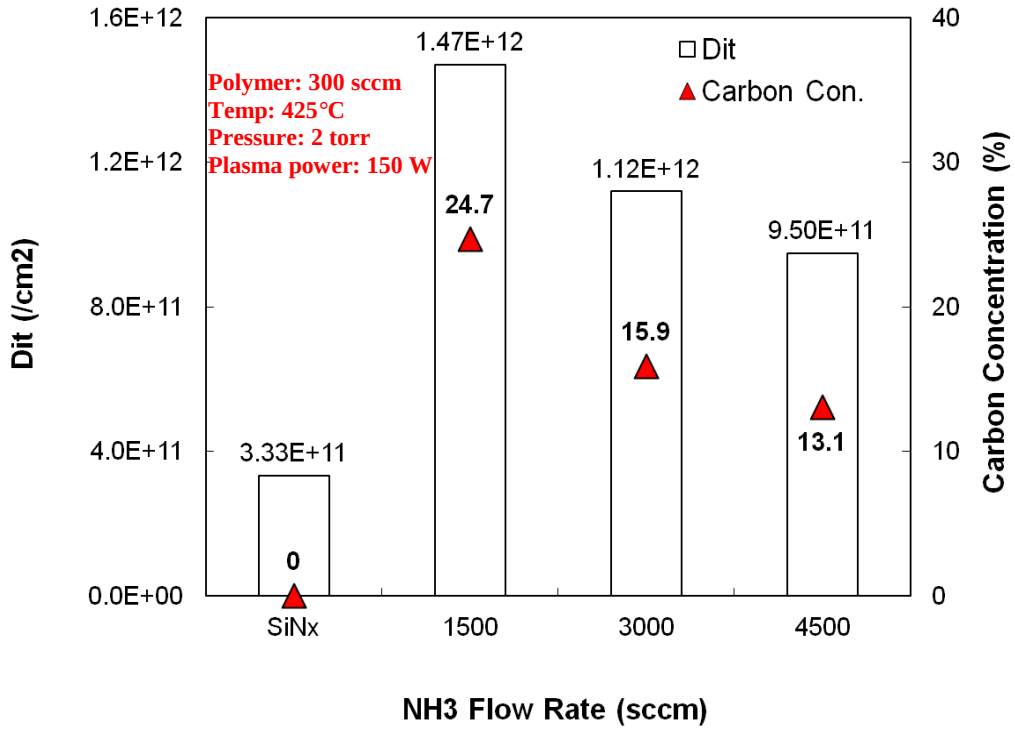

Figure 3.9: Interface trap density in SiC_xN_y films as a function of NH_3 flow rate.

Figure 3.10 shows the interface trap density at the Si/dielectric film interface as a function of plasma power after annealing in an RTP chamber at 800℃ for 2 sec. It was observed that the trap density decreases as plasma power increases. This suggests that higher plasma power is desirable to achieve a better surface passivation.

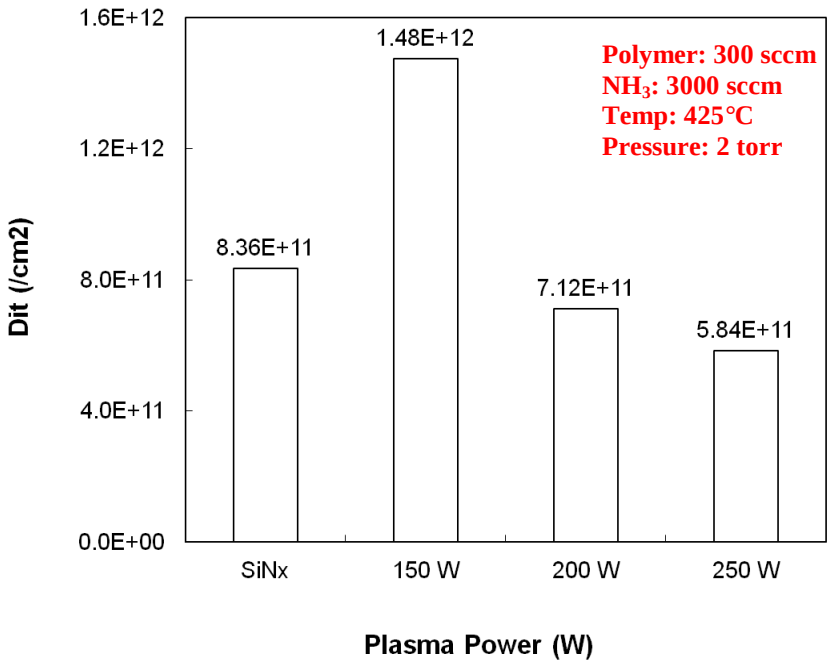

Figure 3.10: Interface trap density in SiC_xN_y films as a function of plasma power.

3.5 Fabrication of high-efficiency Si solar cells with SiC_xN_y AR coating

Since the objective is to develop a low-cost silane-free source for AR coating without compromising solar cell efficiency, complete large-area commercial ready cells with SiC_xN_y as well as conventional SiN_x films were fabricated in this section. Both Cz (~2 Ω-cm) and mc-Si (~1 Ω-cm) screen-printed full aluminum-back-surface field solar cells were fabricated. SiC_xN_y films with varying compositions were investigated for AR coating and emitter surface passivation. Figure 3.11 shows SiC_xN_y-coated Cz solar cell efficiency as a function of NH_3 flow rate. NH_3 flow rate of 3000 sccm provided the best conversion efficiency of 16.9%, which is 0.1% lower than the conventional SiN_x-coated solar cell.

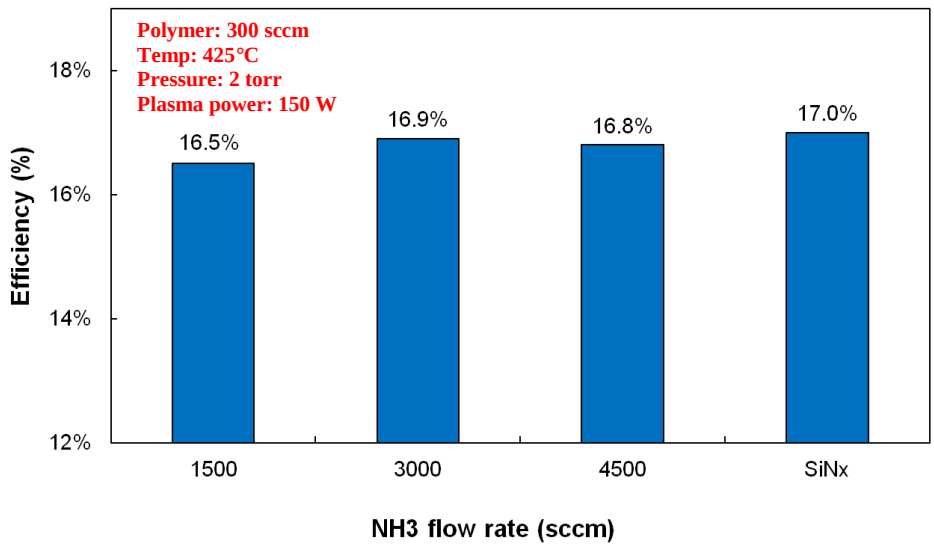

Figure 3.11: Solar cell efficiency of SiC_xN_y- and SiN_x-coated solar cells as a function of NH_3 flow rate.

Tables 3.1 and 3.2 show the key parameters of the solar cells with AR coating deposited using silane and the polymer source. Notice that polymer and NH_3 flow rate were fixed at 300 and 3000 sccm, respectively because the best cell results were obtained with that. Plasma power of 150 W, temperature of 425℃, and pressure of 2 torr were also fixed for Tables 3.1 and 3.2. A cell efficiency of 17.4% was achieved with an 80 Ω/sq emitter on the solar cells with a stack of SiO_2/SiC_xN_y coating. For 45 and 60 Ω/sq sheet emitters, both SiN_x and SiC_xN_y provided cells with comparable J_{sc}, V_{oc}, but the fill factor (FF) was slightly lower for the SiN_x films resulting in a 0.1% efficiency difference. However, for the high sheet emitter (80 Ω/sq), the V_{oc} of cells with the conventional SiN_x film was 11 mV higher than the cells with the SiC_xN_y film, resulting in a 0.2% lower cell efficiency. This large difference in the V_{oc} is attributed to a superior or lower J_{oe} (Figure 3.6) of the SiN_x film due to better surface passivation. Higher sheet resistance cells are more sensitive to surface passivation quality. The comparable J_{sc} supports the good

optical properties for the SiC_xN_y films. In order to improve the surface passivation of SiC_xN_y-coated cells, ~100 Å oxide was grown on the emitter surface prior to nitride deposition. This stack passivation reduced the V_{oc} gap from 11 to 7 mV but not to zero.

Table 3.1: Performance of 149 cm^2 Cz solar cells with industrial-type phosphorus diffused 45, 60, and 80 Ω/sq emitters.

	SiN_x-coated solar cells				SiC_xN_y-coated solar cells			
Emitter (Ω/sq)	V_{oc} (mV)	J_{sc} (mA/cm²)	FF	Eff (%)	V_{oc} (mV)	J_{sc} (mA/cm²)	FF	Eff (%)
45	624	35.1	0.777	17.0	622	34.8	0.780	16.9
60	620	36.1	0.763	17.1	618	35.8	0.766	17.0
80	623	36.3	0.767	17.4	612	36.2	0.775	17.2
80*	632	36.2	0.770	17.6	625	36.1	0.772	17.4

* With oxide stack passivation

Table 3.2: Performance of 156 cm^2 mc-Si solar cells with industrial-type phosphorus diffused 45 Ω/sq sheet resistance emitter.

	V_{oc} (mV)	J_{sc} (mA/cm²)	FF	Eff (%)
SiN_x	614	32.0	0.773	15.2
SiC_xN_y	612	31.4	0.775	14.9

Figure 3.12 shows the internal quantum efficiency (IQE) and front surface reflectance of the two types of cells (SiN_x and SiC_xN_y coated) with 60 and 80 Ω/sq emitters. In the short wavelength range, the IQE of the 60 Ω/sq emitters are comparable suggesting comparable surface passivation. However, the 80 Ω/sq emitter coated with SiN_x showed a higher IQE compared to SiC_xN_y-coated cells, indicating a better surface passivation which is consistent with the higher V_{oc} value. Notice that the long wavelength response for both types of cells is identical for all the emitters, indicating bulk lifetime

preservation or equivalent hydrogen passivation of bulk defects in Cz Si via SiC_xN_y film. Therefore, the SiC_xN_y films can replace the SiN_x films but with a slight loss in solar cell performance, resulting in cost, safety, and efficiency tradeoff.

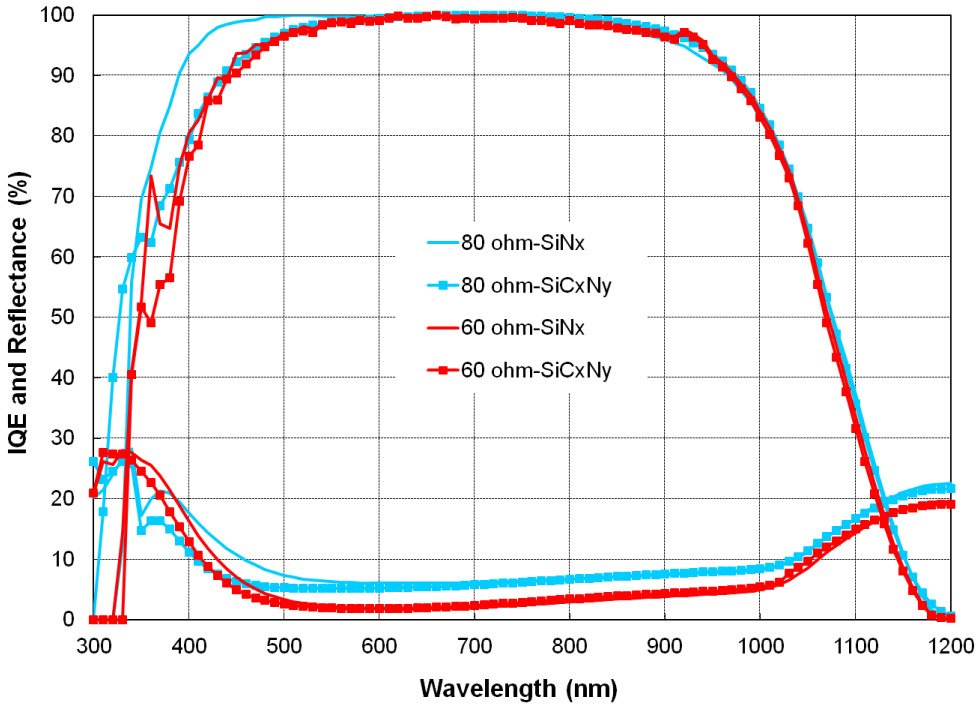

Figure 3.12: IQE responses of the solar cells with SiN_x and SiC_xN_y AR layer with 60 and 80 Ω/sq emitters.

In an effort to improve the surface passivation of SiC_xN_y films, plasma power was varied during the deposition. Figure 3.13 shows solar cell efficiency as a function of plasma power. It is found that passivation quality of SiC_xN_y improves as plasma power increases as supported by the IQE curves in Figure 3.14. Solar cells were made on 45 Ω/sq emitter. Plasma power of 150 W gave inferior surface passivation and 16.7% cell efficiency. However, with the plasma power of 250 W, SiC_xN_y-coated solar cells provided same conversion efficiency as SiN_x-coated cell which was 17.2%.

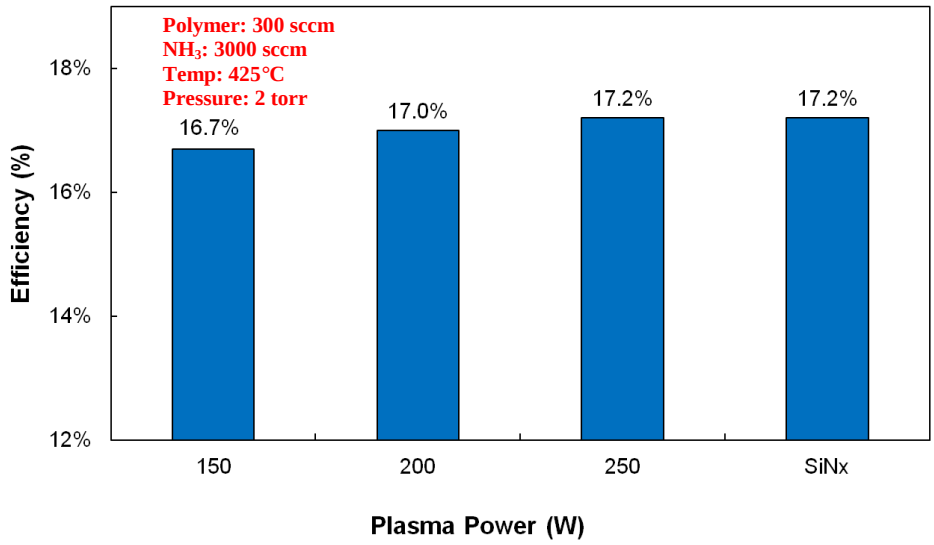

Figure 3.13: Solar cell efficiency of SiC_xN_y- and SiN_x-coated solar cells as a function of plasma power.

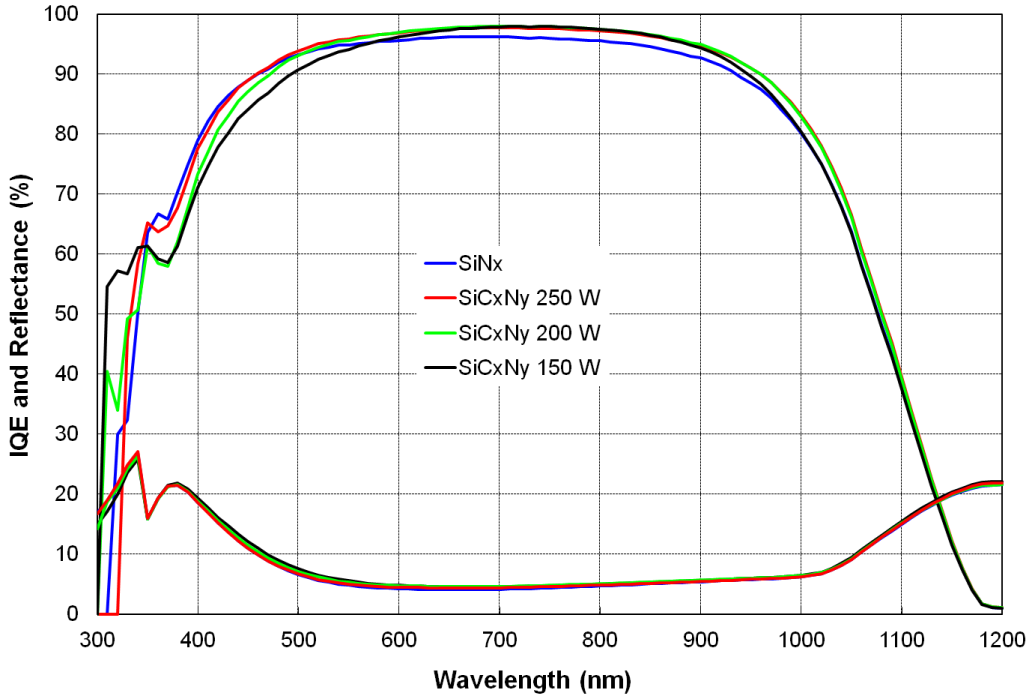

Figure 3.14: IQE responses of the solar cells with SiN_x and SiC_xN_y AR layer with different plasma power.

3.6 Conclusion

A silane-free solid polymer source was developed at SiXtron Advanced Materials to eliminate the dangerous pyrophoric silane gas in a manufacturing line. The polymer source can be shipped which significantly reduces handling and gas transport issues associated with silane gas. The electrical and optical properties of the SiC_xN_y films were studied and compared with the conventional SiN_x film formed with silane gas as a silicon source. The ratio of carbon to nitrogen (C/N), hydrogen content, refractive index, and extinction coefficient of the SiC_xN_y films were found to decrease with the increase in the NH_3 flow rate. High surface charge density and hydrogen concentration, provided comparable surface passivation and J_{oe} values of ~4×10^{-13} A/cm^2 on a 45 Ω/sq emitter cells. However, J_{oe} values of SiC_xN_y-coated cells were slightly higher on the 80 Ω/sq emitter, resulting in 11 mV loss in V_{oc} and ~0.2% loss in cell efficiency. Thus, there is a slight tradeoff in efficiency, but the solid polymer source for SiC_xN_y can provide considerable safety and cost benefits compared to SiN_x films grown by silane gas.

CHAPTER 4

SiC_xN_y-INDUCED REDUCTION OF LIGHT-INDUCED DEGRADATION IN CZ SILICON SOLAR CELL EFFICIENCY

As mentioned in Chapter 2.5, carbon incorporation into the bulk silicon (Si) could reduce light-induced degradation (LID). In Chapter 4, the process-induced incorporation of carbon into the bulk Si with silicon-carbon-nitride (SiC_xN_y) film is investigated. Diffused carbon in the bulk competes with boron and effectively reduces the concentration of boron-oxygen ($B\text{-}O_{2i}$) complex, which is the source of LID in Czochralski (Cz) solar cells. As a result, SiC_xN_y-coated solar cells have the potential to show less LID than solar cells coated with silicon-nitride (SiN_x) film. Solar cells were fabricated using boron-doped p-type ~2 Ω-cm resistivity Cz Si wafers with an oxygen concentration of ~7×10^{17} cm^{-3}. Finished solar cells were measured before and after 72 hours of illumination with an intensity of 0.1 Sun (100 W/m^2) to investigate the LID.

4.1 Study of carbon diffusion from SiC_xN_y films

Secondary ion mass spectrometry (SIMS) data shown in Figure 4.1 confirms that the plasma-enhanced chemical-vapor deposition (PECVD) of SiC_xN_y film on Si at 400–500℃ followed by ~800℃ contact firing injects appreciable amount of carbon from the SiC_xN_y film into the bulk Si wafer. The error-function-like carbon profile observed for the SiC_xN_y-coated cells is indicative of carbon diffusion [55] with surface concentration of 5×10^{20} cm^{-3}. Notice that there is no appreciable carbon diffusion in the SiN_x-coated cells. Even though the carbon concentration in Figure 4.1 appears to level off after 140

nm at the SIMS detection limit of 10^{17} cm^{-3}, it is believed that carbon is present deeper in the bulk Si because diffusion profiles decrease monotonically and do not end abruptly.

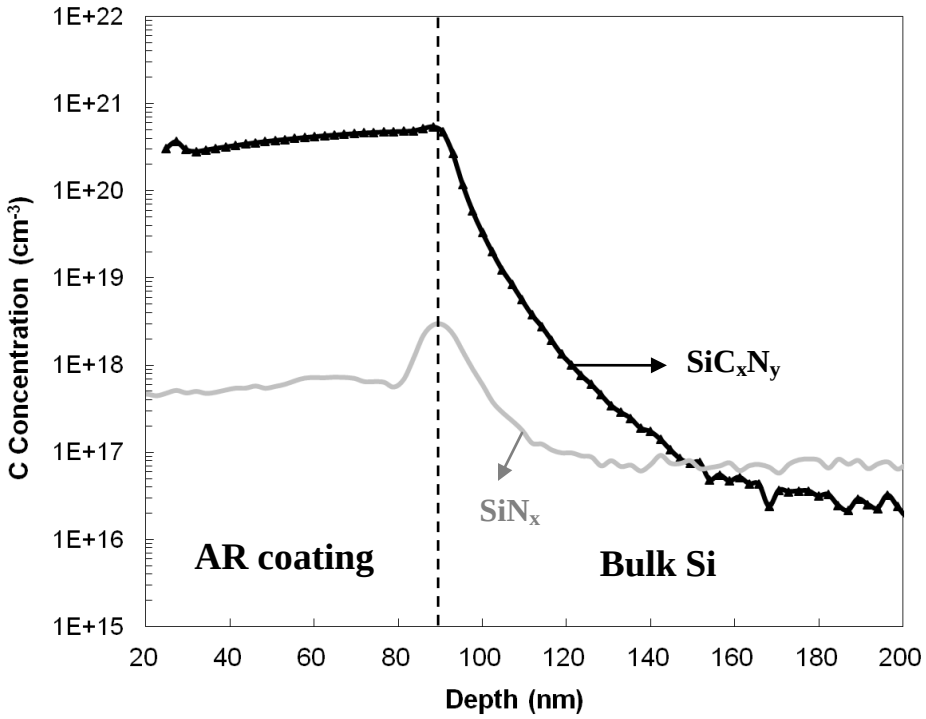

Figure 4.1: SIMS profile of carbon diffusion inside the Cz wafers after short time (2 sec) high temperature annealing (800℃).

The theoretical calculation in Figure 4.2 shows that free carbon can diffuse monotonically to 50 μm depth in Si during the rapid (2 sec) firing at 800℃ because of the low activation energy of 0.73 eV for carbon diffusion in Si [56]. This low activation energy assumes interstitial carbon diffusion via kick-out mechanism as proposed by Frank-Turnbull. In the case of SiC_xN_y-coated solar cells, carbon at Si/SiC_xN_y interface may require additional energy for dissociation and release prior to diffusion. This additional energy may explain why the measured carbon-diffusion profile shown in

Figure 4.1 appears shallower and steeper compared to the theoretical profile (Figure 4.2) and levels off at the SIMS detection limit.

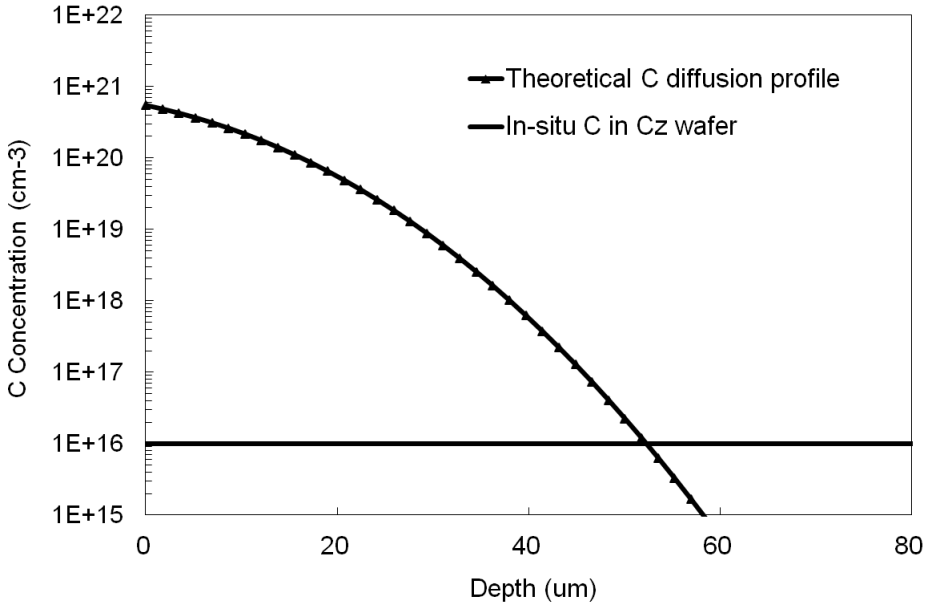

Figure 4.2: Theoretical calculation of carbon diffusion inside the Cz wafers after short time (2 sec) high temperature annealing (800°C).

LID is attributed to B-O_{2i} metastable complexes [41, 43, 57], which are formed under illumination when oxygen (O) dimmers migrate to boron (B). Based on the literature, carbon (C) can also form C-O_{2i} pairs [58, 59] in the presence of oxygen. The literature confirms the evidence of C-O complex formation by Fourier transform infrared spectroscopy (FTIR) [60] and photoluminescence (PL) measurements [61]. It has been suggested [62-65] that carbon may co-precipitate with oxygen, leading to C-O agglomerates. All these studies support that the presence of carbon can steal some of the oxygen dimmers from boron and lead to reduced LID in the SiC_xN_y-coated cells (Figure 4.3).

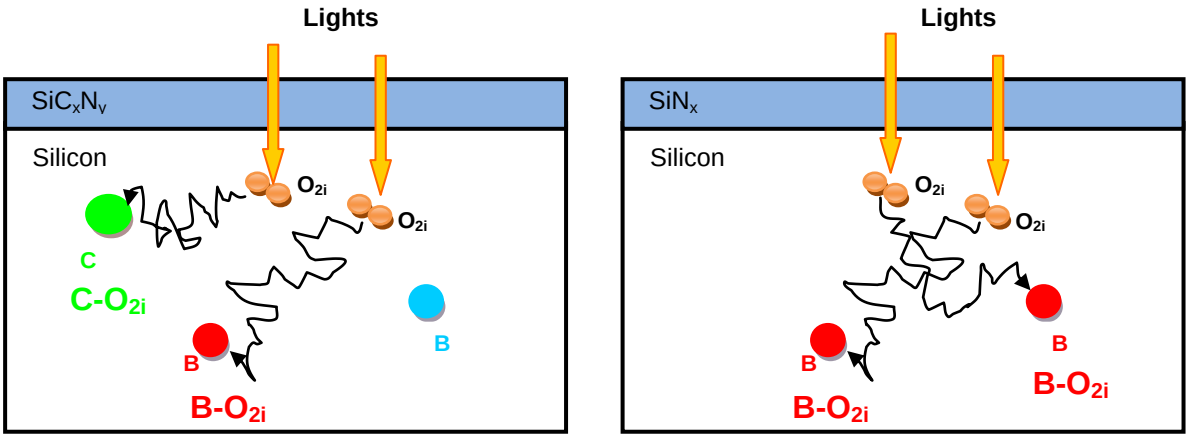

Figure 4.3: A schematic of light-induced degradation mechanism in SiC_xN_y- and SiN_x-coated solar cells. Some number of oxygen dimers, driven by light, diffuses in the bulk Si to form C-O_{2i} and B-O_{2i} complexes. Fewer B-O_{2i} are formed in the presence of carbon.

4.2 Solar cell results with SiC_xN_y AR coatings

Solar cells were fabricated on 2 Ω-cm boron doped p-type Cz substrates with both SiN_x and SiC_xN_y antireflection (AR) coatings to investigate the magnitude of LID after several hours of illumination. Figure 4.4 illustrates the change in efficiency, open circuit voltage (V_{oc}), and short circuit current (J_{sc}) as a function of illumination time. In this study, SiC_xN_y-coated 2 Ω-cm base resistivity solar cell showed 0.04% efficiency drop compared with 0.34% efficiency loss for the SiN_x-coated solar cell after several hours of light exposure. SiN_x-coated solar cells showed 3 mV drop in V_{oc} and 0.4 mA/cm^2 loss in J_{sc}. The counterpart SiC_xN_y-coated solar cells showed smaller LID with a 2 mV decrease in V_{oc} and 0.1 mA/cm^2 loss in J_{sc}. Therefore, SiC_xN_y-coated cell efficiency after LID is equal to or higher than SiN_x-coated cells in spite of slightly higher initial efficiency (~0.2%) of the SiN_x-coated solar cells because of better surface passivation. Thus, reduced LID in SiC_xN_y-coated cells bridged the initial efficiency gap between the two coatings.

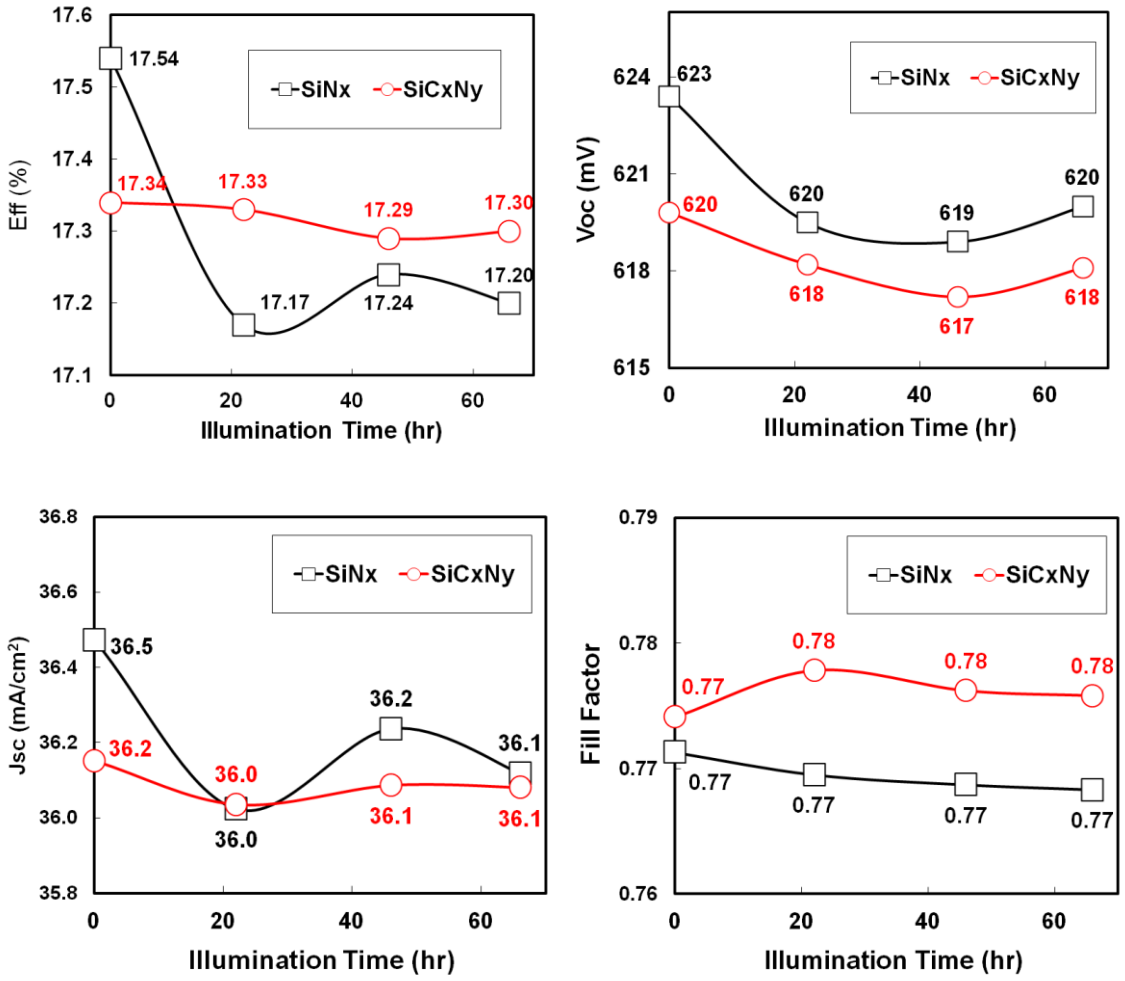

Figure 4.4: Efficiency, V_{oc}, J_{sc}, and fill factor trend curves as a function of illumination time for 2 Ω-cm boron doped Cz cells with SiN_x and SiC_xN_y AR coatings.

A large number of SiN_x- and SiC_xN_y-coated solar cells were fabricated on boron doped Cz wafers to investigate the statistical variation in LID. The statistical degradation of 22 SiN_x- and 37 SiC_xN_y-coated boron doped Cz (oxygen ~7×10^{17} cm^{-3}) solar cells after 72 hours of light exposure are summarized in Figure 4.5. As shown in Figure 4.5, SiC_xN_y-coated solar cells suffered an average loss of 0.1% in absolute efficiency compared to 0.3% loss in efficiency for the SiN_x-coated cells. In addition, the LID-induced loss in V_{oc} and J_{sc} of the SiN_x-coated cells was approximately twice that of the SiC_xN_y-coated cells.

Quantitatively 59% of SiN_x-coated solar cells suffered a loss of 0.3–0.6% in absolute efficiency after the LID, while 75% of SiC_xN_y-coated solar cells showed a LID of < 0.1% and 32% cells with no LID. Reduced LID nearly makes up for the ~0.2% lower initial efficiency of the SiC_xN_y-coated cells compared to SiN_x-coated cells [66].

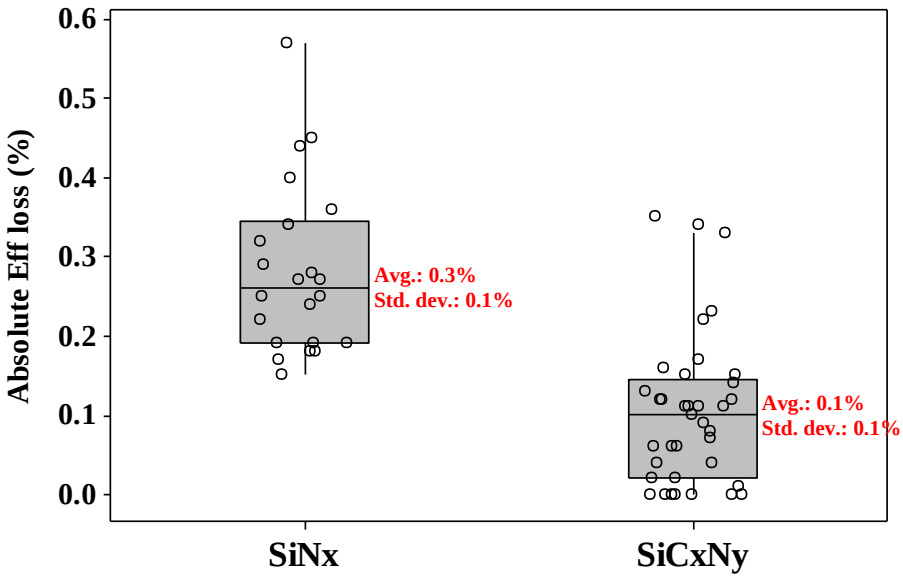

(a)

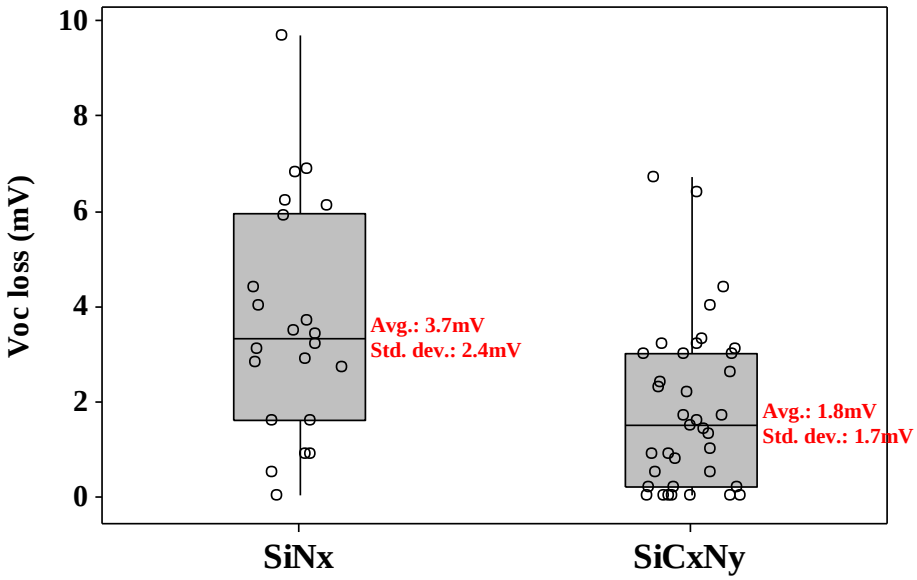

(b)

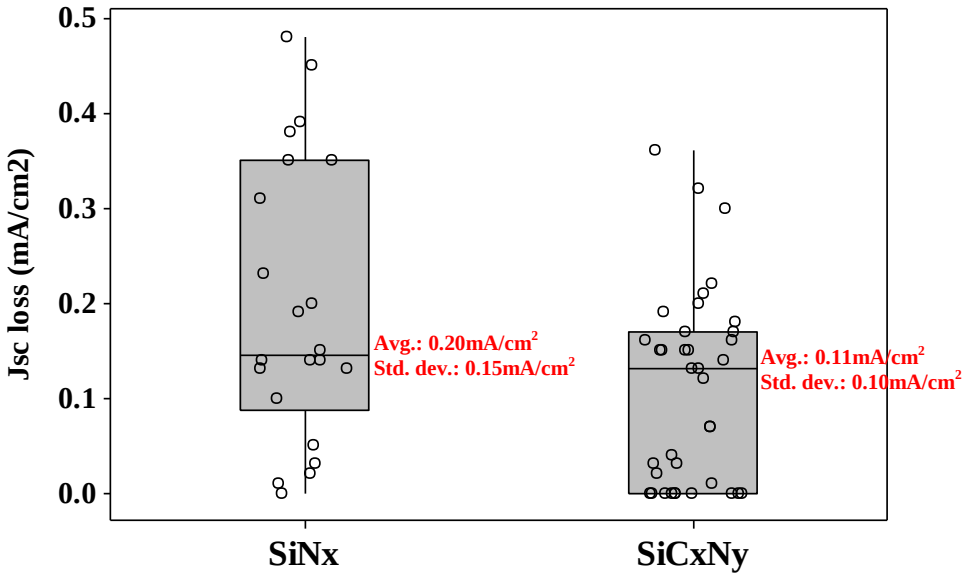

(c)

Figure 4.5: Statistical plot of (a) efficiency, (b) V_{oc}, and (c) J_{sc} degradation after several hours of illumination of boron doped Cz solar cells with SiN_x or SiC_xN_y AR coating.

4.3 PC1D device simulations to understand LID in SiC_xN_y films

To provide better insight into the LID phenomena in the two type of cells, internal quantum efficiency (IQE) (Figure 4.6) and bulk lifetime (Figure 4.7) measurements were performed in the finished cells before and after the LID. Measured bulk lifetime was used to match the measured short and long wavelength response to extract front and back surface recombination velocities (FSRV and BSRV). It was found that LID has no effect on the FSRV and BSRV values, so bulk-lifetime degradation must largely account for the LID effect. Figure 4.6 shows that the FSRV value was much lower in the case of SiN_x-coated cell (45,000 cm/s as opposed to 75,000 cm/s) which explains the ~0.2% higher pre-LID efficiency of the SiN_x-coated cells.

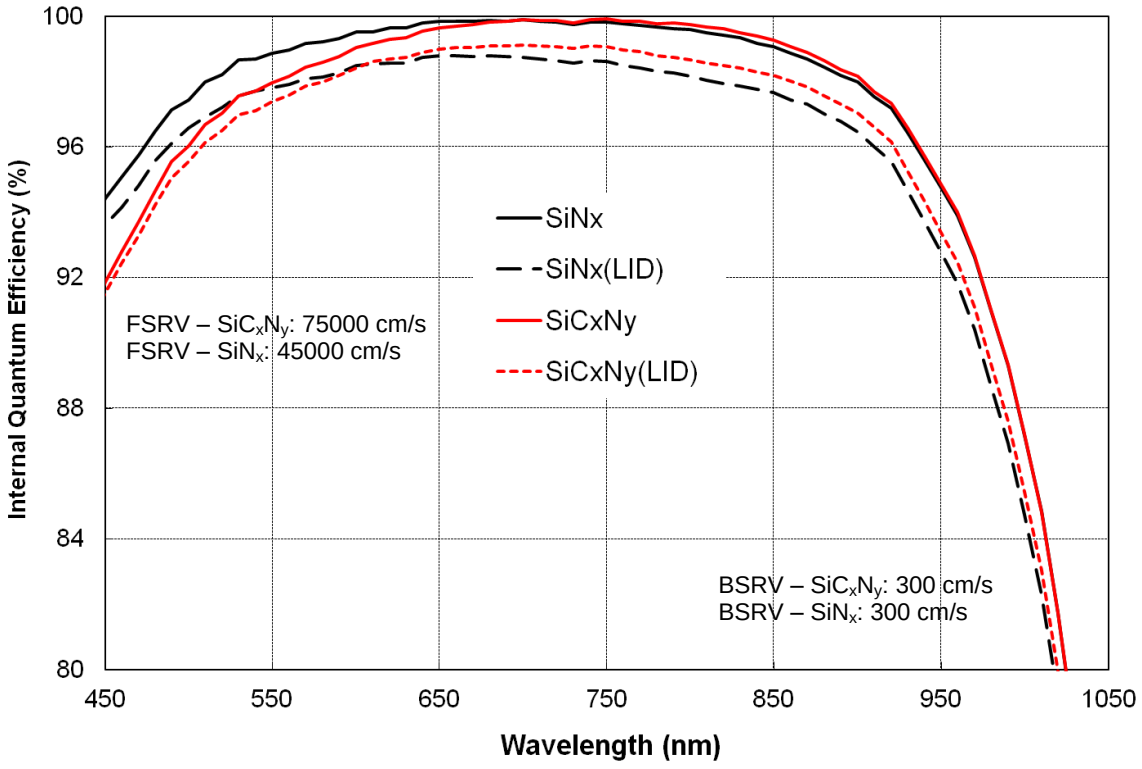

Figure 4.6: IQE of SiN_x- and SiC_xN_y-coated solar cell before and after LID.

Figure 4.7 shows that the LID reduced the bulk lifetime from 234 to 74 µs in the SiN_x-coated cells which accounts for the observed ~0.3% loss in efficiency from 17.3 to 17.0% according to the PC1D model calculations. In the case of SiC_xN_y-coated cells, bulk lifetime decreased from 250 to 130 µs after LID which amounts for a loss of only 0.1% in efficiency because efficiency becomes insensitive to bulk lifetime above 120 µs for the current cell design as supported by the PC1D model calculations in Figure 4.8. As a result, cell efficiency of ~17.0% is observed in both SiC_xN_y- and SiN_x-coated cells after the LID.

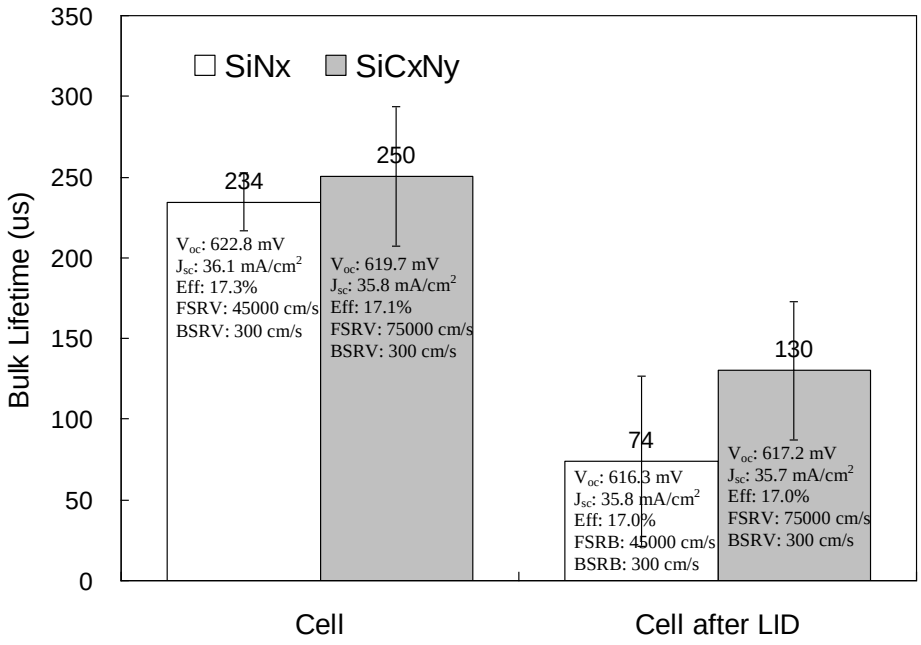

Figure 4.7: Bulk lifetime and corresponding solar cell values from PC1D for SiN_x- and SiC_xN_y-coated solar cell.

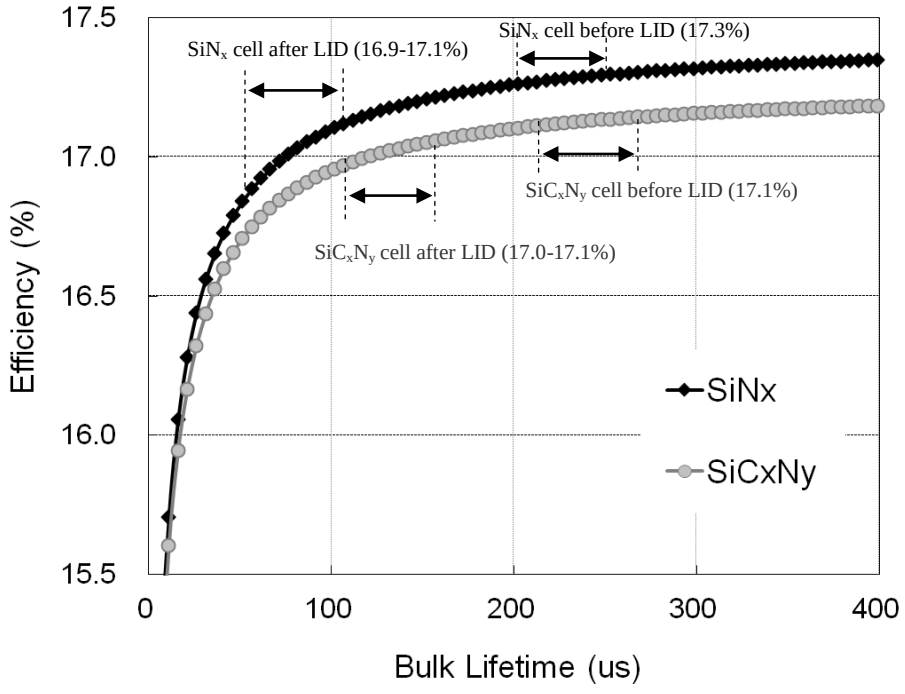

Figure 4.8: Solar cell efficiency as a function of bulk lifetime.

4.4 Conclusion

As shown in this section, the light-induced degradation in boron-doped Cz solar cells also depends on the carbon content of the SiN_x AR coating. Carbon inside the SiC_xN_y AR coating diffuses into Si after the deposition and high temperature contact firing and competes with boron to form complex with oxygen dimmers. This phenomenon reduces the number of $B\text{-}O_{2i}$ metastable defect complexes, which are responsible for bulk lifetime degradation and LID. As a result, SiC_xN_y-coated boron doped Cz solar cells showed appreciably less LID compared to conventional SiN_x-coated solar cells, which have no source of additional carbon. SiN_x-coated solar cells suffered an average loss of 0.3% in absolute efficiency because of LID compared to 0.1% for the SiC_xN_y-coated solar cells. PC1D simulations in Figure 4.7 showed that the observed efficiency loss is entirely consistent with the measured light-induced bulk-lifetime degradation from 234 to 74 μs and 250 to 130 μs in the SiN_x- and SiC_xN_y-coated cells, respectively.

CHAPTER 5

SiC_xN_y-INDUCED RETARDATION OF FILL FACTOR DEGRADATION UNDER LOW LEVEL ILLUMINATION

This chapter investigates the observed improved performance of the cells with silicon-carbon-nitride (SiC_xN_y) antireflection (AR) coating under low illumination. It has been reported [14] that cell efficiency decreases at lower illumination than Standard Test Condition (STC – air mass (AM) 1.5G with intensity of 1000 W/m^2 and 25°C cell temperature) if it has a lower shunt resistance (R_{sh}) [15, 16]. This reduces the annual energy production of the cell and raises the cost of electricity. It was found in this research that SiC_xN_y AR coating from a silane-free source gives higher efficiency at lower illumination compared to the conventional silicon-nitride (SiN_x) film deposited using silane source. Detailed cell analysis and model calculations were performed to demonstrate that this phenomenon is the result of much higher R_{sh} which leads to smaller fill factor (FF) degradation, lower efficiency loss, and higher annual energy production at low illumination. In addition, theoretical calculations are performed to quantify the effect of R_{sh} on FF and efficiency as a function of illumination level. Finally, this information is fed into the System Advisor Model (SAM) from National Renewable Energy Laboratory (NREL) to calculate the impact of R_{sh} on levelized cost of electricity (LCOE) and annual energy production in regions of high and low solar insolation.

5.1 Detailed analysis of the screen-printed Ag/Si contact interface in SiN_x- and SiC_xN_y-coated Si solar cells

Figure 5.1 shows the scanning electron microscope (SEM) picture of screen-printed metal contact interface of SiN_x- and SiC_xN_y-coated cells. It is important to note that screen-printed silver (Ag) contacts are fired through the AR coating, and the firing mechanism can alter the contact interface structure and quality. Generally, the glass inside the paste melts and dissolves Ag particles which etches through the AR coating to form a contact to the silicon (Si) surface. During the high temperature contact firing process, molten glass with silver etches or dissolves a very thin layer of the Si surface, which re-grows epitaxially with silver crystallites embedded into the regrown surface during the cool down [67, 68]. Figure 5.1 shows that SiN_x-coated solar cell had larger silver crystallites at the Ag/Si interface compared to the SiC_xN_y-coated solar cell. Bigger silver crystallites can penetrate much deeper and get closer to ~0.5 μm deep junction edge to form a shunt path because metal inside the Si emitter acts as defect or high recombination site that can increase reverse leakage current [69, 70]. This SEM analysis explains why shunt resistance of the SiC_xN_y-coated solar cells was found to be five to ten times higher than SiN_x-coated solar cells (Figure 5.2).

Larger crystallites in Figure 5.1 were seen in multiple runs with different silver pastes. Figure 5.2 shows that in this study the average shunt resistance of the SiC_xN_y-coated solar cells was 182 Ω compared to 23 Ω for SiN_x-coated solar cells. Therefore, one should be careful in choosing the front silver paste and firing cycle to keep the shunt resistance value above 30 Ω for conventional SiN_x-coated cells. Ag crystallites also assist in tunneling of current through the thin glass layer between Si and Ag grid. This helps in

reducing the value to series resistance (R_{se}). Even though silver crystallites in SiC_xN_y solar cells are much smaller compared to SiN_x-coated solar cells, there are enough of them to give comparable value of R_{se} and FF [70] (Figures 5. 2 (b) and (c)).

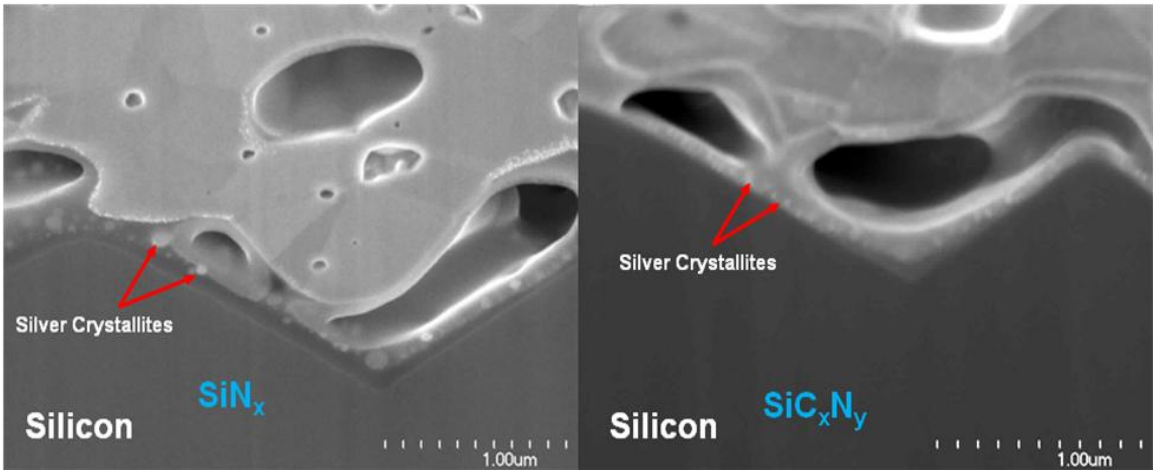

Figure 5.1: SEM picture of screen-printed contact formation through SiN_x- and SiC_xN_y-coated solar cell. SiC_xN_y coating has smaller Ag crystallites.

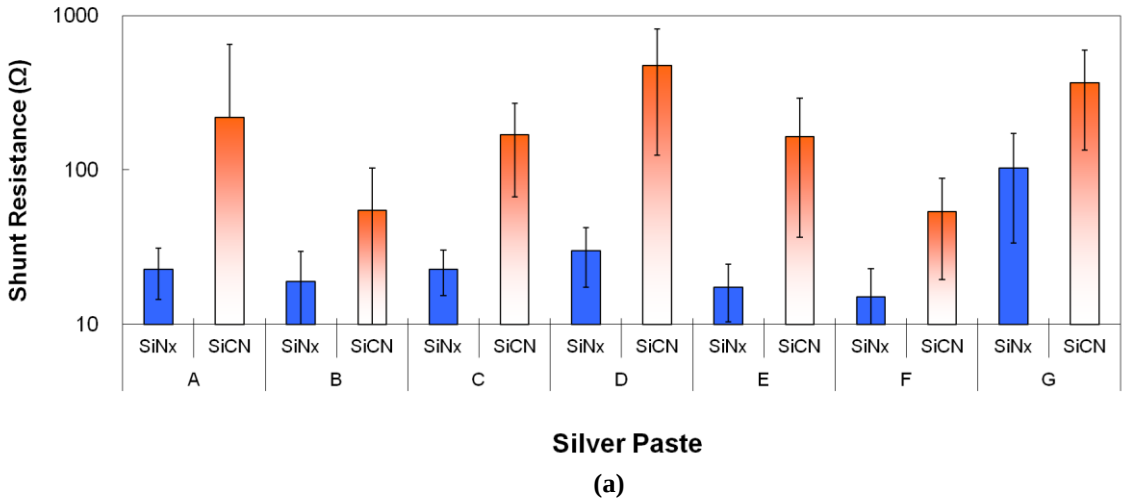

(a)

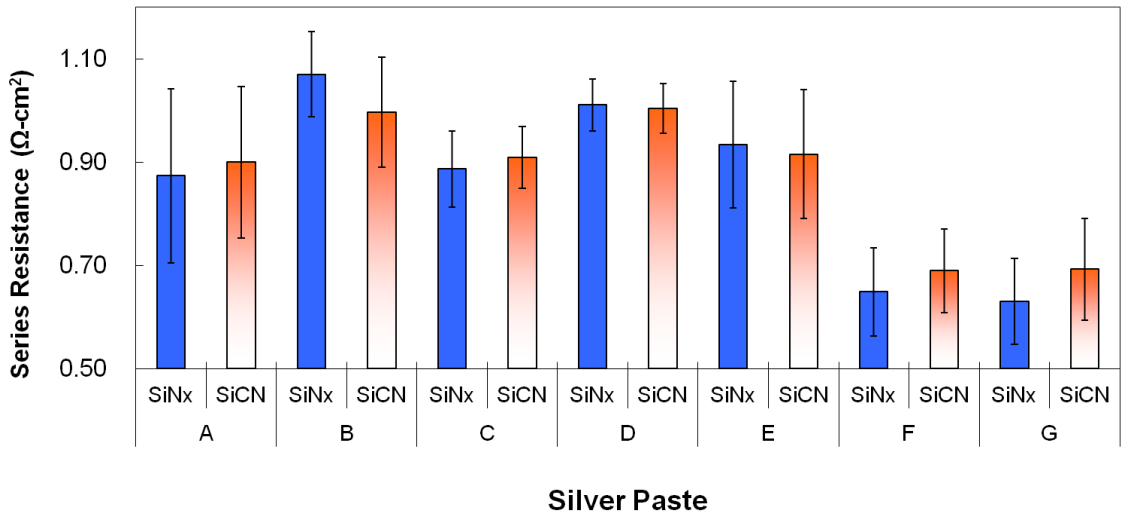

(b)

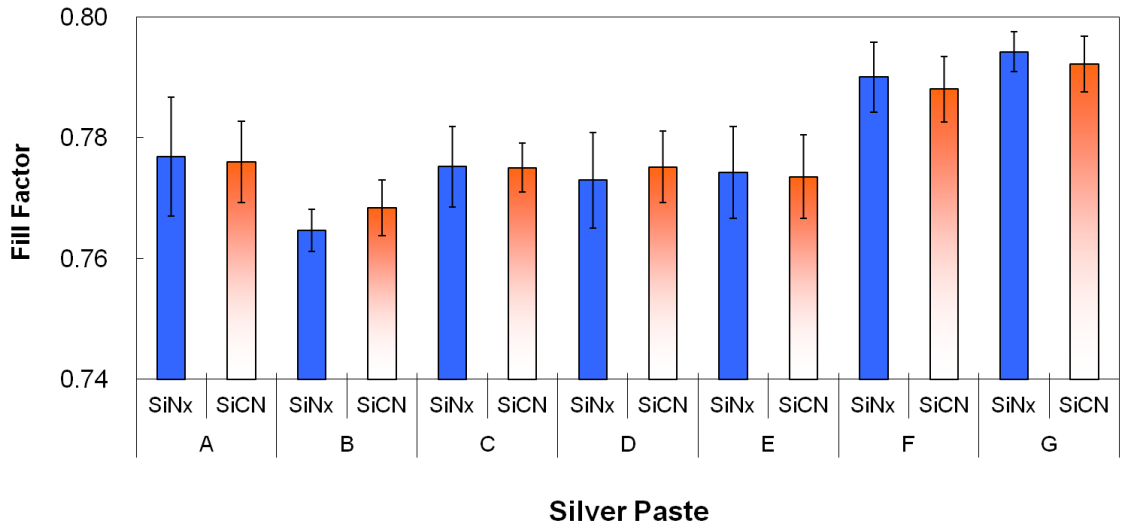

(c)

Figure 5.2: Average values of (a) shunt resistance, (b) series resistance, and (c) fill factor from several hundred SiN_x- and SiC_xN_y-coated solar cells fabricated with different silver pastes.

Figure 5.3 shows the full area shunt scan of a typical SiN_x- and a SiC_xN_y-coated solar cell using CoRRescan. Shunt scan is a destructive technique which measures a potential gradient in the direction of a shunt location and gives a spatial map of R_{sh} over the entire cell [71]. A lower potential gradient indicates less shunting. Average potential gradient was 3.2 mV for the SiN_x-coated solar cell (R_{sh} = 16 Ω) compared to 2.6 mV for the

SiC_xN_y-coated solar cell (R_{sh} = 204 Ω). SiN_x-coated solar cells showed more hot spots (peak in 3D plot) which are believed to be caused by large silver crystallites. Therefore, shunt scan supports better shunt characteristics of SiC_xN_y-coated cell even though there was no appreciable difference in the cell performance under one Sun or the STC conditions. However, the next section shows that is not the case at lower illumination (<< 1000 W/m^2).

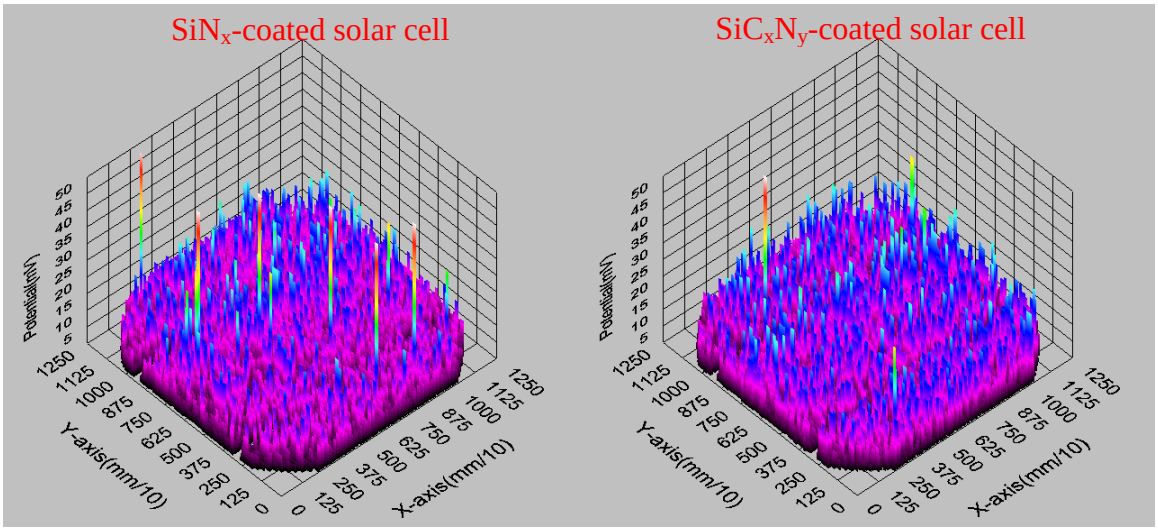

Figure 5.3: Shunt scan of SiN_x- vs. SiC_xN_y-coated solar cells using CoRRescan. SiN_x-coated cells show lower shunt or higher potential gradient and more local hot spots.

5.2 Theoretical calculations to quantify the impact of R_{sh} on FF and solar cell efficiency at lower illuminations

Figure 5.4 shows that calculated values of FF and efficiency as a function of R_{sh} and illumination level. These theoretical calculations were done by using well known equations (5.1) to (5.6) [11] in conjunction with the measured values of open circuit voltage (V_{oc}), short circuit current (I_{sc}), R_{se}, and R_{sh} at STC. Solar cell efficiency degrades

under lower than STC illumination (AM 1.5G of 1000 W/m^2) [14-16] mainly because of the V_{oc} and FF degradation for lower R_{sh} values, as explained below.

I_{sc} decreases linearly with photon flux (N_{ph})

$$I_{sc} \propto q \cdot N_{ph} \cdot IQE \tag{5.1}$$

, and V_{oc} decreases logarithmically with I_{sc}

$$V_{oc} = \frac{kT}{q} \ln\left(\frac{I_{sc}}{I_o} + 1\right) \tag{5.2}$$

Idealized FF_o decreases according to the following equation

$$FF_o = \frac{\upsilon_{oc} - \ln(\upsilon_{oc} + 0.72)}{\upsilon_{oc} + 1},\ \upsilon_{oc} = \frac{V_{oc}}{kT/q} \tag{5.3}$$

Therefore, the R_{CH} (V_{oc}/I_{sc}) value increases, and the normalized r_s and r_{SH} values decrease according to the following equations

$$R_{CH} = \frac{V_{oc}}{I_{sc}},\ r_s = \frac{R_{se}}{R_{CH}},\ r_{SH} = \frac{R_{sh}}{R_{CH}} \tag{5.4}$$

These changes lower the final *FF* (2.30) [11] especially for devices with R_{sh} below 30 Ω.

$$FF_s = FF_o(1 - r_s) \tag{5.5}$$

$$FF = FF_s\left[1 - \frac{(\upsilon_{oc} + 0.7)FF_s}{\upsilon_{oc} \cdot r_{SH}}\right] \tag{5.6}$$

Theoretical calculations revealed that FF drops more rapidly at lower illuminations for cells with smaller values of R_{sh} (Figure 5.4). These calculations also reveal that R_{sh} should be > 8 Ω to reduce the initial sensitivity of efficiency at STC, and R_{sh} should be > 30 Ω to prevent any significant drop at much lower illumination. Above 30 Ω degradation is not appreciable, even though higher value is always desirable.

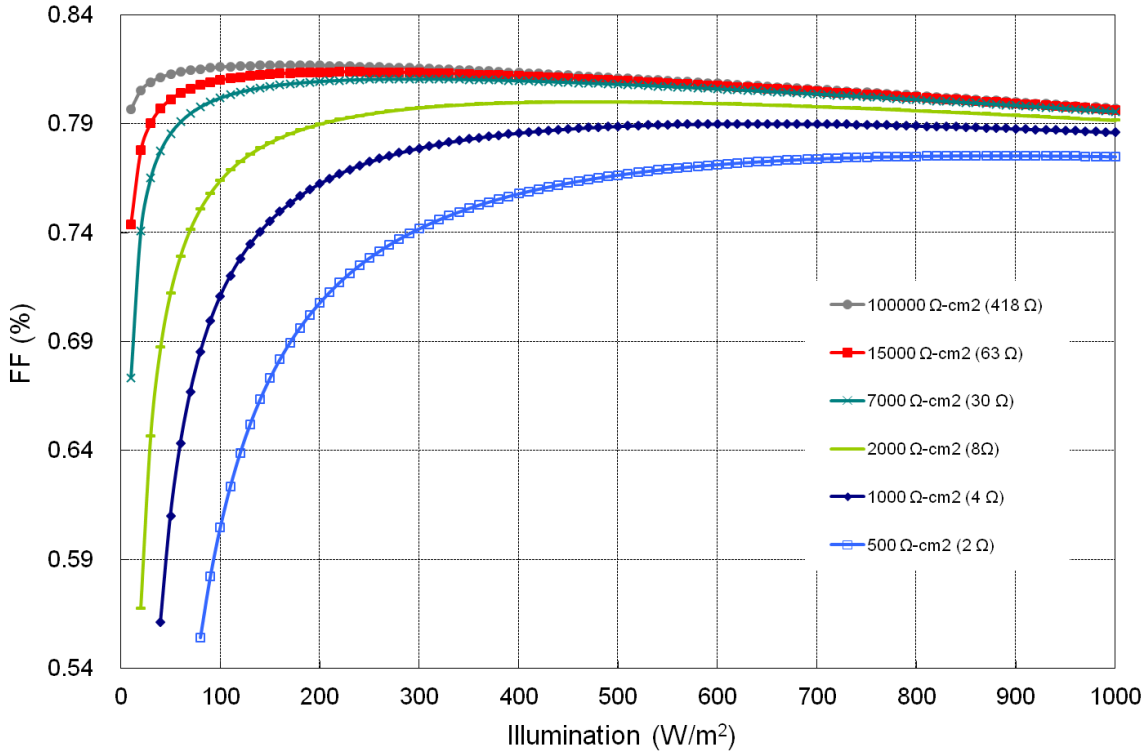

(a)

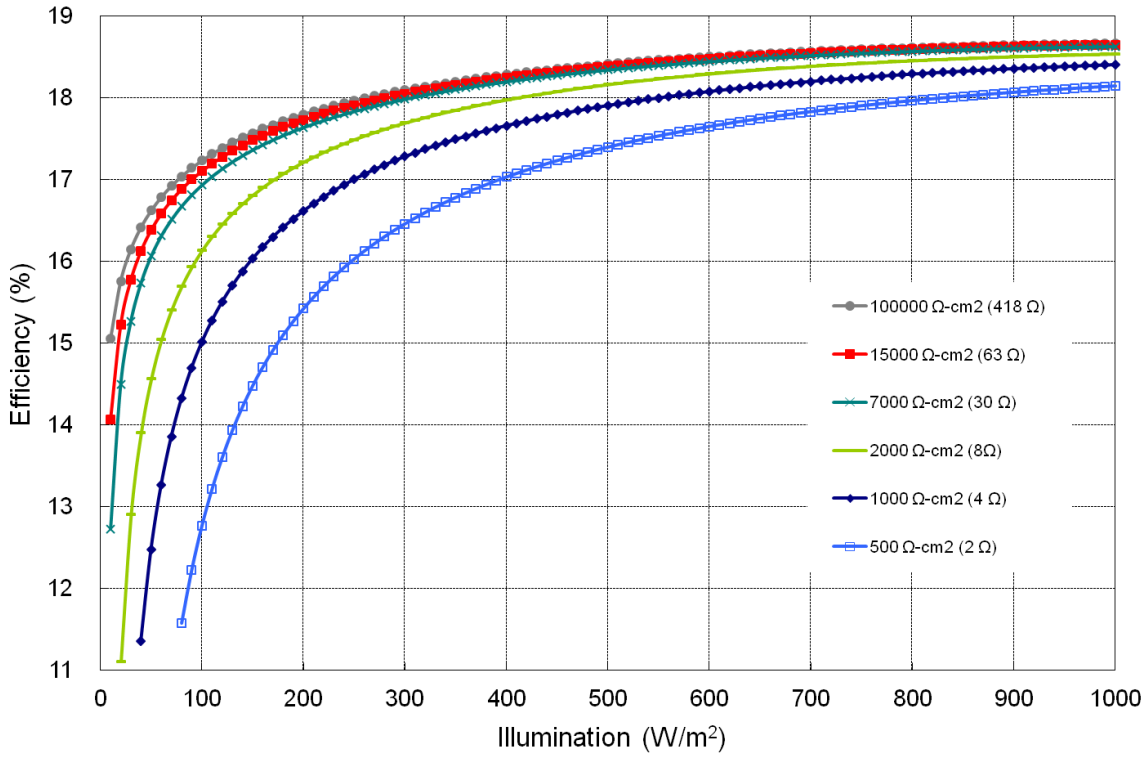

(b)

Figure 5.4: (a) Calculated FF and (b) solar cell efficiency (area = 239 cm^2, V_{oc} = 630 mV, I_{sc} = 8.84 A, and R_{se} = 0.0031 Ω at STC) as a function of illumination intensity with various shunt resistance.

Notice that shunt resistance of SiN_x-coated cells was in the range of ~10–100 Ω (average = 23 Ω) depending on the Ag paste, with many cells below the 30 Ω. Therefore, one needs to be careful in choosing front silver paste and firing to keep the shunt resistance value above 30 Ω for the conventional SiN_x-coated cells. In the case of the SiC_xN_y-coated cells, shunt resistance for most silver pastes was found to be more than 60 Ω with an average of 182 Ω.

5.3 Solar cell efficiency measurements at lower than STC illumination

In order to validate the model calculations in Figure 5.4, efficiency of SiN_x- and SiC_xN_y-coated solar cells was measured (Figure 5.5) with known values of R_{sh}, at various illuminations. Experimental data agreed fairly well with the model calculations.

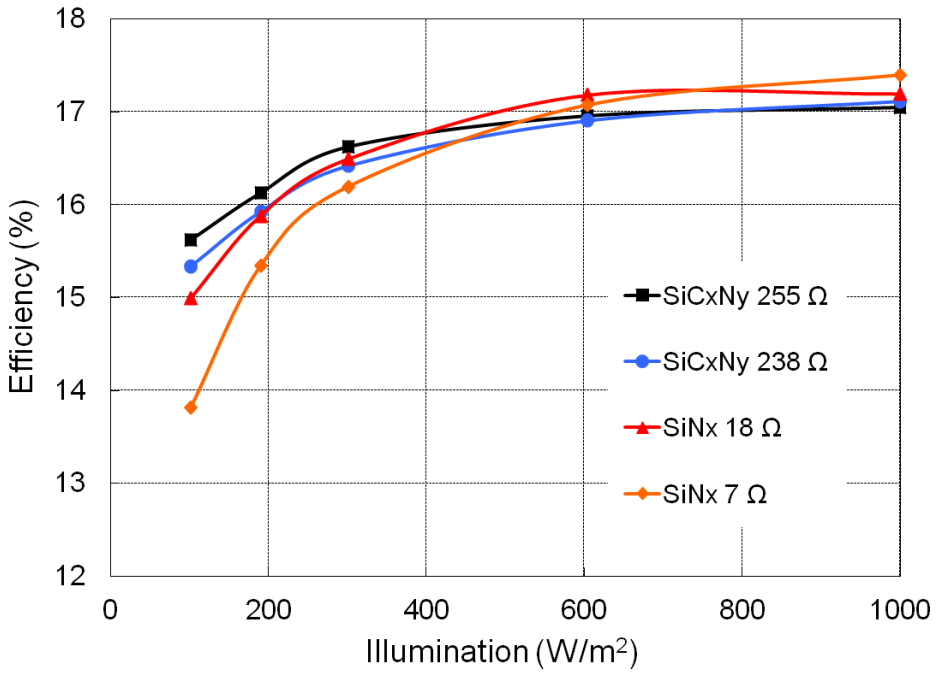

Figure 5.5: Measured solar cell efficiency as a function of illumination intensity of SiN_x- and SiC_xN_y-coated solar cells.

Although starting efficiency of SiC_xN_y-coated cells is slightly lower (~0.2%) because of a inferior emitter surface passivation [66], high R_{sh} or lower efficiency drop at lower illuminations makes up for the slightly lower starting efficiency of the SiC_xN_y-coated cells. SiC_xN_y cell efficiency became equal to or greater than the SiN_x-coated cells at or below 600 W/m^2 illuminations. This affects the LCOE and total annual energy production for the two types of devices, as shown in the next section.

5.4 Impact of shunt resistance on annual energy production and LCOE at different solar insolation

SAM version of 2011.12.2 program from NREL was used to quantify the effect of R_{sh} on LCOE and annual energy production for locations with various solar insolation (high, medium, and low). This tool has the capability to account for the impact of change in efficiency as a function of solar insolation. Calculated efficiency vs. insolation data for different R_{sh} values (Table 5.1) were fed into the SAM program to account for the impact of R_{sh}. Other key inputs for SAM are listed in Table 5.2.

Table 5.1: Solar cell efficiencies (area = 239 cm^2, V_{oc} = 625 mV, I_{sc} = 8.70 A, and R_{se} = 0.0031 Ω at STC) as a function of shunt resistance and solar insolation used for SAM calculations.

Illumination (W/m^2)	4 Ω	8 Ω	13 Ω	21 Ω	30 Ω	105 Ω	209 Ω	418 Ω
200	14.17	14.75	14.95	15.10	15.17	15.29	15.31	15.32
400	15.18	15.49	15.59	15.67	15.70	15.77	15.78	15.79
600	15.57	15.78	15.85	15.91	15.93	15.98	15.98	15.99
800	15.77	15.93	15.98	16.02	16.04	16.07	16.08	16.08
1000	15.87	16.00	16.04	16.07	16.09	16.11	16.12	16.12

Table 5.2: Specified parameters used for SAM calculations.

System parameter	Value
Market	Commercial
Module efficiency at STC (%)	16
System size (kW)	100
PV module cost ($/W)	1
Inverter cost ($/W)	0.3
Area related BOS cost ($/W)	0.8
Indirect or fixed BOS cost ($/W)	1.2
Installed system cost ($/W)	3.3
Annual system degradation (%/yr)	1
System derate losses (%)	20
Annual O&M ($/kW/yr)	16.5
Weight average cost of capital (WACC) (%)	7.5

SAM's output includes LCOE and annual energy production. Four different locations, Phoenix, LA, Atlanta, and Seattle, were selected for comparison because they have appreciably different solar insolation (global horizontal) ranging from 2117 to 1222 $kWh/m^2/yr$. Figure 5.6 shows the difference in calculated LCOE and annual energy production as a function of location and R_{sh} value. It is found that for any given location, if the R_{sh} is above 30 Ω, then R_{sh} has very little effect on LCOE. However if R_{sh} is below 15 Ω, it could reduce the energy production and raise the LCOE. In addition, the impact of R_{sh} below 15 Ω is increased for regions of lower solar insolation like Seattle. Because SiC_xN_y-coated solar cells show high shunt resistance (> 30 Ω) compared to SiN_x-coated cells, the slightly lower initial efficiency (~0.2%) of the SiC_xN_y-coated cells at STC is compensated by higher R_{sh} with regards to annual energy production which will be shown in section 5.5.

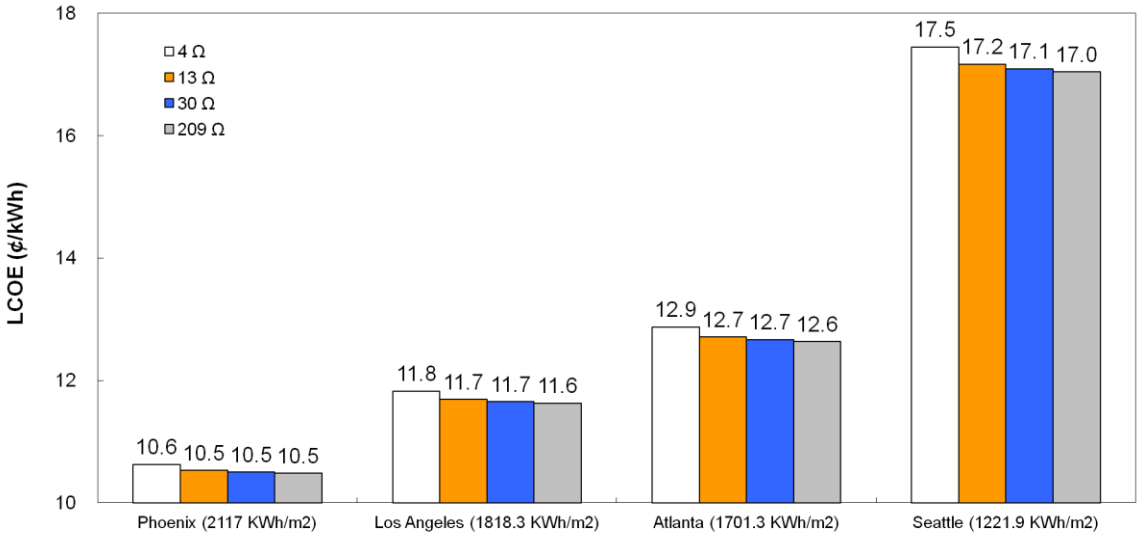

(a)

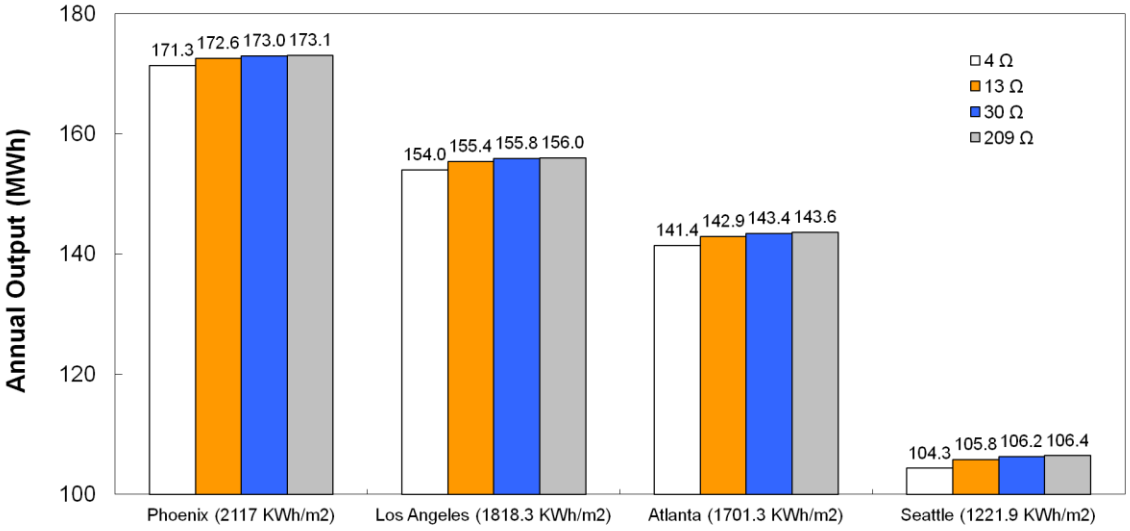

(b)

Figure 5.6: Calculated values of (a) LCOE and (b) annual energy output as a function of shunt resistance for four regions of varying solar insolation.

Figure 5.7 shows the annual energy output loss per 1 kW (kWh/kW) as a function of shunt resistance in the range of 4–418 Ω for Seattle and Phoenix locations. Note that Seattle shows higher loss compared to Phoenix for a given value of R_{sh}. In addition, for R_{sh} above 30 Ω, there is very little energy loss, and the loss increases monotonically as the R_{sh} value goes below 30 Ω. Figure 5.7 shows that for R_{sh} value of 4 Ω, energy loss is

21.4 kWh/kW in Seattle. This means a 1 MW system with R_{sh} = 4 Ω will produce 21400 kWh less energy compared to a module with R_{sh} = 418 Ω. At a 10¢/kWh price of electricity in Seattle, this amounts to a loss of $2140/yr.

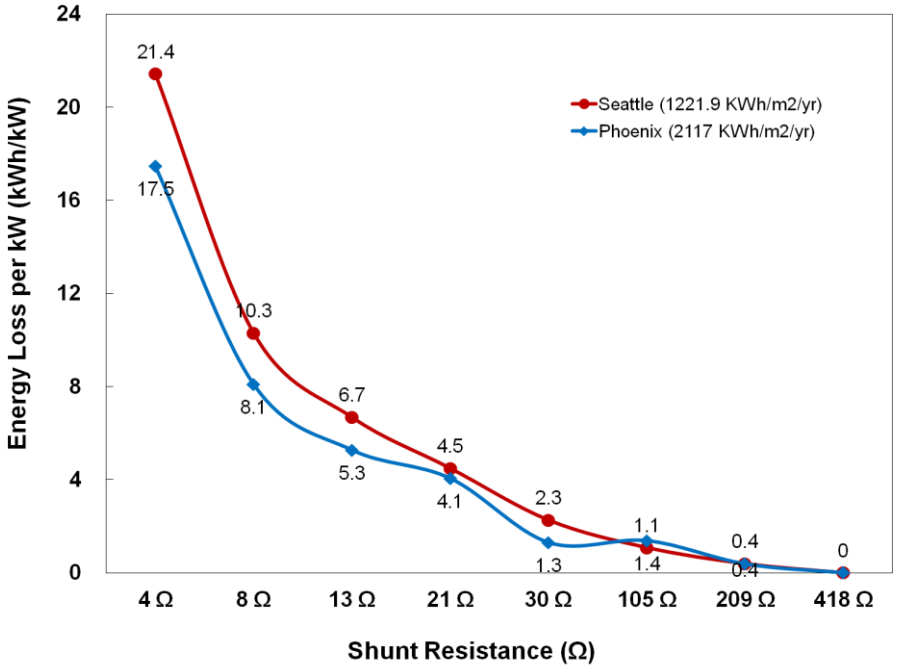

Figure 5.7: Annual output power loss per 1 kW module as a function of shunt resistance.

5.5 LCOE and annual energy production for the two AR coatings

After establishing the methodology to compute efficiency and financial loss associated with R_{sh}, we applied it to compare SiN_x and SiC_xN_y coatings. LCOE and annual energy production for the two AR coatings were calculated using SAM. R_{sh} value of each AR coating was chosen from the experimental average of hundreds cells: 23 Ω for SiN_x and 180 Ω for SiC_xN_y. Module efficiency of 16.0% and 15.8% were used for SiN_x- and SiC_xN_y-coated cells, respectively to account for the slightly lower cell efficiency (18.2% as opposed to 18.4%) of SiC_xN_y-coated cells at STC. Annual energy production and

LCOE calculations were performed for four locations: Phoenix, LA, Atlanta, Seattle. Figure 5.8 (b) shows that if R_{sh} was 23 Ω for both AR coatings (first and second bars), then the SiC_xN_y module would produce 373 kWh less energy in Phoenix. However since R_{sh} is 180 Ω (third bar) for SiC_xN_y instead of 23 Ω, it is able to make up for 264 kWh loss because it performs better at lower illumination.

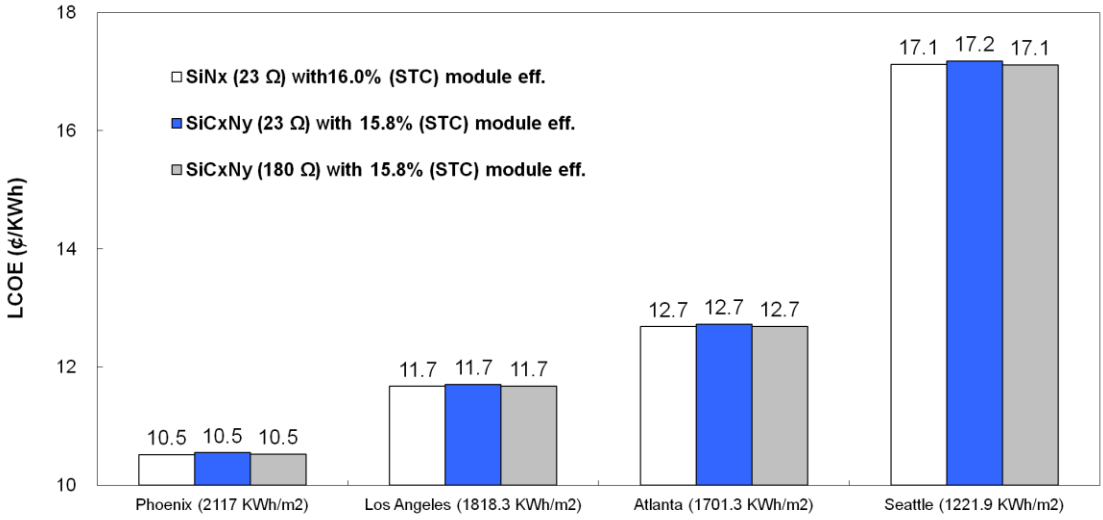

(a)

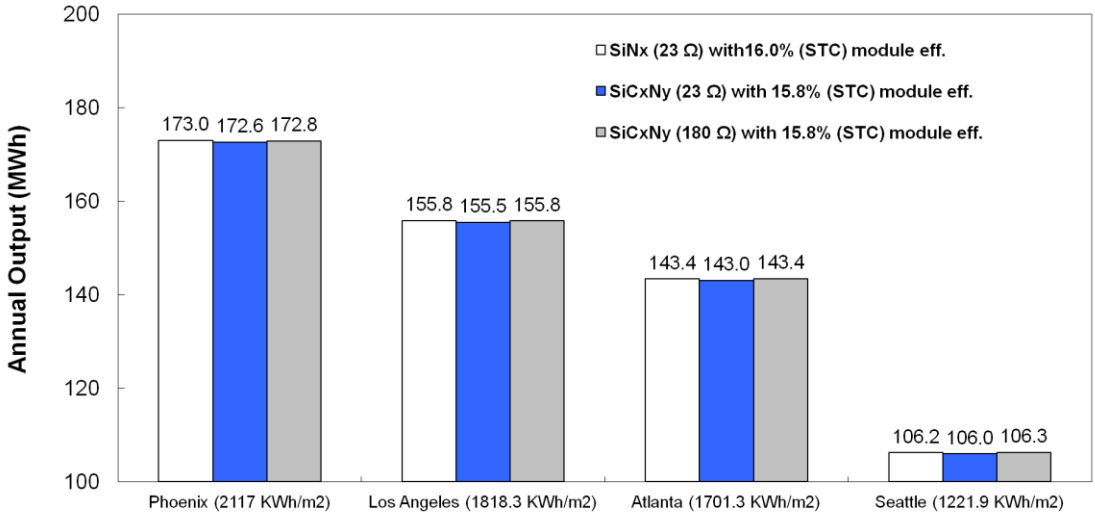

(b)

Figure 5.8: Calculated values of (a) LCOE and (b) annual energy output of SiN_x and SiC_xN_y AR-coated modules for four regions of varying solar insolation.

Note that in Seattle, SiC_xN_y module produces higher energy in spite of its lower starting efficiency than SiN_x module at STC. This is because module stands mostly below STC illumination in Seattle, so performance at low illumination is more important. SAM calculations indicate that higher value of R_{sh} in SiC_xN_y-coated cells can compensate the initial efficiency gap except in high insolation region (Phoenix). Note that there is no appreciable LCOE difference between SiN_x- and SiC_xN_y-coated cells regardless of efficiency and R_{sh} difference.

5.6 Conclusion

It is found that carbon-containing SiC_xN_y film show much higher R_{sh} value after contact firing compared to carbon-free SiN_x film. SEM measurements showed that the size of silver crystallites at the contact interface is smaller in the presence of carbon in the SiC_xN_y AR coatings which reduces the parasitic shunting in the cell (high R_{sh} value). An analytical model was developed and used to calculate the loss in cell efficiency at lower illuminations due to lower R_{sh}. It was found that R_{sh} should be above 30 Ω to avoid appreciable efficiency loss under low illumination. Model calculations were validated with the experimental data which confirmed that lower R_{sh} values reduce the cell efficiency at lower insolation even if the starting cell efficiency is same. A methodology was developed to combine the efficiency vs. illumination calculation with the LCOE and financial calculations to quantify the impact of R_{sh}-induced efficiency loss or LCOE and annual expense. It has shown that a 1 MW system will produce 19100 kWh less energy if the R_{sh} value drops from 30 to 4 Ω which could amount to be $1910/yr for 10¢/kWh price of electricity. This methodology was applied to compare SiC_xN_y and SiN_x films. It was

shown that even though the starting efficiency of SiC_xN_y-coated cells was 0.2% lower than SiN_x-coated cells, the annual energy production and LCOE was very similar because SiC_xN_y-coated cells had much higher R_{sh} (180 Ω) compared to SiN_x-coated cells (23 Ω).

CHAPTER 6

MODELING AND OPTIMIZATION OF INDEX AND THICKNESS OF SiN_x ANTIREFLECTION COATING FOR THE BEST PERFORMANCE OF SILICON SOLAR CELLS PLACED IN MODULES

It is important to note that optimum refractive index (n) and thickness of antireflection (AR) coating could be different for silicon (Si) solar cells tested in air and under glass. This is because air has a n = 1 while glass has a n = 1.5. Generally a higher index film is preferred under glass, but higher index silicon-nitride (SiN_x) films show considerable absorption. Degree of absorption can shift the optimum index under glass. This section takes into account index, thickness, reflection, and absorption to design the SiN_x based AR coating which can provide best performance under a glass module. For more accurate assessment of reflection and absorption losses as a function of Si surface morphology and bulk and interface properties of the films, a Monte-Carlo simulation program "Sunrays" [72] was used. Each ray of light is traced according to the law of geometrical optics which enables accurate characterization of specific surface morphology, cell structure, and multi layers of various dimensions. The program is capable of quantifying reflection, refraction, and absorption at every interface and in the bulk material [73]. First, bulk properties of various SiN_x films were investigated with refractive index in the range of 2.03–2.42. Simulations are performed on planar as well as standard pyramid textured surfaces. Performance is evaluated in air and under an encapsulated glass module. All the optical losses (reflectance and absorbance) obtained from Sunrays simulations are

translated into a reflectance file that can be used in PC1D device simulation program to calculate the expected solar cell efficiency and efficiency loss under a glass module. Final cell efficiency inside the module is used to optimize the choice of SiN_x coating because module efficiency dictates the energy output and levelized cost of electricity (LCOE).

6.1 Optical simulation conditions and inputs

Refractive index (n) (Figure 6.1) and extinction coefficient (k) (Figure 6.2) of various SiN_x films were obtained from literature [30] and transferred to the library files in the Sunrays simulation program. Refractive index is a function of wavelength (dispersion), but for identifying purpose its value at the wavelength of 630 nm will be used in this section to specify the coating because solar spectrum peaks at 630 nm. However, refractive index values at all wavelengths of interests (300–1200 nm) were used in the Sunrays simulations. Figures 6.1 and 6.2 show that within the wavelength range of interest (300–1200 nm), both refractive index and extinction coefficient decrease as the wavelength increases. Notice that high index SiN_x films also have high extinction coefficient values. Therefore, higher index films are expected to have more parasitic absorption. Also note that extinction coefficient value is high at shorter wavelengths and approaches zero when the photon energy falls below the bandgap energy (E_g) of the SiN_x film. Higher index SiN_x films have lower bandgap energy, so they have a cut off at higher wavelength which also increases the absorption.

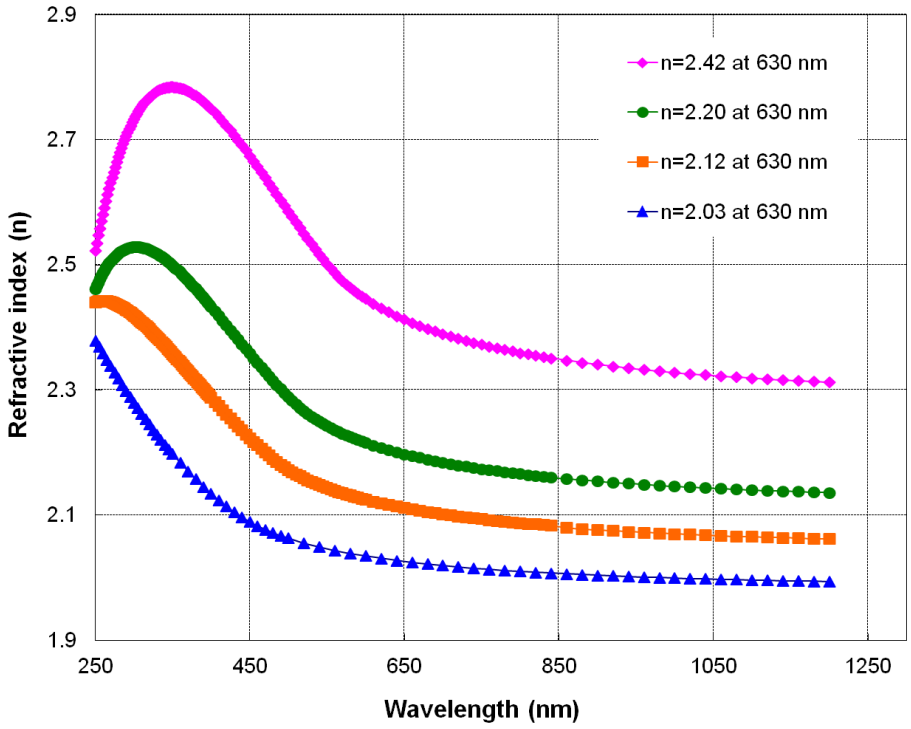

Figure 6.1: Refractive index (n) of various index SiN_x films.

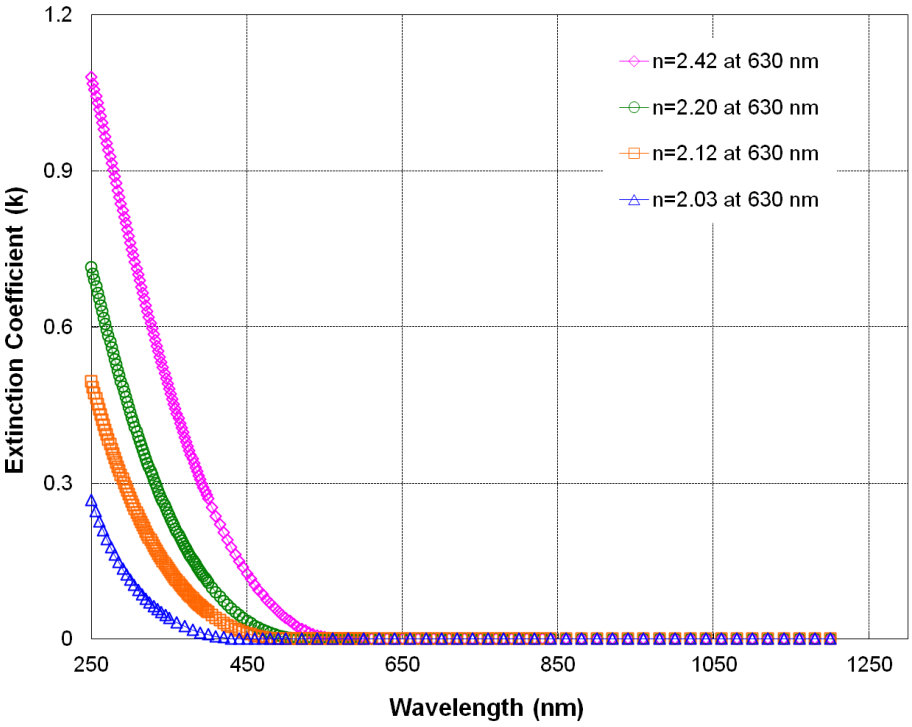

Figure 6.2: Extinction coefficient (k) of various index SiN_x films.

Specific cell and optical parameters used for simulations are listed in the Table 6.1. A typical screen-printed cell with full aluminum-back-surface field (Al-BSF) structure was used in the device simulation. Lambertian aluminum was adopted for back reflector. SiN_x films with refractive index of 2.03, 2.12, 2.20, and 2.42 were used for investigation of AR coatings. A combination of B270 glass (n = 1.5) and ethylene vinyl acetate (EVA; n=1.5) was selected for module encapsulation. Air mass (AM) 1.5G (1000 W/m^2) solar spectrum with normal incidence was applied for illumination of the light. Note that refractive index of each material is defined at 630 nm wavelength for identifying purpose, but for simulations, correct index values for all wavelengths were used.

Table 6.1: Sunrays simulation parameters for determining optical loss in air and under a glass module.

		Air	Glass
Texturing	Structure	Upright pyramid	Upright pyramid
	Width	5 μm	5 μm
	Depth	3.535 μm	3.535 μm
Material	Front	Air (n = 1)	Air (n = 1)
	Encapsulant	Air (n = 1)	EVA (n = 1.5)
	Texture	Silicon (n = 3.8)	Silicon (n = 3.8)
	Substrate	Silicon (n = 3.8)	Silicon (n = 3.8)
	Back	Aluminum	Aluminum
AR Coating	Front/Encapsulant	Air	Top: B270 (3 mm) Bottom: EVA (0.5 mm)
	Encapsulant/Texture	SiN_x (n = 2.03–2.42)	SiN_x (n = 2.03–2.42)
	Back surface reflector	Aluminum	Aluminum
Illumination		Normal	Normal
Spectrum		AM1.5G (1000 W/m^2)	AM1.5G (1000 W/m^2)
	Polarization	Unpolarized	Unpolarized

The sum of reflectance and absorbance losses at each wavelength from Sunrays was transferred to PC1D model as *.ref file to calculate the final solar cell efficiency. Wavelengths used for the calculation ranged from 300 to 1200 nm. Baseline screen-printed Al-BSF solar cell parameters used for PC1D modeling are listed in Table 6.2.

Table 6.2: List of solar cell parameters used in PC1D to quantify the impact of optical loss on cell efficiency.

Cell thickness	200 μm
Base resistivity	2.2 Ω-cm^2
Bulk lifetime	200 μs
Emitter	63 Ω/sq (Gaussian)
Texturing depth	3.535 μm
FSRV	40000 cm/s
BSRV	300 cm/s
BSR	70%
J_{o2}	10 nA/cm^2
Rseries	0.8 Ω-cm^2
Rshunt	5263 Ω-cm^2
Grid shading	6.5%

6.2 Optical properties of SiN_x films and corresponding cell efficiency in air (n = 1.0)

6.2.1 Analysis of SiN_x-coated planar surfaces and corresponding cells tested in air

Figure 6.3(a) shows the total optical loss (reflectance + absorbance) calculated form Sunrays model and Figure 6.3(b) shows the corresponding solar cell efficiency calculated from PC1D device model for various SiN_x films as a function of SiN_x thickness. According to Figure 6.3(a), the optimum thickness of a SiN_x film on a planar surface is inversely proportional to its refractive index. As expected, n = 2.03 showed the smallest optical loss (reflectance + absorbance) because of the combination of better index match with air and smallest parasitic absorption [30]. Greater optical loss for the higher index films is due to higher index mis-match with respect to air as well as higher absorption. For example, Figure 6.3(a) shows that a SiN_x film with n = 2.42 loses 6% more photons (16.4% vs. 10.4%) compared to n = 2.03 because of reflection + absorption, which amounts to over 1% absolute efficiency loss from 16.6% to 15.3% as shown in Figure 6.3(b). Thus, for planar cells in air, best AR coating has an index of 2.03 and a thickness of ~76 nm.

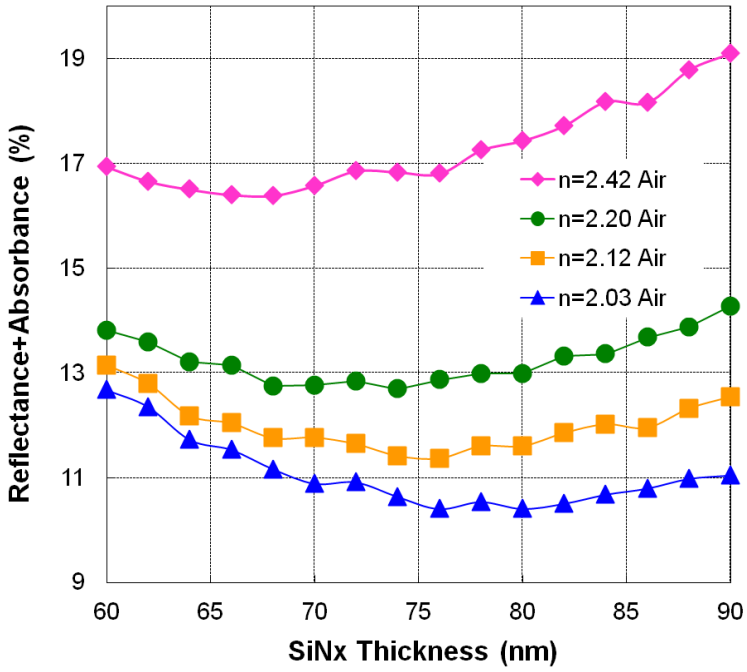

(a)

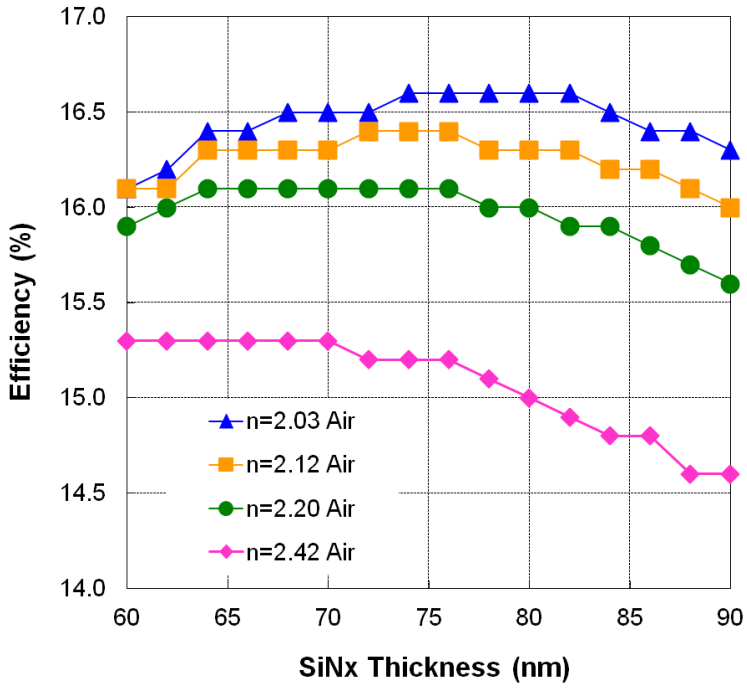

(b)

Figure 6.3: (a) Total optical loss (reflectance + absorbance) associated with index of SiN_x films as a function of SiN_x thickness on planar surface in air ambient and (b) corresponding solar cell efficiency from PC1D calculations.

6.2.2 Analysis of SiN_x-coated textured surfaces and corresponding cells tested in air

Figures 6.4(a) and (b) show total optical loss (reflectance + absorbance) and corresponding solar cell efficiency for textured cells tested in air ambient. General trends are similar to the planar surface calculations in the previous section except the efficiency is not as strong a function of thickness compared to the planar surface. For example, on a textured surface, thickness can vary from 64–84 nm without appreciable change in efficiency for a SiN_x film with n = 2.03. This window shrinks to 74–82 nm for planar cells (Figure 6.3). This is because reflectance contribution to the total optical loss is much less for textured cells, so the thickness window can be greater because thickness influences the reflectance. Since reducing the thickness decreases absorption, therefore for a high index film, it is desirable to reduce the AR thickness to a point where the absorption gain offsets the reflection loss. Figures 6.3 and 6.4 show that the optimum thicknesses are comparable for planar and textured surfaces for low index SiN_x films (2.03 and 2.12). However, optimum thicknesses on a textured surface is ~8 nm less than the planar surface for high index films (2.20 and 2.42) because of appreciable absorption in these films. This is because contribution of reflection to total optical loss is much greater for a planar surface, so the attempt to reduce total optical loss by reducing the thickness (or absorption) is not as effective. Thus, according to Figure 6.4, the optimum SiN_x AR coating for a textured solar cell in air has an index of 2.03 with thickness of 64–84nm.

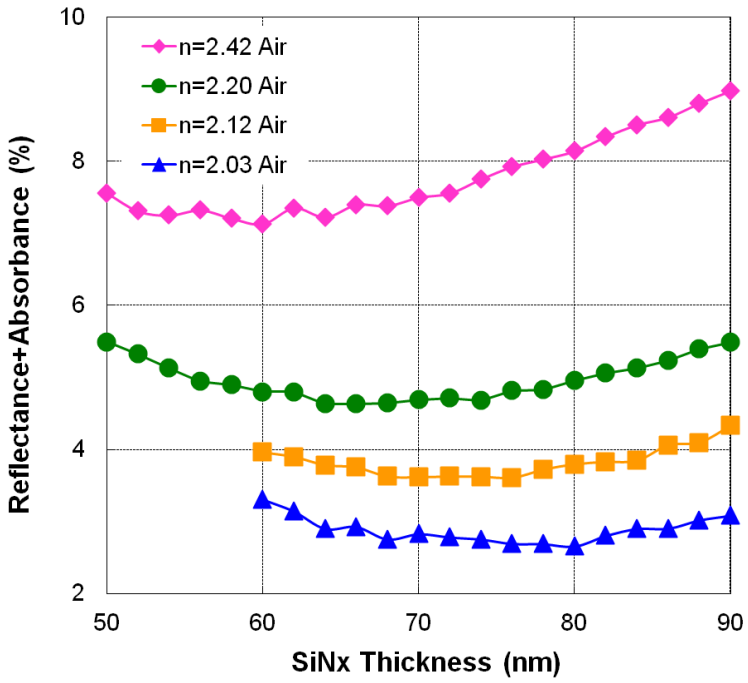

(a)

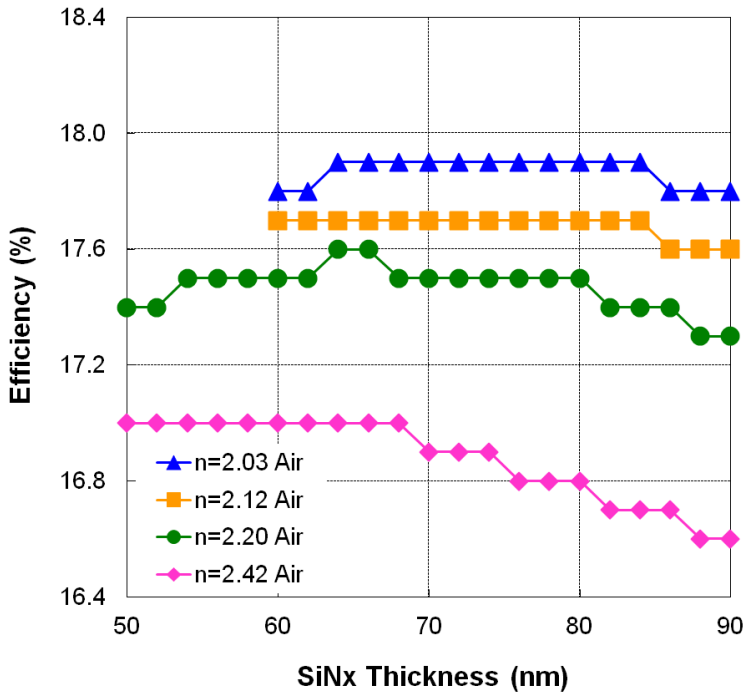

(b)

Figure 6.4: (a) Total optical loss (reflectance + absorbance) associated with index of SiN_x films as a function of SiN_x thickness on textured surface in air ambient and (b) corresponding solar cell efficiency from PC1D calculations.

6.3 Optical properties of SiN_x films and corresponding cell efficiency under glass (n = 1.5)

Finished solar cells are generally encapsulated in a glass module with EVA layer between the glass and solar cells. Therefore, encapsulated cell efficiency loss which comes from change in optical properties under a glass module are more critical than in air. Note that glass and EVA both have an index of 1.5 at 630 nm. Table 6.3 shows a list of all possible optical and electrical losses or gains when solar cells are placed in a glass module [37, 74]. Gray-highlighted values are from our optical simulations, and the others are from the literature. PC1D solar cell efficiency calculations accounted for only the highlighted loss and gain mechanisms in Table 6.3 because zero depth concentrator effect and series resistance losses are beyond the capability of Sunrays optical model and are not associated with the antireflection properties of the AR coating. Glass adds 4% reflection from the top surface regardless of the SiN_x film underneath. However, glass also reduces the reflection from the SiN_x film at the glass/EVA and SiN_x interface because of its higher index (n = 1.5) than air (n = 1). This optical gain is especially large on a planar surface or for a higher index SiN_x film. The absorption in the SiN_x film is reduced under glass because some absorption occurs in glass and EVA in the short wavelength (300–400 nm). Thus, many short wavelength photons are already absorbed in the glass or EVA before reaching the SiN_x film. As a result, absorption within the SiN_x film is reduced by 0.29 to 1.26% depending on the index (Table 6.3). Note that B270 glass and EVA combination used in this study absorbs 2.08 to 2.21% of the light in the short wavelength range for textured and planar devices, respectively. Zero depth concentrator effect gain is associated with the light reflected from the white Tedlar® sheet

between the cells which gets reflected back onto the cell from the glass, causing a concentrator type effect [37, 74].

Table 6.3: Glass module encapsulation loss (negative) and gain (positive) list.

Surface	Textured				Planar			
Refractive index	2.03	2.12	2.2	2.42	2.03	2.12	2.2	2.42
Glass reflection (%)	-4	-4	-4	-4	-4	-4	-4	-4
Glass & EVA absorption (%)	-2.08	-2.08	-2.08	-2.08	-2.21	-2.21	-2.21	-2.21
Gain by SiN_x reflection reduction (%)	+1.64	+1.77	+2.06	+2.81	+3.85	+5.09	+6.26	+8.94
Gain by SiN_x absorption reduction (%)	+0.29	+0.64	+0.9	+1.26	+0.18	+0.4	+0.57	+0.66
Series resistance loss (%)	-4	-4	-4	-4	-4	-4	-4	-4
Zero depth concentrator effect (%)	+1.2	+1.2	+1.2	+1.2	+1.2	+1.2	+1.2	+1.2
Total encapsulation loss (%)	-6.95	-6.47	-5.92	-4.81	-4.98	-3.52	-2.18	0.59

6.3.1 Analysis of SiN_x-coated planar surfaces and corresponding cells tested under glass/EVA

Figures 6.5(a) and (b) show the total optical loss (reflectance + absorbance) and the corresponding solar cell efficiency for various SiN_x films as a function of SiN_x thickness. From the quarter-wavelength equation [11], n = 2.42 should be the best index under glass for smallest reflection. However, in reality, the significant absorption in this film makes total optical loss worse than any other SiN_x film. In contrast, the SiN_x film with n = 2.03 has the highest reflection but lowest absorption loss. It was found that for a planar surface, SiN_x film with n = 2.20 has the lowest optical loss composed of modest reflection and absorption.

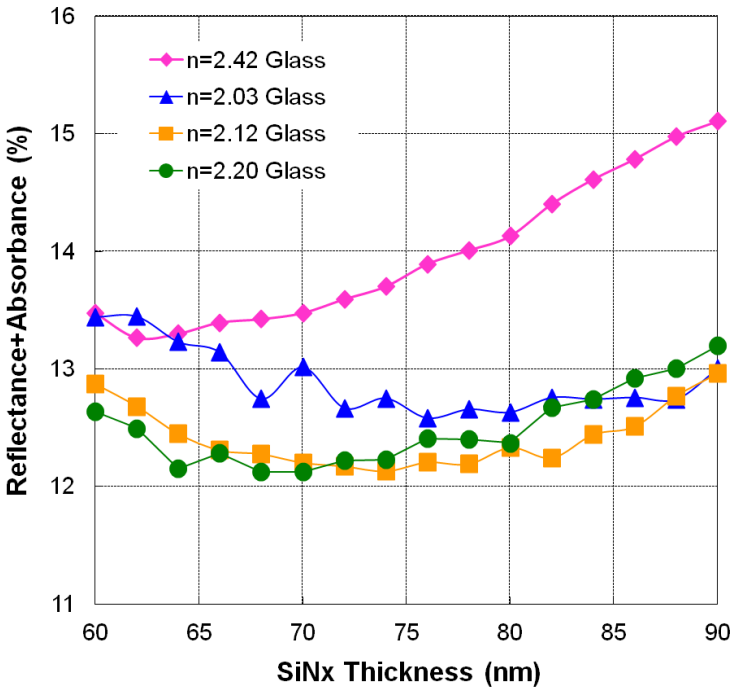

(a)

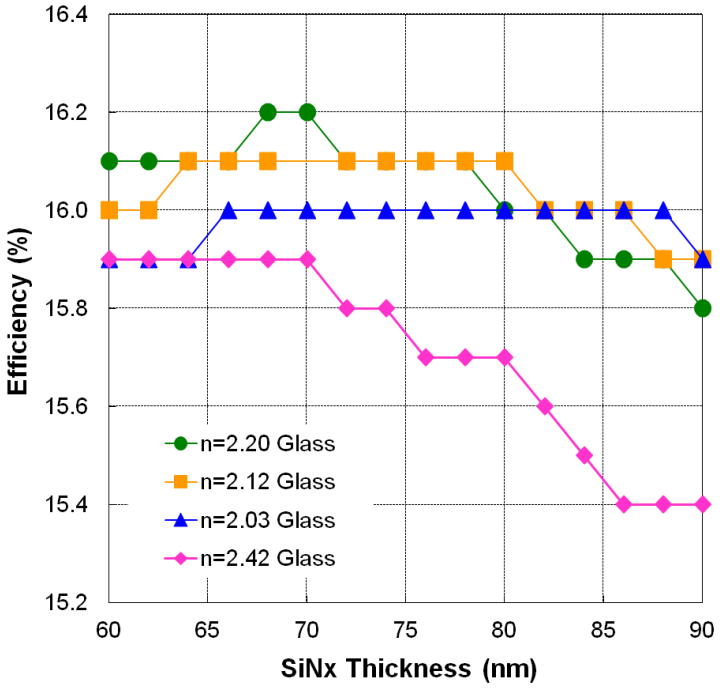

(b)

Figure 6.5: (a) Total optical loss (reflectance + absorbance) associated with index of SiN_x films as a function of SiN_x thickness on planar surface under glass ambient and (b) corresponding solar cell efficiency from PC1D calculations.

6.3.2 Analysis of SiN_x-coated textured surfaces and corresponding cells tested under glass/EVA

This is the most popular and important case because most commercial cells are textured and encapsulated for systems applications. Figures 6.6(a) and (b) show the calculated optical loss and efficiency of textured cells under glass. It was found that the combination of texturing and glass/EVA materials significantly reduce the reflection from the SiN_x film. Therefore, reflection is no longer a dominant factor in the total optical loss, instead absorption becomes more important. That is why the smallest optical loss is seen in the film with the smallest parasitic absorption which happens to be low index. As a result, contrary to conventional thinking from the viewpoint of index matching, index of 2.03 is the best for textured cells under glass. Even though, n = 2.42 film is better index matched with glass according to quarter-wavelength equation, its cell efficiency under glass is lower by 0.6% absolute compared to SiN_x film with n = 2.03 (17.1% vs. 16.5%) because the starting cell efficiency in air is 0.9% higher (17.9% vs. 17.0%) for the n = 2.03 film compared to n = 2.42 film (Figure 6.4). Thus, even though the 2.42 film is better index matched, index 2.03 film produces higher cell efficiency inside a module. This is also reflected in Table 6.3, which shows that total encapsulation loss (air to glass) for 2.42 index film is 4.81% compared to 6.95% for n = 2.03 film. However, Figure 6.6 shows that the encapsulated cell efficiency (17.1%) for n = 2.03 film is greater than the efficiency (16.5%) for n = 2.42 film because of higher starting cell efficiency (17.9% vs. 17.0%) for the n = 2.03 film in the air.

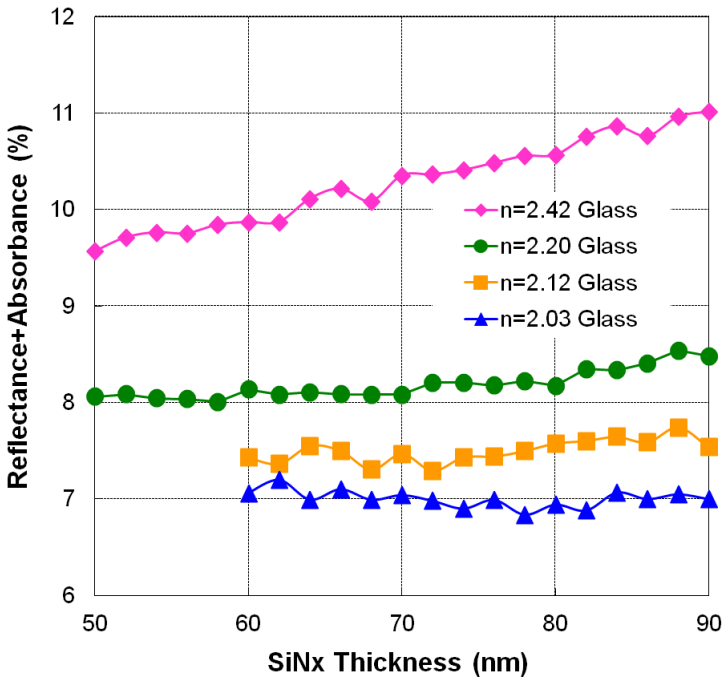

(a)

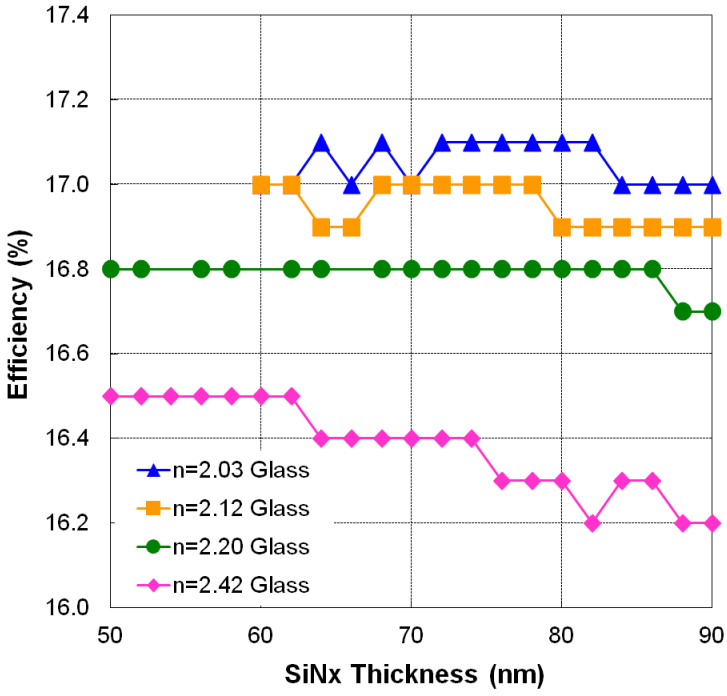

(b)

Figure 6.6: (a) Total optical loss (reflectance + absorbance) associated with index of SiN_x films as a function of SiN_x thickness on textured surface under glass ambient and (b) corresponding solar cell efficiency from PC1D calculations.

6.4 Quantitative understanding of optical and cell efficiency loss as a function of index, ambient, and surface morphology

After analyzing optical and efficiency loss of cells with different SiN_x based AR coatings (index and thickness) and surface morphologies (planar and textured) individually, this section summarizes the quantitative understanding of why and which coating makes most economical sense for the highest module power output. Figures 6.7 and 6.8 show the calculated sum of reflectance and absorbance as a function of wavelength for various SiN_x films on a planar and textured surface, respectively, in air and under glass. For these calculations, best SiN_x thickness for each index was chosen for encapsulated cells under glass because module power output is the key figure of merit. Calculations were performed using Sunrays and the irradiance for these calculations was assumed normal.

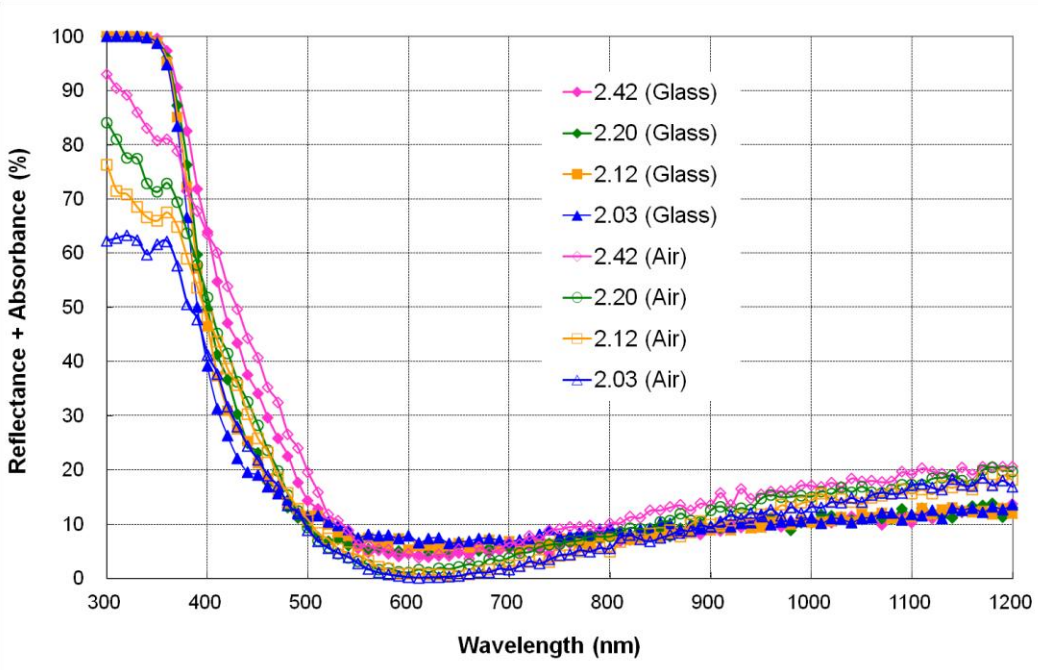

Figure 6.7: Calculated sum of reflectance and absorbance as a function of wavelength for various SiN_x films on a planar surface.

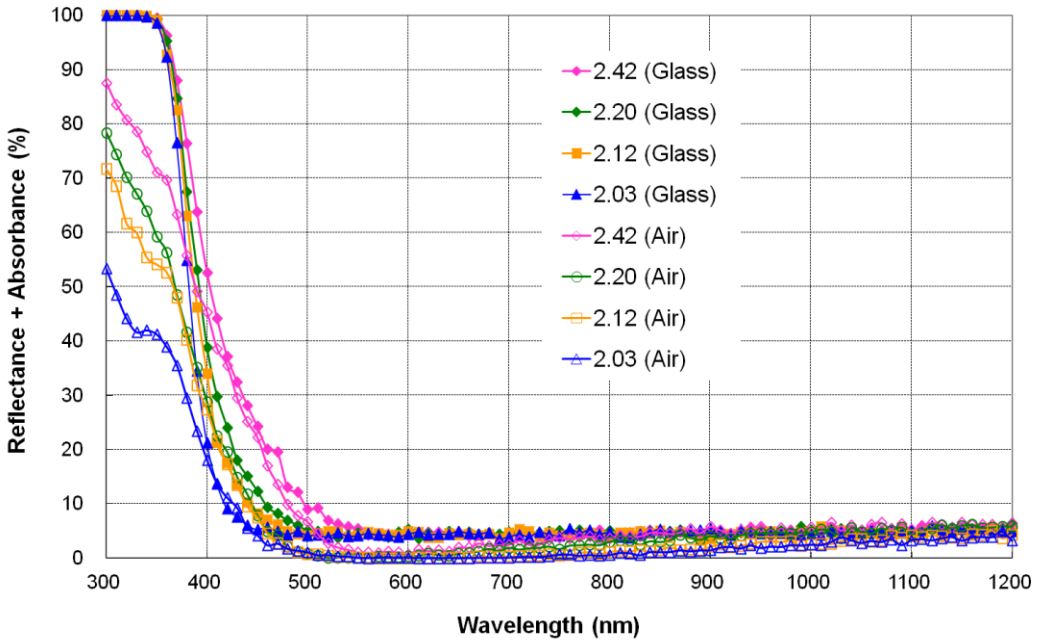

Figure 6.8: Calculated sum of reflectance and absorbance as a function of wavelength for various SiN_x films on a textured surface.

It is important to recognize that thickness optimization for module (under glass/EVA) will suppress the starting cell efficiency in air. Thus, even if a film gives small encapsulation loss, it may not give the highest module power. Table 6.4 summarizes the optical encapsulation loss and corresponding solar cell efficiency for various SiN_x films on planar and textured surfaces in air and under glass. Final solar cell efficiencies in Table 6.4 do not account for zero depth concentrator effect (+1.2%) [37, 74] and series resistance loss (-4%) because these two are not accounted for in Sunrays and PC1D models and are not need for concluding which film is best for module power output. To estimate the total encapsulated cell efficiency, one can simply add 2.8% efficiency loss (4% - 1.2%) to the total optical encapsulation loss calculated in this study to account for these two effects.

Table 6.4: Effect of refractive index, surface morphology (planar vs. textured), and ambient (air vs. glass) on optical loss and cell efficiency. AR coating thickness was optimized for each index to minimize optical losses under glass.

	Planar surface							
	Air (n = 1.0)				Glass (n = 1.5)			
AR thickness (nm)	76	74	68	62	76	74	68	62
Refractive index (n)	2.03	2.12	2.20	2.42	2.03	2.12	2.20	2.42
SiN_x reflectance (%)	10.2	10.5	11.1	13.3	6.3	5.4	4.9	4.3
SiN_x absorbance (%)	0.2	0.9	1.6	3.4	0.1	0.5	1.1	2.8
Glass reflectance (%)	0	0	0	0	4	4	4	4
Glass & EVA absorbance (%)	0	0	0	0	2.2	2.2	2.2	2.2
Total optical loss (%)	10.4	11.4	12.8	16.7	12.6	12.1	12.1	13.3
V_{oc} (mV)	628.6	628.3	627.8	626.4	627.7	627.9	627.9	627.5
J_{sc} (mA/cm^2)	33.6	33.2	32.7	31	32.5	32.7	32.8	32.3
Efficiency (%)	16.6	16.4	16.1	15.3	16.0	16.1	16.2	15.9
Efficiency loss (Eff_{Air} - Eff_{Glass})	0.6	0.3	-0.1	-0.6	N/A	N/A	N/A	N/A

	Textured surface							
	Air (n = 1.0)				Glass (n = 1.5)			
AR thickness (nm)	78	72	58	50	78	72	58	50
Refractive index (n)	2.03	2.12	2.20	2.42	2.03	2.12	2.20	2.42
SiN_x reflectance (%)	2.3	2.3	2.7	3.5	0.6	0.5	0.7	0.7
SiN_x absorbance (%)	0.4	1.3	2.2	4.1	0.1	0.7	1.3	2.8
Glass reflectance (%)	0	0	0	0	4	4	4	4
Glass & EVA absorbance (%)	0	0	0	0	2.1	2.1	2.1	2.1
Total optical loss (%)	2.7	3.6	4.9	7.6	6.8	7.3	8.0	9.6
V_{oc} (mV)	625.9	625.7	625.3	624.5	624.6	624.5	624.3	623.7
J_{sc} (mA/cm^2)	36.6	36.3	35.8	34.7	34.9	34.7	34.4	33.8
Efficiency (%)	17.9	17.7	17.5	17.0	17.1	17.0	16.8	16.5
Efficiency loss (Eff_{Air} - Eff_{Glass})	0.8	0.7	0.7	0.5	N/A	N/A	N/A	N/A

* Negative values in column "Efficiency loss (Eff_{Air} - Eff_{Glass}) denote that efficiency under glass is higher than in air.

Figure 6.9 summarizes the highest solar cell efficiency for each SiN_x film in air and under glass with and without the resistive and zero depth concentrator effect. It is clear that n = 2.03 with a thickness of 78 nm is the best coating for final module efficiency

(17.1%) regardless of ambient or surface texturing morphology. This is in spite of the fact that as refractive index increases from 2.03 to 2.42 for the textured cells, air to glass efficiency gap or encapsulation loss decreases from 0.8 to 0.5% (Table 6.4). In fact, SiNx film with n = 2.42 gave the lowest performance (16.5%) under glass even though air to glass efficiency loss was smallest (17.0% - 16.5% = 0.5%). Therefore, for the highest module power or efficiency, n = 2.03 with thickness of 78 nm is the best AR coating for textured mono-crystalline Si solar cells, but for the smallest air to glass loss, n = 2.42 is the best.

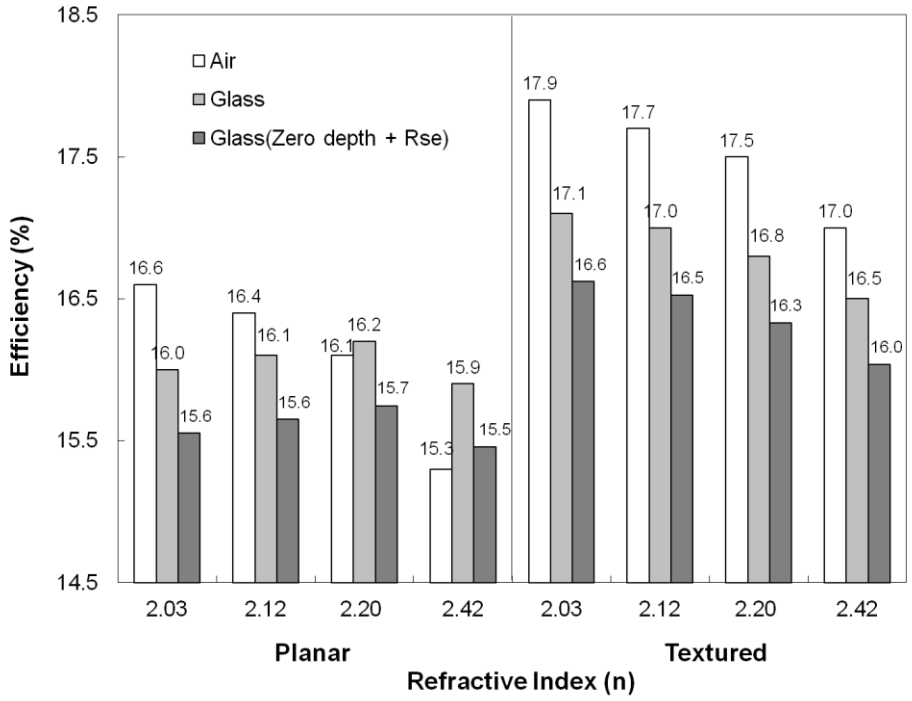

Figure 6.9: Simulated PC1D solar cell efficiency for each refractive index SiN_x film under air and glass with and without the zero depth concentrator effect (+1.2%) and series resistance loss (-4%).

Table 6.5 summarizes the simulation results using absorption-less no-iron glass/EVA compared to the 2.1% absorption in glass and EVA used in previous calculation (Table 6.4). Table 6.5 shows that reducing the glass and EVA absorption to zero increases the

cell performance by only 0.1 to 0.2%, which is less than the expected efficiency gain of ~0.3 to 0.4% (2.1% of 17% cell). Also notice that the 0.2% efficiency increase (17.1 to 17.3%) was for the n = 2.03 film while decreased to 0.1% for the high index n = 2.42 film (16.5 to 16.6%). This is because when the glass and EVA absorption is removed, absorption in SiN_x increases because glass, EVA, and SiN_x all absorb in the short wavelength regime. Short wavelength photons that were absorbed by B270 glass and EVA can now reach the SiN_x film, but some may get absorbed in the SiN_x film prior to reaching the cell. Increased absorbance in the higher index SiN_x films explains why efficiency enhancement is less for the high index absorbing film when the 2.1% absorption in glass/EVA is removed.

Table 6.5: Quantitative understanding of optical and cell efficiency for non-absorbing glass/EVA.

	Planar surface							
	Absorbing glass & EVA				Non-absorbing glass & EVA			
AR thickness (nm)	76	74	68	62	76	74	68	62
Refractive index (n)	2.03	2.12	2.20	2.42	2.03	2.12	2.20	2.42
SiN_x reflectance (%)	6.3	5.4	4.9	4.3	7.0	6.1	5.6	4.8
SiN_x absorbance (%)	0.1	0.5	1.1	2.8	0.3	1.1	1.9	4.0
Glass reflectance (%)	4	4	4	4	4	4	4	4
Glass & EVA absorbance (%)	2.2	2.2	2.2	2.2	0	0	0	0
Total optical loss (%)	12.6	12.1	12.1	13.3	11.3	11.2	11.5	12.7
V_{oc} (mV)	627.7	627.9	627.9	627.5	628	628.1	628	627.6
J_{sc} (mA/cm^2)	32.5	32.7	32.8	32.3	32.9	33	32.8	32.4
Efficiency (%)	16.0	16.1	16.2	15.9	16.2	16.3	16.2	16.0

	Textured surface							
	Absorbing glass & EVA				Non-absorbing glass & EVA			
AR thickness (nm)	78	72	58	50	78	72	58	50
Refractive index (n)	2.03	2.12	2.20	2.42	2.03	2.12	2.20	2.42
SiN_x reflectance (%)	0.6	0.5	0.7	0.7	0.8	0.8	0.8	0.8
SiN_x absorbance (%)	0.1	0.7	1.3	2.8	0.5	1.5	2.3	4.1
Glass reflectance (%)	4	4	4	4	4	4	4	4
Glass & EVA absorbance (%)	2.1	2.1	2.1	2.1	0	0	0	0
Total optical loss (%)	6.8	7.3	8.0	9.6	5.3	6.3	7.1	8.9
V_{oc} (mV)	624.6	624.5	624.3	623.7	625.1	624.8	624.5	624
J_{sc} (mA/cm^2)	34.9	34.7	34.4	33.8	35.4	35.1	34.7	34
Efficiency (%)	17.1	17.0	16.8	16.5	17.3	17.1	17.0	16.6

6.5 Conclusion

The performance of various SiN_x films was investigated by a combination of geometrical ray tracing simulation program Sunrays and PC1D device modeling program. Simulations showed that SiN_x film with n = 2.03 and thickness of 78 nm provides the highest cell efficiency under glass/EVA encapsulation for the pyramid textured mono-crystalline Si solar cells. The efficiency drops from 17.1% to 16.5% as you raise the index of the SiN_x film from 2.03 to 2.42 because of increase in reflectance + absorbance loss from 6.8% to 9.6% (this includes 4% reflection from front glass surface and 2.1% absorption in glass and EVA). For the cell design used in these simulations, the starting cell efficiency in air with 2.03 index film is 17.9% which drops to 17.0% in air with 2.42 index SiN_x AR coating. Although 2.42 index film shows the lowest optical encapsulation loss (17.0% - 16.5% = 0.5%), it has the lowest final encapsulation cell efficiency of 16.5%. If the final module efficiency is used as the figure of merit for the photovoltaics technology, then 2.03 is the index of choice for the textured mono-crystalline Si solar

cells. Identical optical analysis for planar cells showed that 2.42 index film gives the highest optical encapsulation gain (15.9% - 15.3% = 0.6%), but the index of 2.20 gives the highest encapsulated cell efficiency of 16.2%.

CHAPTER 7

INVESTIGATION OF ALD Al_2O_3 PASSIVATION DIELECTRIC

Atomic layer deposition (ALD) aluminum oxide (Al_2O_3) has become an active area of investigation because of its reported excellent passivation quality [18-21] of p-type silicon (Si). This passivation is attributed to its high negative charge, which creates an accumulation layer at the p-type Si surface to reduce the recombination. Schematic of ALD Al_2O_3 layer deposition process is described in Figure 7.1.

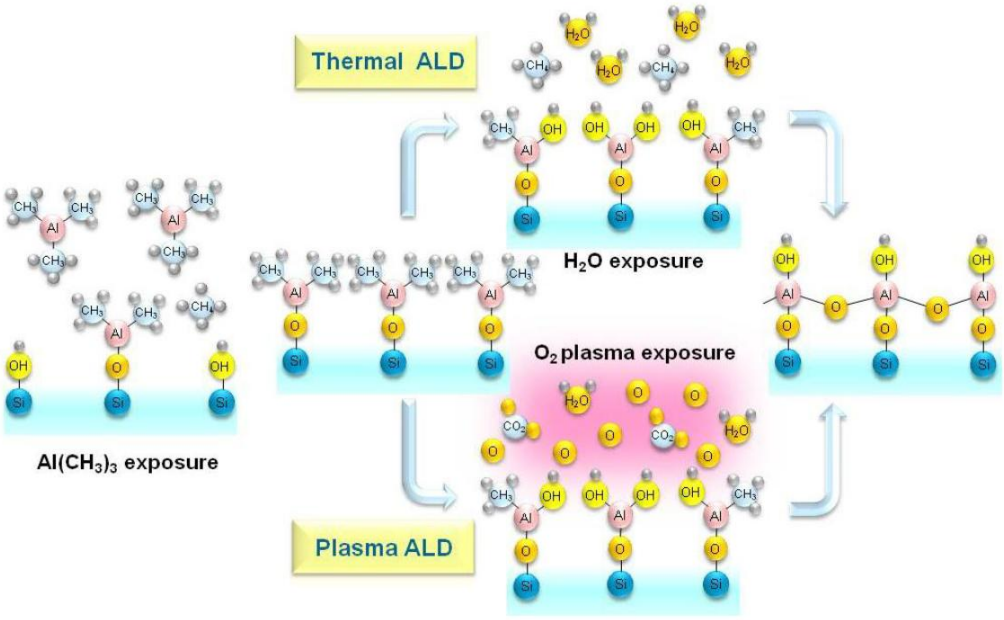

Figure 7.1: Schematic of thermal and plasma-assisted ALD Al_2O_3 layer deposition [75].

Several equipment builders have built high-throughput Al_2O_3 deposition systems, but it is still not being used for commercial production of cells because of some issues related to deposition and annealing conditions, thermal stability, and passivation quality after

firing of screen-printed contacts. This chapter investigates the deposition and annealing conditions for ALD Al_2O_3 film for achieving stable and high-quality passivation for commercial ready p-type and n-type screen-printing solar cells.

7.1 In-house thermal ALD Al_2O_3 passivation system

Passivation quality of thermal ALD Al_2O_3 passivated p-type Si is investigated in this chapter by extracting surface recombination velocity (SRV) using quasi-steady-state photo-conductance (QSSPC) measurements [76]. Figure 7.2 shows a picture of our in-house thermal ALD machine used in this study. Detailed deposition parameters for thermal ALD Al_2O_3 film are listed in Table 7.1. Each cycle of deposition consists of a H_2O pulse (5 msec) followed by trimethylaluminum (TMA: $Al_2(CH_3)_6$) pulse (15 msec). In this system, 72 ALD cycles can deposit Al_2O_3 film a thickness of ~10 nm.

Figure 7.2: Picture of in-house thermal ALD machine.

Table 7.1: Thermal ALD Al_2O_3 deposition parameters.

1	H_2O pulse time	5 msec
2	H_2O N_2 flow	20 sccm
3	H_2O N_2 purge time	5 sec
4	TMA pulse time	15 msec
5	TMA N_2 flow	20 sccm
6	TMA N_2 purge time	5 sec

7.1.1 Surface recombination velocity of thermal ALD Al_2O_3 passivated FZ Si samples

Figure 7.3 shows the SRV of thermal ALD Al_2O_3 passivated planar p-type 1 Ω-cm float zone (FZ) wafers as a function of annealing temperature. Thermal ALD Al_2O_3 films were deposited at a chamber temperature of 100℃ or 200℃ with thickness of 10 nm (72 cycles). As-deposited SRV values were in the range of 900–5000 cm/s and 100–600 cm/s for 100℃ and 200℃ deposition temperature, respectively. As-deposited samples were annealed in a rapid thermal processing (RTP) chamber with N_2 ambient at temperatures above 300℃ for 30 min. Figure 7.3 shows that as the annealing temperature is increased from 300 to 425℃ SRV decreases from 63 to 9 cm/s and from 110 to 10 cm/s for the films deposited at 100℃ and 200℃, respectively. Lowest SRV was achieved when annealing was done in the range of 375–425℃ regardless of chamber temperature. This indicates that post deposition annealing condition is more critical than the deposition temperature for achieving low SRV with thermal ALD Al_2O_3. It is important to note that a SRV of 10 cm/s is excellent for achieving high-efficiency cells if it can be maintained through the subsequent cell processing steps. This was investigated in the following experiment.

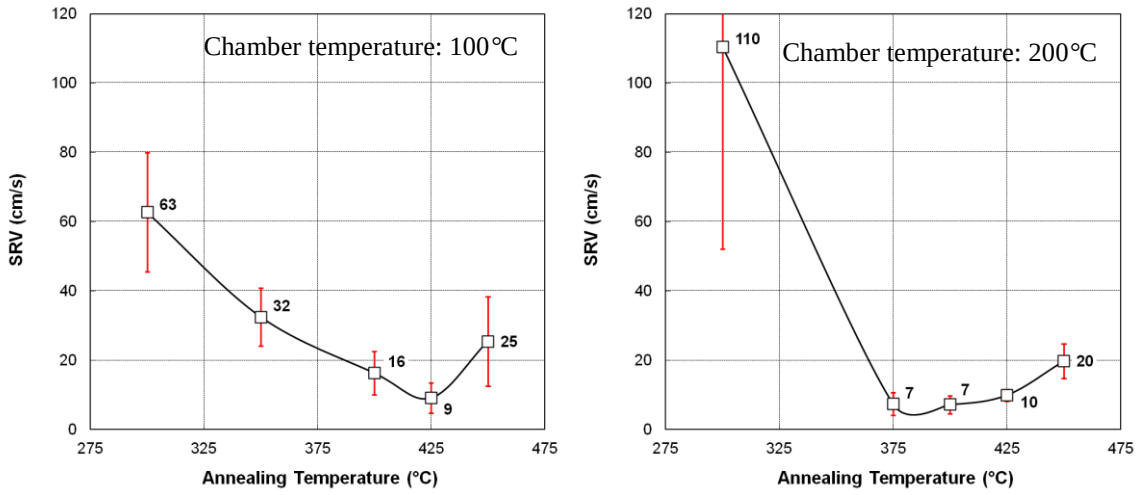

Figure 7.3: SRV of in-house thermal ALD Al_2O_3 passivated planar p-type 1 Ω-cm FZ wafers as a function of annealing temperature deposited at chamber temperature of (a) 100℃ and (b) 200℃.

Figure 7.4 tracks the change in SRV of thermal ALD Al_2O_3 passivated planar FZ wafers through typical solar cell fabrication steps including silicon-nitride (SiN_x) deposition and contact firing cycle which may come after the Al_2O_3 deposition. Samples annealed at 425℃ were capped with SiN_x film followed by high temperature (800℃) infrared (IR) belt furnace firing to simulate the firing of screen-printing contact formation. Note that the SRV showed only a slight change after SiN_x deposition but increased substantially to 60–120 cm/s after firing. However, a subsequent forming gas anneal at 400℃ for 20 min restored the SRV value back to ~30 cm/s.

Above study is pertinent for p-type high-efficiency passivated emitter rear contact (PERC) [21] solar cells where the Al_2O_3/SiN_x passivation can be used on the back surface, which is frequently planarized to improve back surface reflectance and passivation. However, Al_2O_3 passivation can also play a very important role in passivating boron emitters for n-base solar cells. In this case, front surface has to be textured to reduce

reflectance. Therefore, in the next section, Al_2O_3 passivation of a textured Si surface is investigated.

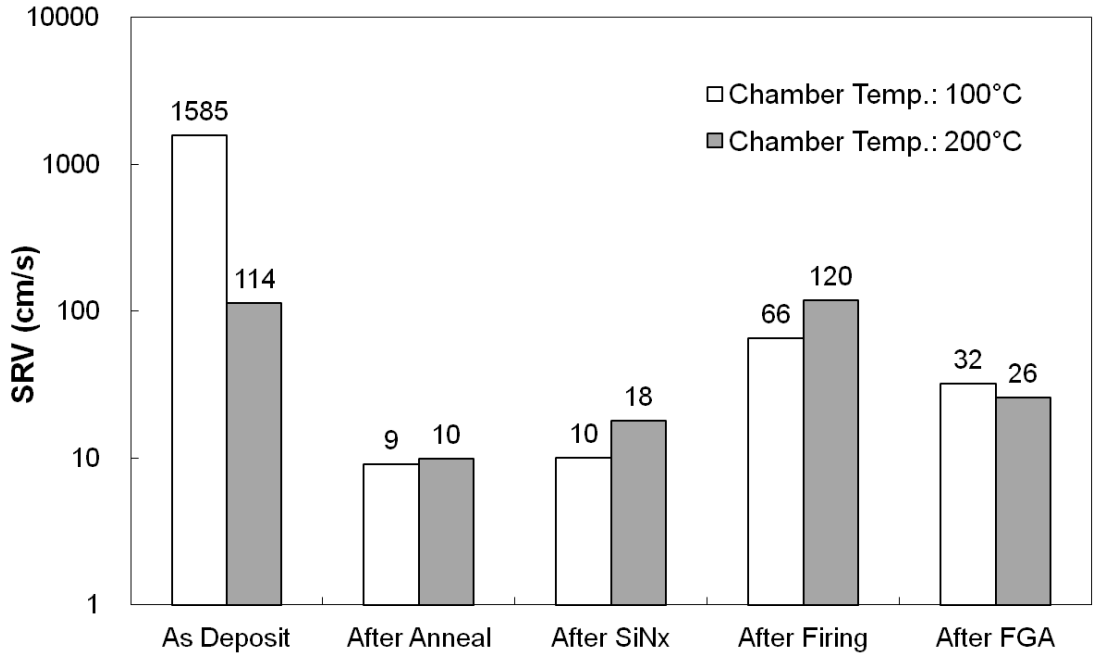

Figure 7.4: SRV tracking of FZ wafers through solar cell fabrication process flow.

Figure 7.5 shows the result of investigation of thermal ALD Al_2O_3 passivation of textured FZ wafers without the boron emitter. A 10 nm thermal ALD Al_2O_3 were deposited at chamber temperature of 200℃ and annealed at 425℃ in RTP chamber for 30 min. SRV of the textured wafers, even after annealing, was found to be 32 times higher (322 cm/s) than the counterpart planar wafers (10 cm/s). It is interesting to note that this is significantly higher than the ratio of the area of textured and planar surface which is about a factor of 1.7. This indicates that surface morphology also plays an important role in attaining excellent passivation from thermal ALD Al_2O_3. In the case of

planar surface, Al_2O_3 is deposited on (100) Si surface while textured surface has (111) orientation.

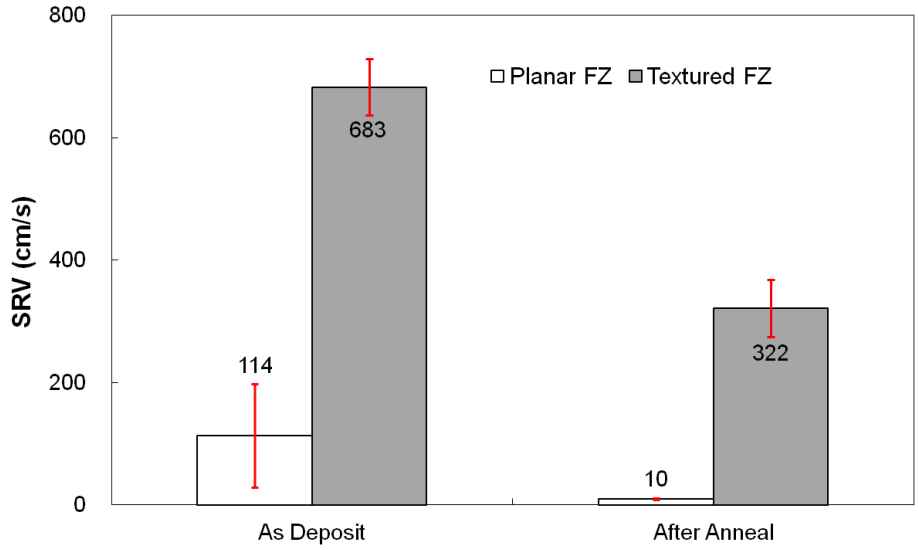

Figure 7.5: SRV of in-house thermal ALD Al_2O_3 passivated planar and textured p-type 1 Ω-cm FZ wafers.

7.1.2 Surface recombination velocity of thermal ALD Al_2O_3 passivated Cz Si samples

In the previous studies, FZ wafers were used, however most commercial cells are made on large area Czochralski (Cz) wafers. Therefore, in this section, the difference in Al_2O_3 passivation of Cz and FZ wafers was investigated. Figure 7.6 shows the SRV of thermal ALD Al_2O_3 passivated KOH planarized p-type 2 Ω-cm Cz wafers as a function of annealing temperature. All the Al_2O_3 films were deposited at a chamber temperature of 200℃ with thickness of 10 nm (72 cycles). As-deposited samples were annealed in RTP chamber with N_2 ambient at temperatures above 300℃ for 30 min. SRV of thermal ALD Al_2O_3 passivated Cz wafers was found to be higher than the FZ wafers for the same

annealing temperature. For example, an SRV of 10 cm/s was achieved on FZ wafer while the corresponding SRV was 64 cm/s on the Cz wafer. Different SRV may come from different surface finish. Planarization of Cz wafers was performed in our lab with KOH etching while the FZ wafers were factory polished. This indicates that surface finish is also important for attaining the passivation potential of thermal ALD Al_2O_3.

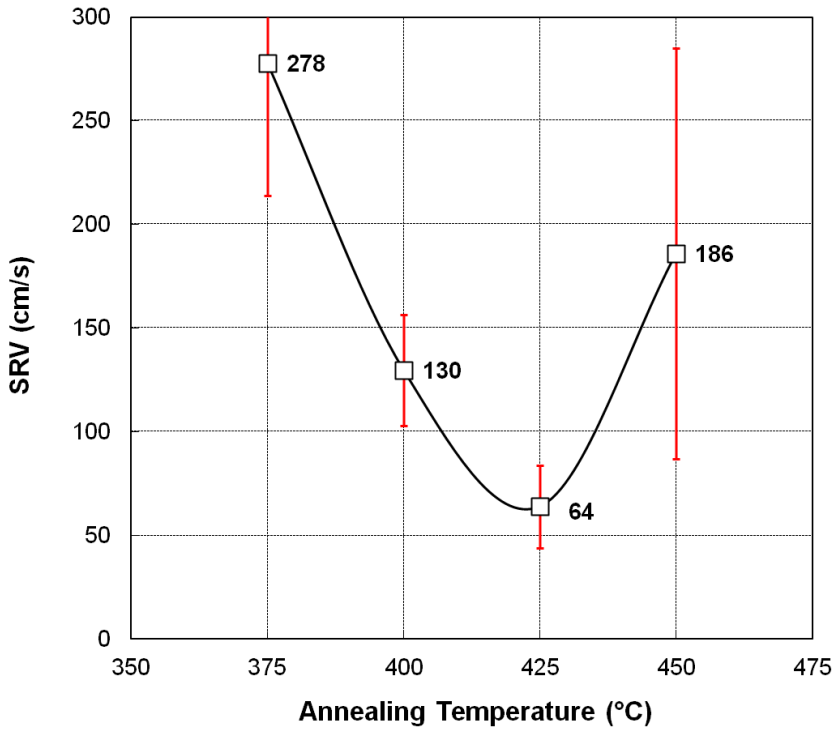

Figure 7.6: SRV of thermal ALD Al_2O_3 passivated KOH planarized p-type 2 Ω-cm Cz wafers as a function of annealing temperature.

Figure 7.7 shows the change in SRV of thermal ALD Al_2O_3 passivated planarized and textured Cz wafers as a function of subsequent solar cell fabrication steps involving SiN_x deposition and contact firing. Again 10 nm Al_2O_3 was deposited on all samples at 200°C and annealed in the RTP chamber at 425°C for 30 min followed by SiN_x capping and high temperature (800°C) IR belt furnace firing. Figure 7.7 shows that after SiN_x

deposition and contact firing steps, SRV of a textured Cz wafer ends up at 857 cm/s, which is more than six times larger than the planar Cz wafer. SRV on KOH planarized wafers reached over 100 cm/s after firing which is quite high for high-efficiency solar cells. For more than 20% efficient solar cells, SRV should be below 100 cm/s. Therefore, to achieve SRV of below 100 cm/s after firing for both KOH planarized and textured Cz wafers, further optimization is required.

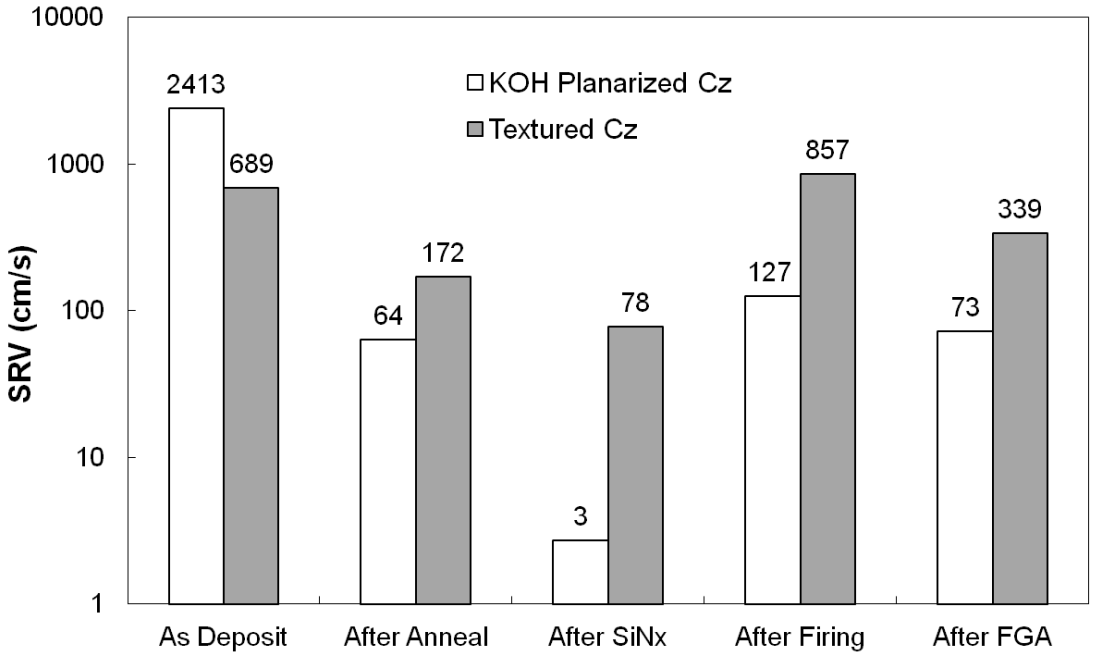

Figure 7.7: SRV tracking of KOH planarized and textured Cz wafers through solar cell fabrication process flow.

7.1.3 J_{oe}, implied V_{oc}, and solar cell performance passivated with thermal ALD Al_2O_3

To investigate the feasibility of thermal ALD Al_2O_3 on commercial-ready solar cells, emitter saturation current (J_{oe}) and implied open circuit voltage (V_{oc}) was measured, and

then (2×2 cm^2) screen-printing solar cells were fabricated. For J_{oe} measurement, 45 Ω/sq symmetric boron emitter was formed on planar high resistivity (~500 Ω-cm) FZ n-type wafers. For implied V_{oc} measurements and solar cell fabrication, structures shown in Figure 7.8 were fabricated on both side textured wafers. Figure 7.9 shows that J_{oe} decreased and implied V_{oc} increased after firing for these different structures which conflicts with the observed SRV trend in Figure 7.4 for undiffused wafers. Complete n- and p-type screen-printed solar cells passivated with thermal ALD Al_2O_3 were fabricated and compared with silicon dioxide (SiO_2) passivated n- and p-type solar cells. Table 7.2 shows that solar cells with thermal ALD Al_2O_3 passivation gave significantly lower cell performance compared to the SiO_2 passivated devices which were nearly 20% with V_{oc} of 650 mV. This was consistent with the SRV data but contrary to the hope that negative charge in Al_2O_3 will enhance passivation. It may still be possible to achieve that goal by using a better ALD system and further optimization of growth and annealing. Since recent reports on plasma-assisted ALD Al_2O_3 deposition [19, 75] have been positive, we decided to switch to plasma-assisted ALD Al_2O_3 passivation of Si wafers and cells in the next section.

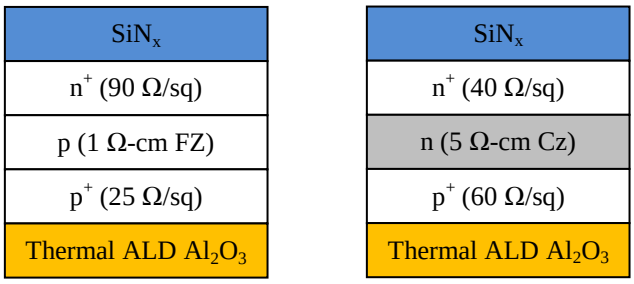

Figure 7.8: p- (left) and n-type (right) solar cell structures for implied V_{oc} measurement.

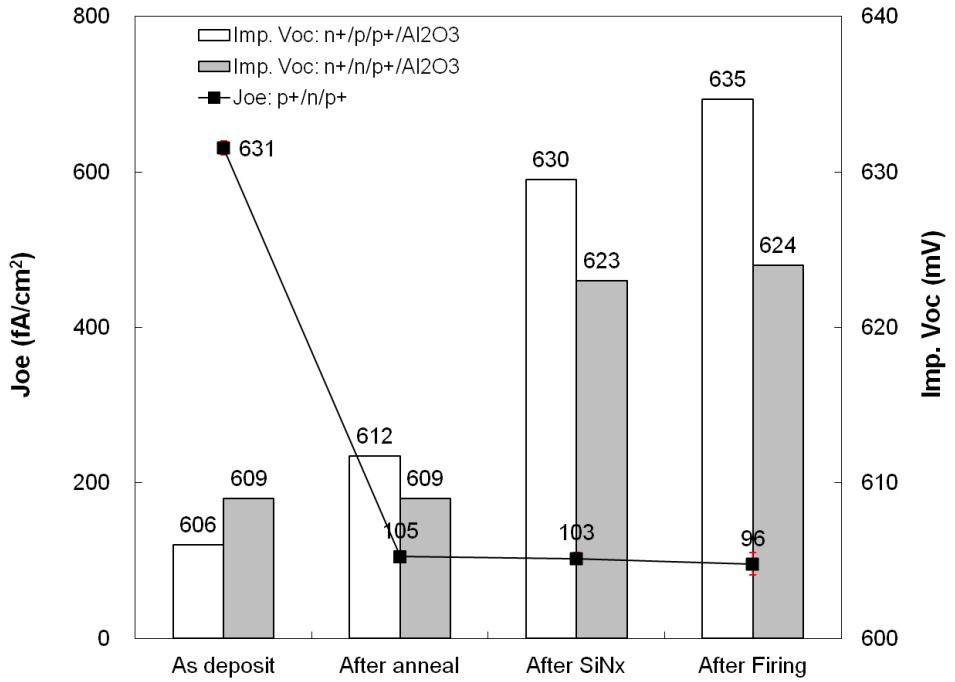

Figure 7.9: J_{oe} and implied V_{oc} measurement.

Table 7.2: Solar cell parameters of thermal ALD Al_2O_3 and SiO_2 passivated solar cells.

Structure	Area (cm^2)	V_{oc} (mV)	J_{sc} (mA/cm^2)	FF	Eff (%)	R_{se} (Ω-cm^2)	R_{sh} (Ω-cm^2)
$n^+/p/p^+/Al_2O_3$	4	638	38.2	0.746	18.2	1.11	3343
$n^+/p/p^+/SiO_2$	4	652	39.8	0.764	19.8	1.13	2132
$n^+/n/p^+/Al_2O_3$	4	624	33.5	0.538	11.3	7.49	2057
$n^+/n/p^+/SiO_2$	N/A (Broken during cell processing)						

7.2 Plasma-assisted ALD Al_2O_3 passivation

Passivation quality of plasma-assisted ALD Al_2O_3 film on p-type Si has been investigated in this section. Cambridge NanoTech Fiji F202 plasma ALD system was used to deposit plasma-assisted ALD Al_2O_3 films. SRV was extracted from QSSPC measurements. Plasma-assisted ALD Al_2O_3 deposition mechanism is shown in Figure 7.1, and detailed deposition parameters are listed in Table 7.3. Each cycle of deposition is

consisted of a TMA pulse (0.06 sec) followed by 20 sccm O_2 flow with plasma power of 300 W for 20 sec (Figure 7.11). In this system, 70 ALD cycles can deposit ~7 nm thick Al_2O_3 film.

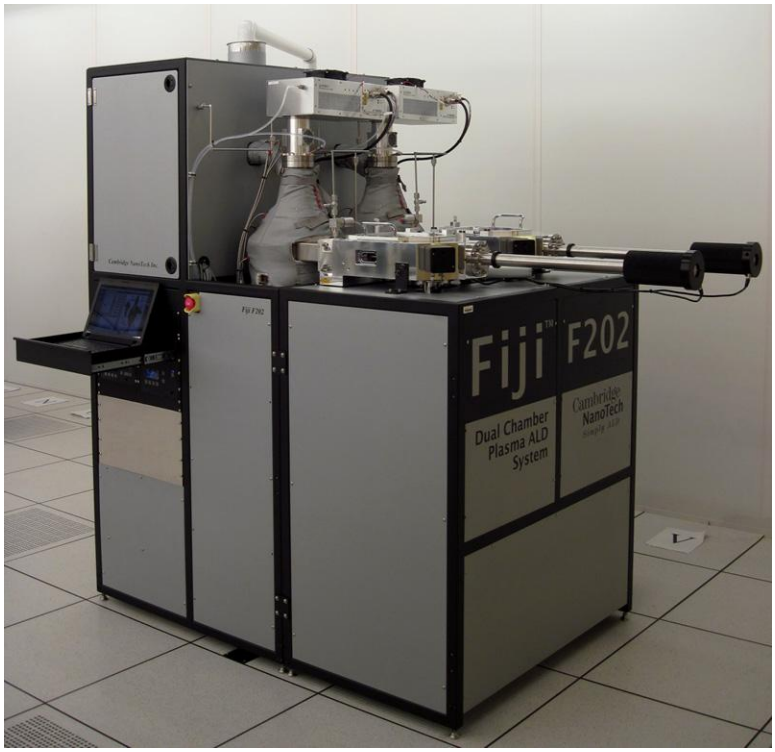

Figure 7.10: Picture of Cambridge NanoTech plasma-assisted ALD machine.

Table 7.3: Plasma-assisted ALD Al_2O_3 deposition parameters.

1	TMA pulse time	0.06 sec
2	Wait	5 sec
3	O_2 flow	20 sccm
4	Wait	5 sec
5	Plasma	300 W
6	Wait	20 sec

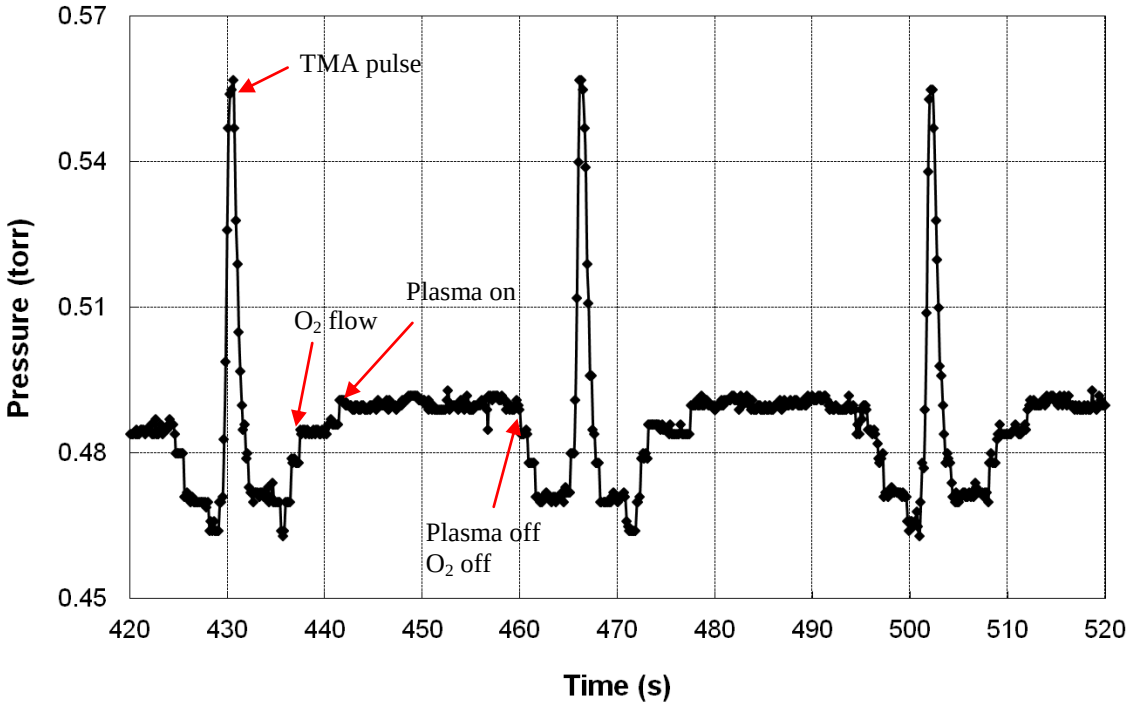

Figure 7.11: Chamber pressure during plasma-assisted ALD deposition.

7.2.1 Surface recombination velocity of plasma-assisted ALD Al_2O_3 passivated Cz Si samples

SRV on plasma-assisted ALD Al_2O_3 passivated KOH planarized and textured Cz wafers was investigated (Figure 7.12). About 7 nm plasma-assisted ALD Al_2O_3 films were deposited at chamber temperature of 250℃. No separate anneal was performed, instead thermal cycle during the SiN_x anneal was used for annealing the film. After the SiN_x deposition, samples were subjected to contact firing cycle to simulate cell fabrication. SiN_x coating deposition was done in a plasma-enhanced chemical-vapor deposition (PECVD) chamber at 450℃ for 20 min. Figure 7.12 shows that for KOH planarized Cz samples, average SRV of 30 cm/s was obtained after SiN_x deposition which increased to 97 cm/s after the contact firing cycle. Notice that this is lower than the

thermal ALD Al_2O_3 which gave an SRV of 127 cm/s (Figure 7.7). For the textured Cz samples, average SRV was 57 cm/s after SiN_x deposition and increased to 150 cm/s after the firing cycle. This is significantly lower than thermal ALD Al_2O_3 which gave an SRV of 857 cm/s (Figure 7.7). In addition, SRV difference between planarized (97 cm/s) and textured (150 cm/s) samples correspond to the surface area difference of 1.7. This indicates that plasma-assisted ALD Al_2O_3 passivates textured Si (111) surface just as well as (100) planar surface because the SRV increase only comes from area not morphology of surface orientation (100 vs. 111).

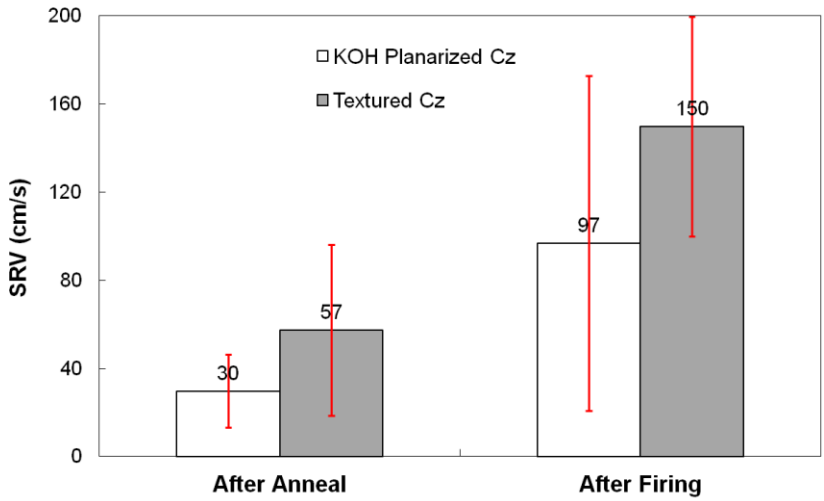

Figure 7.12: SRV of plasma-assisted ALD Al_2O_3 passivated 2 Ω-cm Cz wafers.

For further optimization, deposition chamber temperature was varied from 150 to 250℃. Figure 7.13 indicates lower chamber temperature provided even better SRV. SRV of below 30 cm/s and 15 cm/s achieved after SiN_x deposition and firing when the chamber temperature was reduced to 200℃ and 150℃, respectively. This is low enough for greater than 20% efficient p-type PERC solar cells. In addition, high thermal stability

with respect to contact firing makes plasma-assisted ALD Al_2O_3 film an alternative candidate for commercial-ready screen-printing solar cells.

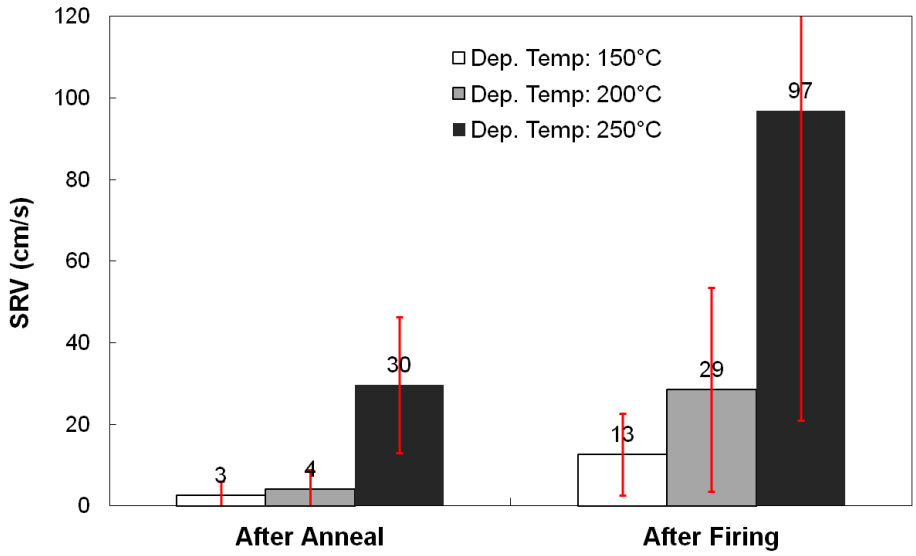

Figure 7.13: SRV of plasma-assisted ALD Al_2O_3 passivated 2 Ω-cm Cz wafers as a function of deposition chamber temperature.

7.2.2 Fabrication of large-scale commercial-ready solar cells passivated with plasma-assisted ALD Al_2O_3

After establishing the deposition and anneal conditions for plasma-assisted ALD Al_2O_3 film for excellent SRV, commercial-ready screen-printed large area (239 cm^2) p- and n-type solar cells with plasma-assisted ALD Al_2O_3 passivation were fabricated and compared with SiO_2 passivated solar cells. For n-type solar cells, plasma-assisted ALD Al_2O_3 was deposited for front side boron emitter passivation while p-type solar cells, Al_2O_3 was deposited for back side p-type surface passivation. Figure 7.14 shows the cell structures and corresponding process sequence, and Table 7.4 summarizes solar cell parameters fabricated on both side textured wafers. Use of plasma-assisted ALD Al_2O_3

passivation showed a clear improvement in V_{oc}, J_{sc}, and cell efficiency for both n- and p-type solar cells compared to the counterpart SiO_2 passivation. Note that Al_2O_3 passivation of textured p^+ boron emitter gave 0.3% improvement in cell efficiency compared to textured SiO_2 passivated boron emitter. On p-type PERC cell, it is known that SiO_2 passivation of textured back p-surface is highly detrimental to cell performance which was also validated in Table 7.4, resulting in 17.7% efficiency. However, Al_2O_3 passivation of textured p-surface raised that efficiency to 18.6%. That is why most PERC cells are made with planar back surface. Better passivation quality of plasma-assisted ALD Al_2O_3 (Figure 7.12) on textured surface is attributed to its field-induced passivation effect, which is insensitive to surface orientation. However, SiO_2 is quite sensitive to surface orientation [77]. SiO_2 does not passivate (111) surface as effectively as ALD Al_2O_3. Even though our work on thermal ALD did not reveal this effect due to poor interface quality, but plasma-assisted ALD did validate the concept and show promise for commercial Si solar cells.

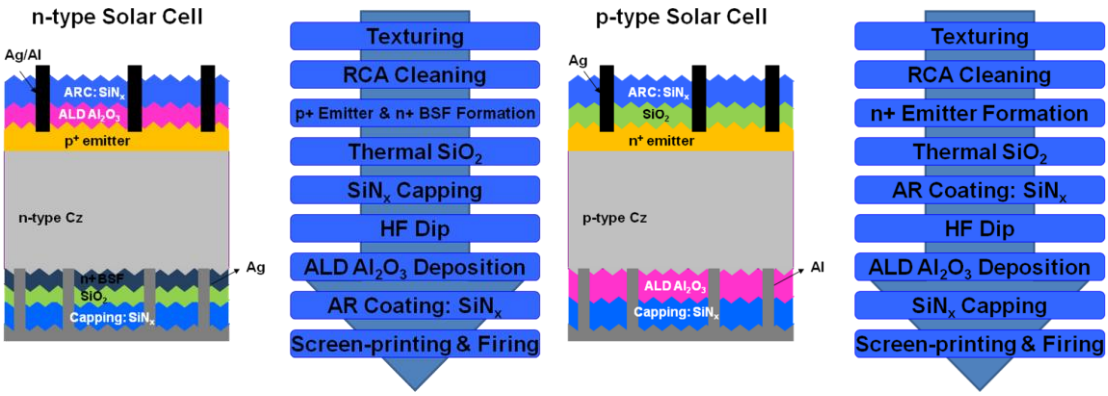

Figure 7.14: Solar cell structures and corresponding process sequence

Table 7.4: Solar cell parameters of plasma-assisted ALD Al_2O_3 and SiO_2 passivated solar cells.

Bulk	Structure	Area (cm^2)	V_{oc} (mV)	J_{sc} (mA/cm^2)	FF	Eff (%)	R_{se} (Ω-cm^2)	R_{sh} (Ω-cm^2)
n-type Cz	$Al_2O_3/p^+/n/n^+$	239	654	38.8	0.780	19.8	0.894	7337
	$SiO_2/p^+/n/n^+$	239	650	38.8	0.771	19.5	1.07	44693
p-type Cz	$n^+/p/Al_2O_3$	239	641	37.4	0.777	18.6	0.612	8536
	$n^+/p/SiO_2$	239	634	36.5	0.765	17.7	0.462	2740

7.3 Conclusion

Plasma-assisted ALD Al_2O_3 provided excellent passivation for a p-type Si surface after proper deposition, annealing, and firing. This is the result of large negative charge, which creates an accumulation layer at the p-type Si surface to reduce the recombination. Plasma-assisted ALD Al_2O_3 gave SRV of less than 10 cm/s after annealing and remained below 30 cm/s after contact firing cycle on planarized Cz wafers. For textured Cz wafers, SRV of 57 cm/s after annealing and 150 cm/s after firing was achieved which is superior to full aluminum-back-surface field and SiO_2 passivation of textured surface. Large area (239 cm^2) commercial-ready screen-printed Cz solar cells with textured back and plasma-assisted ALD Al_2O_3 coating were fabricated and compared with SiO_2 passivated textured back solar cells. About 0.3% absolute efficiency gain for n-type cell and 0.9% absolute efficiency enhancement for p-type cells was obtained by using ALD Al_2O_3 passivation on double side textured wafers compared to the SiO_2 passivated cells.

CHAPTER 8

SIMPLE ANALYTICAL MODEL TO QUANTIFY THE PV MODULE-COST PREMIUM ASSOCIATED WITH MODULE EFFICIENCY AND CELL TECHNOLOGY

Photovoltaics (PV) industry has experienced a remarkable growth due to rising interest in green energy, PV cost reduction, and favorable policies [6-8, 78, 79]. Various technologies are being investigated with the objective of increasing cell efficiency and reducing the cost to attain grid parity. Cost reduction can come from either module or balance of system (BOS) cost. Since total BOS cost is a function of module efficiency due to area-related BOS components, module cost needs to be adjusted to account for the difference in BOS cost in order to maintain the same installed system cost or levelized cost of electricity (LCOE) [47]. In this chapter, a simple model with analytical equations is developed to rapidly determine the equivalent cost for different modules with different efficiencies, material parameters or technologies, operating conditions, and BOS costs so that the final LCOE remains same.

Model accounts for different cell technologies and operating conditions by allowing the change in temperature coefficient (γ) for efficiency degradation, module efficiency, and irradiance weighted operating cell temperature (T_{iwoct}) simultaneously. Calculations were performed to compare four promising cell technologies, namely crystalline Si (c-Si), copper indium gallium diselenide (CIGS), cadmium telluride (CdTe), and amorphous Si (a-Si). Since BOS cost can be different in different regions of the world and may decrease

in the future [6, 78], calculations are also performed to quantify the impact of BOS cost on module efficiency premium using the analytical equations.

8.1 Analytical equations to assess the module cost

This section describes the analytical model to quantify the equivalent cost of any module relative to a reference module so that LCOE remains unchanged. Cost of an installed PV system consists of module cost (C_{Mod}), area-related BOS cost (C_{Area}), and fixed or indirect BOS cost (C_{Fix}) [47]. Sum of all cost components, except the module, is referred to as total BOS cost (C_{BOS}).

$$System \quad Cost = C_{Mod} + C_{Area} + C_{Fix} = C_{Mod} + C_{BOS} \tag{8.1}$$

Area-related BOS cost consists of wiring/mounting hardware and installation labor cost, which varies linearly with the number of modules or system area. Therefore, area-related BOS cost is inversely proportional to module efficiency because higher efficiency module requires fewer modules for a given size system (kW). Fixed or indirect cost includes permitting, commissioning, engineering, design, site preparation, grid connection, management, sales tax, installer margin, overhead, and insurance which is generally independent of system area or module efficiency. Similarly inverter cost is independent of module efficiency because it is dictated by system size.

To compare modules from the same material and technology (same γ and T_{iwoct}) but different efficiencies, the module costs should be adjusted to provide same installed system cost or LCOE. Since C_{Area} depends on module efficiency (η), cost of a new module in this case must be adjusted simply by an amount equal to the difference in the C_{Area}. Therefore, module cost (C_{Mod}) of different efficiency module can be expressed as

$$C_{Mod} = C_{Mod\_ref} + C_{Area\_ref} \cdot \left(\frac{\eta - \eta_{ref}}{\eta} \right) \tag{8.2}$$

where C_{Area_ref}, η_{ref}, and C_{Mod_ref} is area-related BOS cost, efficiency, and cost of the reference module.

Analytical equation (8.2) only accounts difference in module efficiency but does not account for the difference in γ and T_{iwoct}, which dictate the operating temperature induced efficiency degradation [11, 47, 80, 81]. This is important when cells or modules from different semiconductor materials are used which can have different value for γ and T_{iwoct} (Table 8.1). Difference in T_{iwoct} can occur from change in climate or location, mounting strategy, and module structure [47, 82]. For example, polymer/thin film/steel structure is used for thin film modules (CIGS, CdTe, and a-Si) while glass/cell/polymer structure is used for c-Si module. Modules can also run cooler if mounted for better air flow or have some passive cooling features. Therefore, in the following section we have modified analytical equations to account for the impact of γ and T_{iwoct}, in addition to efficiency, on module cost.

Since percentage of efficiency loss is defined as $\gamma \cdot (T_{iwoct} - 25°C)$ where γ is negative number expressed as %/°C, a module with lower absolute value of γ will lose less power and produce more energy. This extra energy can be monetized in terms of module cost ($/W). To accomplish this, we defined a normalized loss of cell efficiency as a compensation factor 'β' to account for the temperature-induced difference in efficiency degradation of the new module with respect to the reference module and is described as

$$\beta = \frac{[100 + \gamma \cdot (T_{iwoct} - 25°C)]}{[100 + \gamma_{ref} \cdot (T_{iwoct\_ref} - 25°C)]} \tag{8.3}$$

Since the module with lower γ produces more energy in spite of the same system size, the installed system cost of the two systems need to be adjusted to attain the same LCOE. According to our model, this can be accomplished by multiplying the system cost with reference module by 'β' and equating it to the system cost with the new module.

$$New\ \ System\ \ Cost = C_{Mod} + C_{Fix} + C_{Var} = \beta \cdot \left(C_{Mod\_ref} + C_{Fix\_ref} + C_{Var\_ref}\right) \tag{8.4}$$

$$where\ \ C_{Fix} = C_{Fix\_ref}\ \ and\ \ C_{Var} = C_{Var\_ref}\frac{\eta_{ref}}{\eta}$$

$$\therefore C_{Mod} = \beta \cdot C_{Mod\_ref} + (\beta - 1) \cdot C_{Fix\_ref} + \left(\beta - \frac{\eta_{ref}}{\eta}\right) \cdot C_{Var\_ref} \tag{8.5}$$

Table 8.1: Temperature coefficient (γ) and T_{iwoct} for four commercially important terrestrial PV materials. T_{iwoct} was computed for south-facing open-rack-mounted PV arrays at latitude tilt on Phoenix, AZ (33.4°) and Boston, MA (42.4°).

Material	Bandgap (eV)	γ (%/°C)	T_{iwoct} (°C) at Phoenix	T_{iwoct} (°C) at Boston
Crystalline silicon (c-Si)	1.12	-0.45	47.3	27.3
Copper indium gallium diselenide (CIGS)	1.04–1.68	-0.34	45.1	24.9
Cadmium telluride (CdTe)	1.44	-0.25	45.1	24.9
Amorphous silicon (a-Si)	1.4–1.9	-0.20	45.1	24.9

8.2 Applications of the analytical equations to establish the equivalent cost of modules with different efficiency and temperature coefficient resulting in the same LCOE

After establishing the analytical equation (8.5), next step was to apply it to four promising commercial PV materials (c-Si, CIGS, CdTe, and a-Si) with different efficiency and temperature coefficient. For equivalent module cost calculations, system cost and parameters for a reference system need to be defined. Table 8.2 lists the

reference system costs and parameters used for these calculations. Since efficiency impacts the BOS cost, calculations were performed for total BOS cost ranging from \$0.5–4/W and with fixed and variable BOS costs accounting for 50% of the total BOS.

Table 8.2: Reference inputs used for module cost calculations.

Item	Value
Module cost (\$/W)	1.00
Module efficiency (%)	16
γ (%/°C)	-0.45
T_{iwoct} (°C)	47.3

8.2.1 Determination of the Si module cost as a function of module efficiency for the same LCOE

Using the analytical equation (8.2), calculations were performed to quantify the equivalent cost of different efficiency c-Si modules which results in the same installed system cost and LCOE. In the first example, the γ and T_{iwoct} were kept constant and only the efficiency was varied. This corresponds to c-Si modules with different efficiency but same temperature coefficient. Calculations were performed for various area-related BOS costs in the range of \$0.25–2/W using a 16% efficient reference Si module at \$1/W. Note that BOS cost can be very different in different regions of the world and may decrease further in the future, therefore, equivalent module cost is also region dependent. Recall that area-related BOS cost varies with efficiency $\left(C_{Var} = C_{Var\_ref} \cdot \eta_{ref} / \eta\right)$. Each curve in Figure 8.1 represents the same system cost and LCOE for a given BOS cost. Figure 8.1 reveals quantitatively that as the area-related BOS cost decreases, the cost premium (additional cost for high efficiency) for higher efficiency modules decreases. For example, a 16% mono-Si modules has a premium of \$0.29/W over a 14% multi-crystalline-Si

module when area-related BOS cost is \$2/W. This premium decreases to \$0.07/W when area-related BOS cost drops to \$0.5/W. According to Figure 8.1, if a 16% module sells for \$1/W, the 14% efficient module should be sold for \$0.71/W in a region where the area-related BOS cost is \$2/W and for \$0.93W in a region with area-related BOS cost of \$0.5/W.

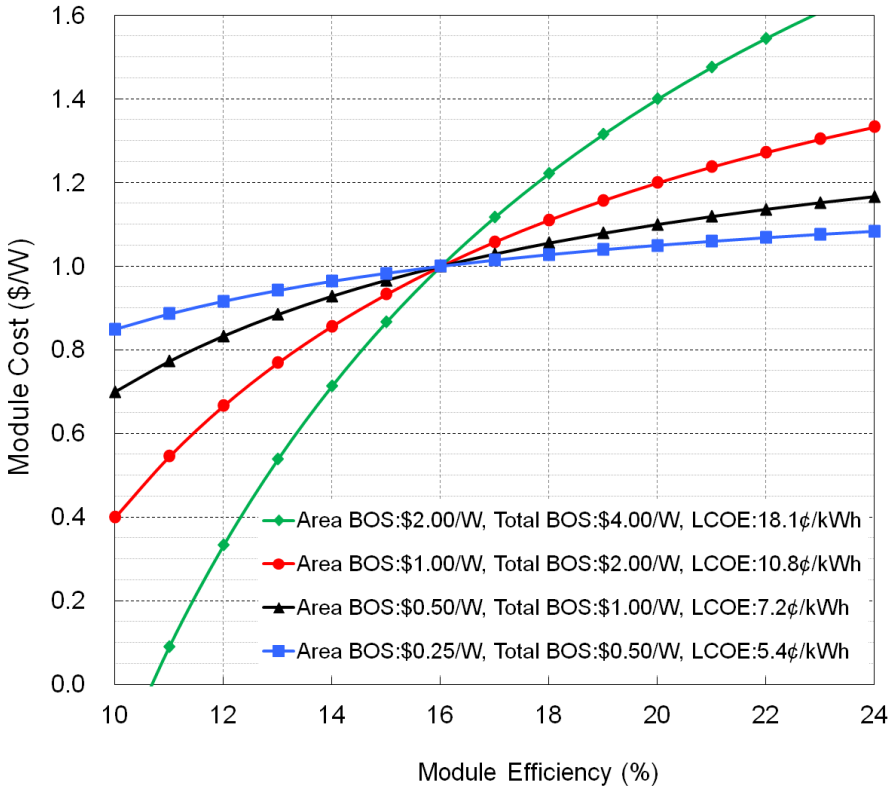

Figure 8.1: c-Si module costs as a function of module efficiency for various BOS costs with \$1/W 16% efficient c-Si reference module. Each curve represents a constant LCOE. LCOE were calculated with an assumption of weighted average cost of capital (WACC) = 7.7% without investment tax credit (ITC) in Phoenix.

8.2.2 Determination of equivalent cost of modules made from different materials and cell technologies (c-Si, CIGS, CdTe, and a-Si)

In this section, analytical equation (8.5) was applied to establish equivalent cost of modules made from different materials and technologies (different γ and T_{iwoct}) while

maintaining the same LCOE. Results are plotted in Figure 8.2 for various BOS conditions with respect to reference module efficiency of 16% at \$1/W. Calculations in Figure 8.2(a) reveal that every 0.05%/°C reduction in γ commands a 2¢/W, 2.5¢/W, 4¢/W, and 6¢/W increase in module price for a total BOS cost of \$0.5/W, \$1/W, \$2/W, and \$4/W, respectively. This is reflected in the increased steepness of the slope as the BOS increases. Calculations in Figure 8.2(b) reveal that every 5°C reduction in T_{iwoct} could command for 4¢/W, 5¢/W, 8¢/W, and 13¢/W increase in module price for a total BOS cost of \$0.5/W, \$1/W, \$2/W, and \$4/W, respectively. Note that each curve in Figures 8.2(a) and (b) correspond to a fixed BOS and fixed LCOE, but the installed system cost changes with γ and T_{iwoct} because module price has to be adjusted according to the energy production.

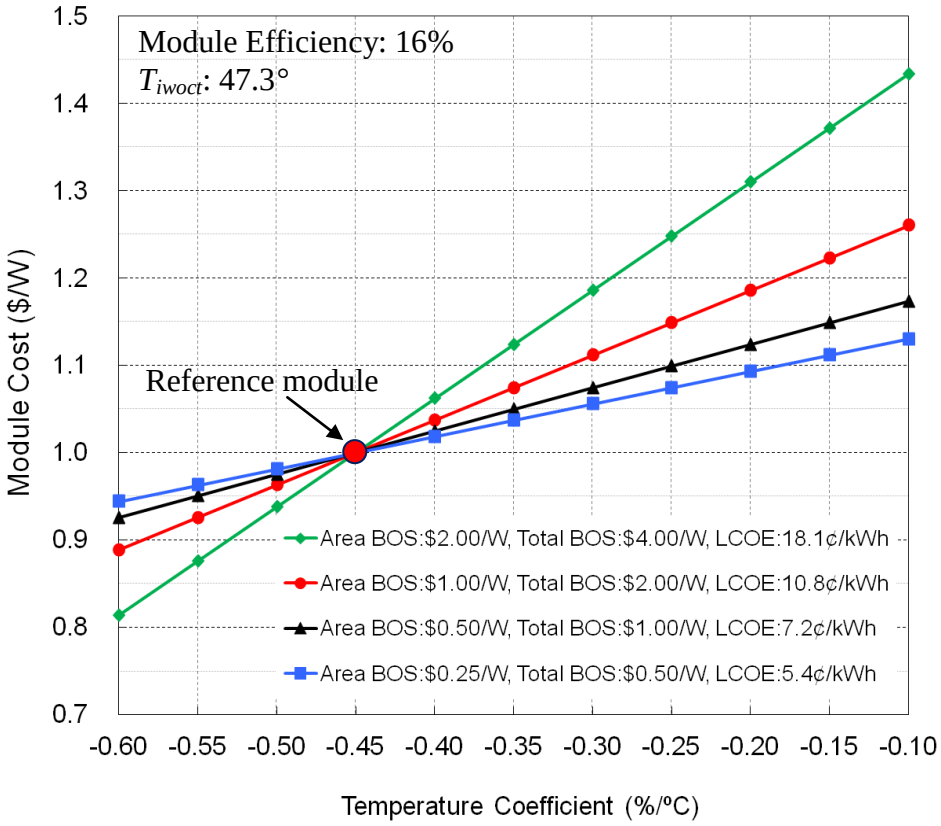

(a)

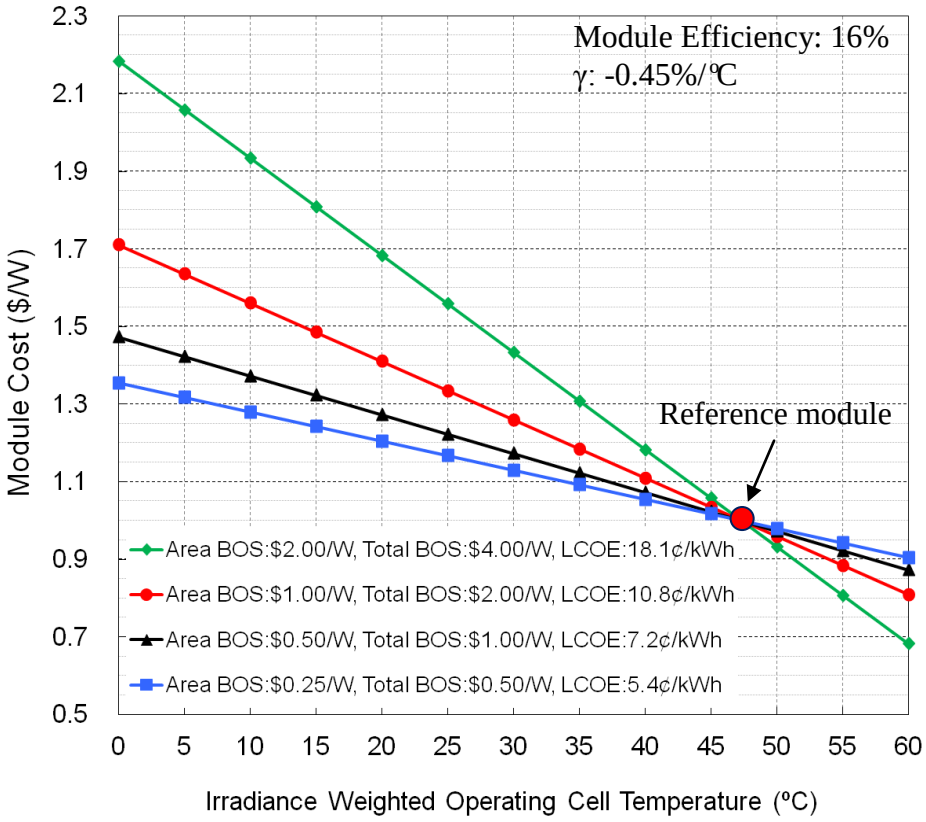

(b)

Figure 8.2: Module costs as a function of (a) temperature coefficient (γ) and (b) irradiance weighted operating cell temperature (T_{iwoct}) for various BOS costs with $1/W 16% efficient c-Si reference module (red circle). Each curve represents a constant LCOE. LCOE were calculated with an assumption of WACC = 7.7% without ITC in Phoenix.

In the above calculations, module efficiency was fixed at 16%. Generally γ varies with open circuit voltage and the bandgap of the absorber material. Therefore, an attempt is made to compare the four different promising and competing cell technologies today (c-Si, CdTe, CIGS, and a-Si) by using the model equations developed in this study in conjunction with the γ and T_{iwoct} values in Table 8.1. For these calculations, a 16% efficient c-Si module at $1/W with γ of -0.45%/℃ and T_{iwoct} of 47.3℃ (Phoenix) [47] was used as a reference. Different technologies were compared by calculating module cost that will lead to the same LCOE (Figure 8.3). These calculations are performed to

help consumers decide which technology to use in their region which is often a difficult decision due to a large number of variables. These results are plotted in Figures 8.3(a)–(d). Each figure corresponds to a certain BOS, which was varied in the range of $0.5–$4/W. Four technologies are compared for each BOS condition. It is also important to note that each curve in each figure ((a) to (d)) correspond to a fixed LCOE. Figure 8.3(c) shows that when area-related BOS cost is $1/W with total BOS cost of $2/W [8], a 12% CIGS module at $0.77/W, 12% CdTe module at $0.83/W, 9% a-Si module at $0.42/W, and 16% c-Si module at $1/W are equivalent and provide the same LCOE (Table 8.3) in Phoenix. Note that this price difference includes both efficiency and temperature coefficient effects. For example, Figure 8.3(c) shows that for a BOS of $2/W, without the temperature coefficient effect, a 12% CdTe module should cost $0.67/W to be equivalent to 16% c-Si module at $1/W. However, lower temperature coefficient allows the same size (kW) CdTe system more energy, therefore, CdTe module cost can be raised to $0.83/W, which is still below $1/w c-Si module. Figure 8.3 shows the comparison of four technologies for four different BOS conditions ranging from $0.5–4/W in the Phoenix area where the temperature coefficient plays a big role due to high temperatures. However, the equivalent module cost could change appreciably in a colder climate like Boston. This is the subject of next section.

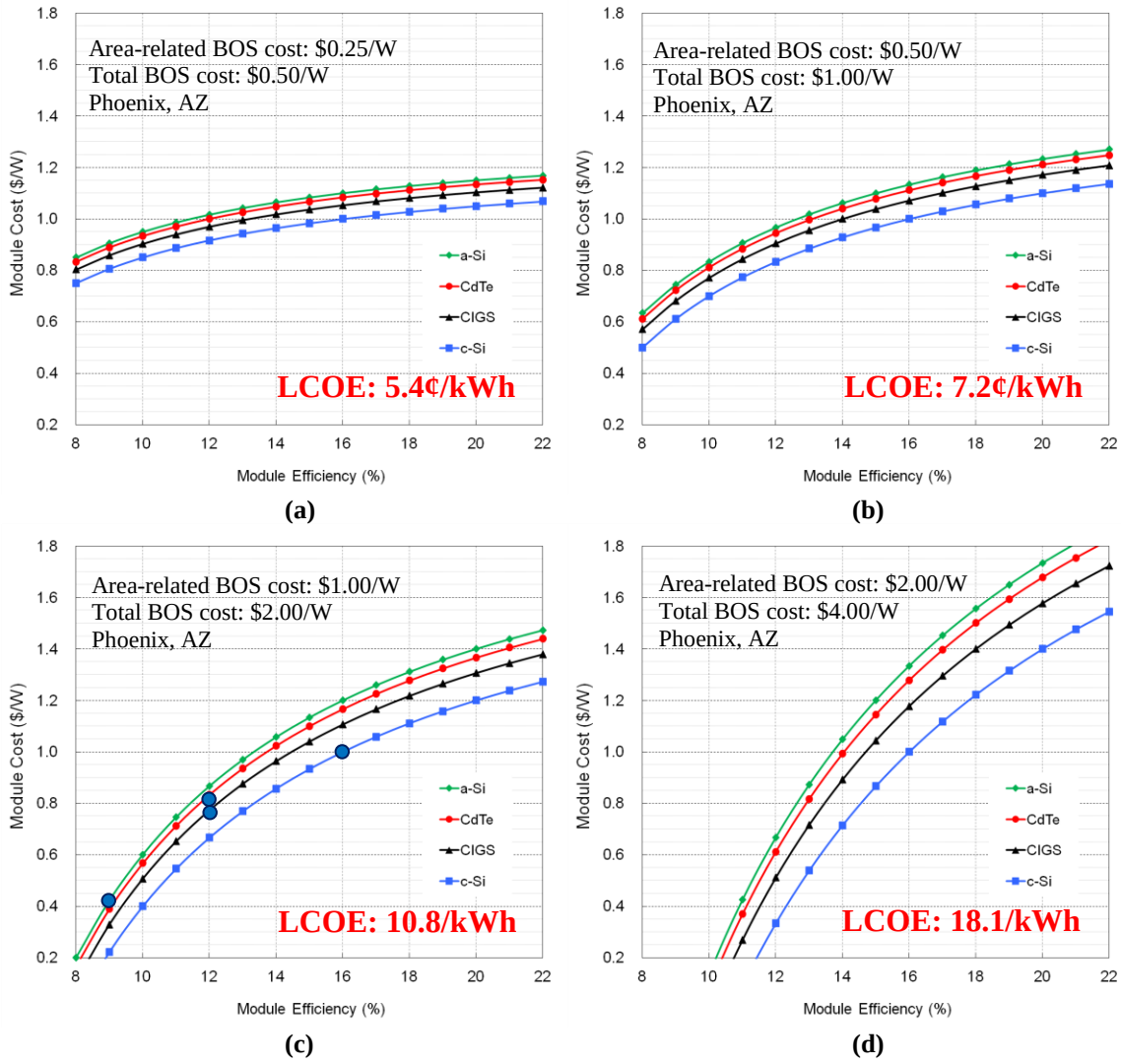

Figure 8.3: Module costs for four promising material modules as a function of module efficiency and BOS cost. T_{iwoct} of c-Si module was 47.3°C, and CdTe, CIGS, and a-Si was 45.1°C which is equivalent to when module is in Phoenix. LCOE were calculated with an assumption of WACC = 7.7% without ITC in Phoenix.

Table 8.3: Calculated module costs for various BOS costs at Phoenix. $1/W 16% c-Si module ($T_{iwoct}$ = 47.3°C) was used as reference. Each row provides same LCOE.

Module cost ($/W)	16% c-Si	12% CdTe	12% CIGS	9% a-Si
C_{Area}: $2/W, C_{BOS}: $4/W	1	0.61	0.51	-0.22
C_{Area}: $1/W, C_{BOS}: $2/W	1	0.83	0.77	0.42
C_{Area}: $0.5/W, C_{BOS}: $1/W	1	0.94	0.90	0.74
C_{Area}: $0.25/W, C_{BOS}: $0.5/W	1	1.00	0.97	0.91

8.2.3 Impact of geographical location and T_{iwoct} on equivalent cost of module

Change in geographical location generally involves change in solar irradiation and corresponding T_{iwoct}. For example, going from Phoenix, AZ to Boston, MA results in a decrease in average solar irradiation from 2256 to 1544 kWh/m^2/yr [83] and a decrease in T_{iwoct} from 47.3 to 27.3°C [47]. Lower solar irradiation hurts the LCOE, but lower T_{iwoct} increases energy production and reduces LCOE. Therefore, above calculation were repeated for the Boston area with reduced T_{iwoct} (Table 8.1) and irradiation. Figures 8.4(a)–(d) show the module cost vs. efficiency curves for C-Si, CIGS, CdTe, and a-Si modules that can provide same LCOE in Boston for four different BOS conditions. In contrast with Figure 8.3, all four curves in Figures 8.4(a) to (d) tend to merge, indicating that the premium due to lower γ for thin film modules shrinks in lower T_{iwoct} region like Boston. For example, Figure 8.3(c) showed that for $1/W area-related BOS cost, 12% efficient CdTe module should be sold at $0.83/W to compete with 16% Si reference module at $1/W in Phoenix. However, Figure 8.4(c) shows that CdTe module price need to drop to $0.70/W in Boston (Figure 8.4) because γ and T_{iwoct} premiums shrink significantly in colder climate. Thus, geographical location may play a significant role in dictating the premium for temperature coefficient. Calculated equivalent module cost for four different technologies is summarized quantitatively in Table 8.4 for four different BOS values in Boston area.

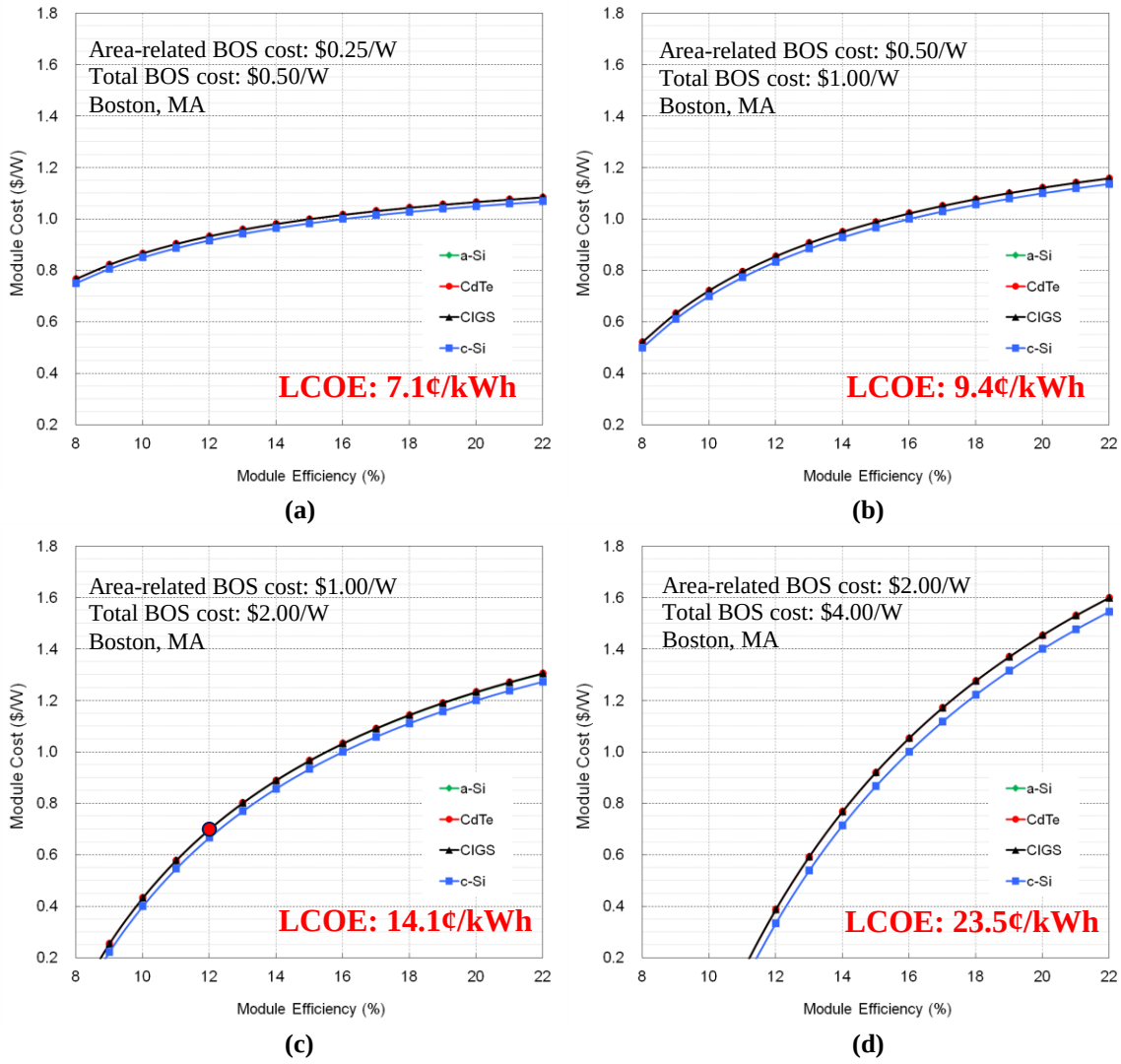

Figure 8.4: Module costs for four promising material modules as a function of module efficiency and BOS cost. T_{iwoct} of c-Si module was 27.3°C, and CdTe, CIGS, and a-Si was 24.9°C which is equivalent to when module is in Boston. LCOE were calculated with an assumption of WACC = 7.7% without ITC in Boston.

Table 8.4: Calculated module costs for various BOS costs at Boston. $1/W 16% c-Si module ($T_{iwoct}$ = 27.3°C) was used as reference. Each row provides same LCOE.

Module cost ($/W)	16% c-Si	12% CdTe	12% CIGS	9% a-Si
C_{Area}: $2/W, C_{BOS}: $4/W	1	0.39	0.39	-0.50
C_{Area}: $1/W, C_{BOS}: $2/W	1	0.70	0.70	0.25
C_{Area}: $0.5/W, C_{BOS}: $1/W	1	0.85	0.85	0.63
C_{Area}: $0.25/W, C_{BOS}: $0.5/W	1	0.93	0.93	0.82

Thus, the simple analytical model and equations developed in this chapter can quickly quantify equivalent module cost using a simple spread sheet model, without running extensive modeling program like System Advisor Model (SAM) [45] to compare various modules with varying γ, T_{iwoct}, efficiency, and cost in different geographical locations with varying BOS cost. In order to verify the analytical model and methodology, these results were validated by SAM calculations which gave the same LCOE when the calculated equivalent module cost, for a given BOS, from this study was fed into SAM along with the module efficiency, γ, and T_{iwoct} for the four technologies.

8.3 Conclusion

Analytical equations were developed and used to quantify the equivalent module cost and the associated premium for module efficiency, γ, and T_{iwoct}. The analytical equations can be easily programmed in an excel spread sheet to provide quick and accurate assessment of a new module cost, for a given BOS, that can lead to same LCOE as the reference module. Application of these analytical equations is shown by first calculating module cost for the same technology but different efficiency (fixed γ and T_{iwoct}) and then extending it to different materials and technologies (c-Si and thin films). For example, it is shown that $1/W 16% efficient c-Si module is equivalent to $0.86/W 14% efficient or $1.11/W 18% efficient c-Si module, resulting in same installed system cost and LCOE for $2/W BOS. In addition, it is shown that for a BOS of $2/W in a hot climate like Phoenix, a $1/W 16% c-Si module is also equivalent to $0.83/W 12% CdTe, $0.77/W 12% CIGS, and $0.42/W 9% a-Si module again resulting in same LCOE. Finally, it is shown quantitatively that the benefit of lower temperature coefficient of thin films is

significantly reduced in lower temperature climate. For example, for a $2/W BOS, the price of a 12% CdTe module needs to drop to $0.70/W in Boston area compared to $0.83/W in Phoenix area to be competitive with a 16% efficient $1/W c-Si module.

CHAPTER 9

QUANTITATIVE IMPACT OF KEY SYSTEM PARAMETERS ON THE LEVELIZED COST OF ELECTRICITY

Levelized cost of electricity (LCOE) is the most important parameter to assess the cost effectiveness of a photovoltaics (PV) system. Ultimate goal of PV is to attain LCOE equal to or lower than the current market price of electricity in a given location (grid parity). Correct value of LCOE is dependent on the accuracy of multiple inputs which makes it challenging to assess its exact value. Therefore, in this chapter, an attempt has been made to provide a deeper insight into the economics of PV by quantifying the sensitivity and impact of key parameters on LCOE including system installation cost, solar insolation, system lifetime, system derate losses, module cost, module efficiency, balance of system (BOS) cost, inflation, discount rate, and loan rate. Current realistic parameters were used as input to establish the starting point (Table 9.1), and then selected key parameters were varied to assess their impact on LCOE. System Advisor Model (SAM) program from National Renewable Energy Laboratory (NREL) was used for LCOE calculations. Contour plots are generated in this chapter to help in rapid assessment of LCOE for a situation different from the starting point. Contour plots provide excellent guidelines for focusing on most important parameters and selecting the best combination of system and financial parameters that can lead to a desired LCOE value in a given location. Finally, model calculations are extended to quantify the required installed system cost in different regions of the US and the world to attain grid parity.

9.1 Levelized cost of electricity from a PV system

LCOE is defined as cost per unit energy produced over the entire life of a system. Therefore, correct LCOE requires accurate assessment of money spent and energy produced during the system lifetime. Money spent over system lifetime consists of installed system cost, its financing, and annual operation and maintenance (O&M) costs [48]. Installed system cost consist of module and BOS costs, and the BOS cost is composed of wiring and mounting hardware, installation labor, inverter, permitting, commissioning, engineering, design, site preparation, grid connection, management, sales tax, installer margin, overhead, insurance, etc [6, 8]. Wiring and mounting hardware and installation labor are referred to as an area-related BOS cost because they depend on system area or the number of modules. The sum of other costs including inverter, permitting, commissioning, engineering, design, site preparation, grid connection, management, sales tax, installer margin, overhead, and insurance is referred to as fixed or indirect BOS cost because it is independent of the number of modules [47].

Since accurate assessment of LCOE involves consideration of time value of money and power [47, 48, 50] which is affected by inflation and real or nominal discount rates. The net present value, which recalls future value into present value using nominal or real discount rate, is used in the LCOE calculation. Nominal discount rate for money and real discount rate for power gives real LCOE [45]. When nominal discount rate is used for both money and power, nominal LCOE is obtained. In this chapter, only the real LCOE was calculated for comparison. A detailed list of input parameters used as starting point for LCOE calculations in this study are summarized in Table 9.1 [6, 78]. These inputs are

closer to a commercial PV system today. For a residential or utility scale system, financial inputs may be little different.

Table 9.1: List of reference input parameters used for LCOE calculations.

Parameter	Unit	Value
Array size	kW	100
Operation and maintenance	$/yr	0.5% of total installed system cost
System derate losses	%	20
Availability	%	97
Temperature coefficient	%/℃	-0.45
Annual system power degradation	%	0.5
System lifetime	yr	30
Tracking		South-facing latitude tilt
Inflation	%	2.5
Nominal discount rate	%	10.7
Real discount rate	%	8
Federal/state tax	%	28/7
Net salvage value	%	0%
Loan term	yr	10
Loan rate	%	7
Debt fraction	%	50
WACC	%	7.7
Federal and state depreciation		5-yr MACRS
Investment tax credit and incentives	%	0

* Availability: Assuming 10 days system down per year for maintenance
* Real discount rate = (1+Nominal discount rate) / (1+Inflation) - 1
* WACC: Weight average cost of capital
  = Debt fraction×Loan rate×(1-Tax rate) + (1-Debt fraction)×Nominal discount rate
* MACRS: Modified accelerated cost recovery system

9.2 Effect of installed system cost and solar insolation on LCOE

Installed system cost and solar insolation are the two most important parameters that impact LCOE. This is because installed system cost ($/W) represents the total amount of money ($) used for PV system installation of a given size (W), and solar insolation dictates the total amount of energy produced by the PV modules. Model calculations were performed by varying the installed system cost in the range of $0.5–6/W and solar

insolation from 1300–2200 kWh/m^2/yr. This information was plotted in the form of user friendly LCOE contours to assess their impact. Figure 9.1 shows the LCOE contour plot depicting the combined impact of installed system cost and annual solar insolation (global horizontal) on the LCOE using the inputs shown in Table 9.1. Note that the LCOE contours range from 3–30¢/kWh for the range of solar insolation and installed system cost used in this study. This plot can readily provide the required installed system cost in these regions (insolation) to attain grid parity or any desired LCOE. The y-axis shows selected locations and corresponding solar insolations. These contours can be used to provide many useful guidelines. For example, Figure 9.1 shows that for the given system and financial inputs in Table 9.1, an installed system cost of $2.8/W, $2.3/W, and $1.9/W (marked as red circles) can lead to a LCOE of 10¢/kWh in Phoenix, Atlanta, and Detroit, respectively which is close to or lower than the current market price of electricity in those regions (9.2, 9.3, and 10.5¢/kWh) [9]. Since module and BOS costs have recently declined quite rapidly, a commercial or utility scale PV system can be installed today in many parts of the world at ≤ $3/W [7, 8, 84] which will bring Phoenix close to grid parity. Solar insolation in Detroit will require installed system cost to below $2/W. Contour plots in Figure 9.1 are very useful in predicting the change in LCOE in different regions as the installed cost declines. For example, it shows that if the Department of Energy (DOE) SunShot target of $1.25/W [6] is achieved for installed system cost, LCOE value in Phoenix, Atlanta, and Detroit will reach 4.5, 5.4, and 6.4¢/kWh, respectively. Notice that for a fixed LCOE contour, LCOE is proportional to the installed system cost. However, the slope of the LCOE contour becomes steeper as you move toward lower installed system cost. This means a same drop in installed system cost has

smaller effect on the absolute value of LCOE, but the relative change in LCOE remains same.

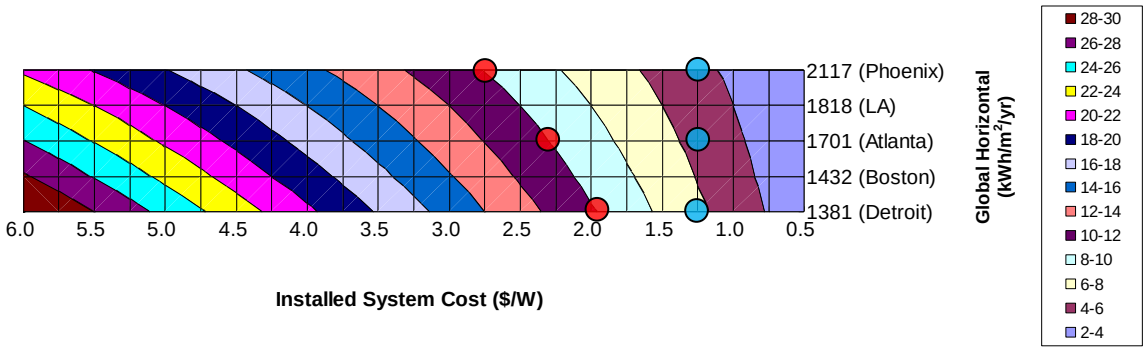

Figure 9.1: LCOE contour plot as a function of installed system cost and solar insolation.

9.3 Requirement for grid parity in the US and the world

The goal of PV is to attain grid parity in different parts of the world. Since price of electricity, solar insolation, and installed system cost can be different in different parts of the world, therefore, different region will attain grid parity at different price point of installed system cost. In order to provide this answer, above model calculations were extended to provide charts that show how low the installed system cost needs to be in different regions of the US (Figure 9.2(a)) and in different parts of the world (Figure 9.2(b)) to attain grid parity. In order to accomplish this, LCOE calculations (using the inputs in Table 9.1) were performed as a function of solar insolation and installed system cost and were super imposed on the current market price of commercial electricity in different parts of the US and the world in 2012 [9]. These plots show the required installed system cost in different regions to attain grid parity.

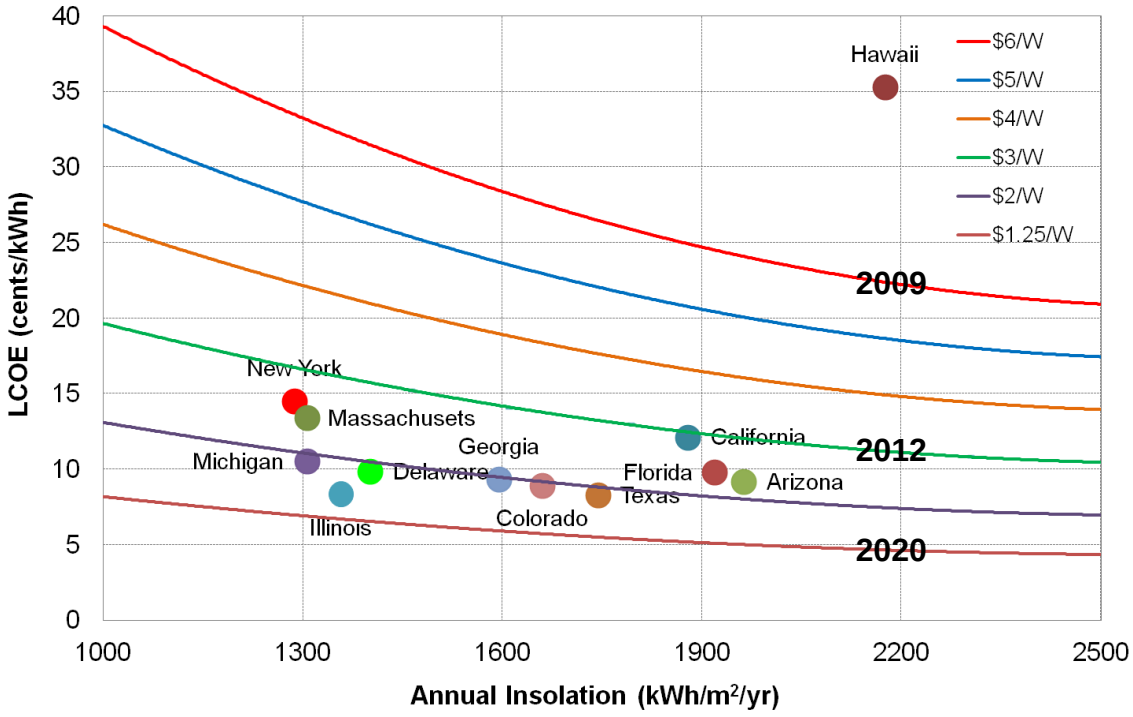

(a)

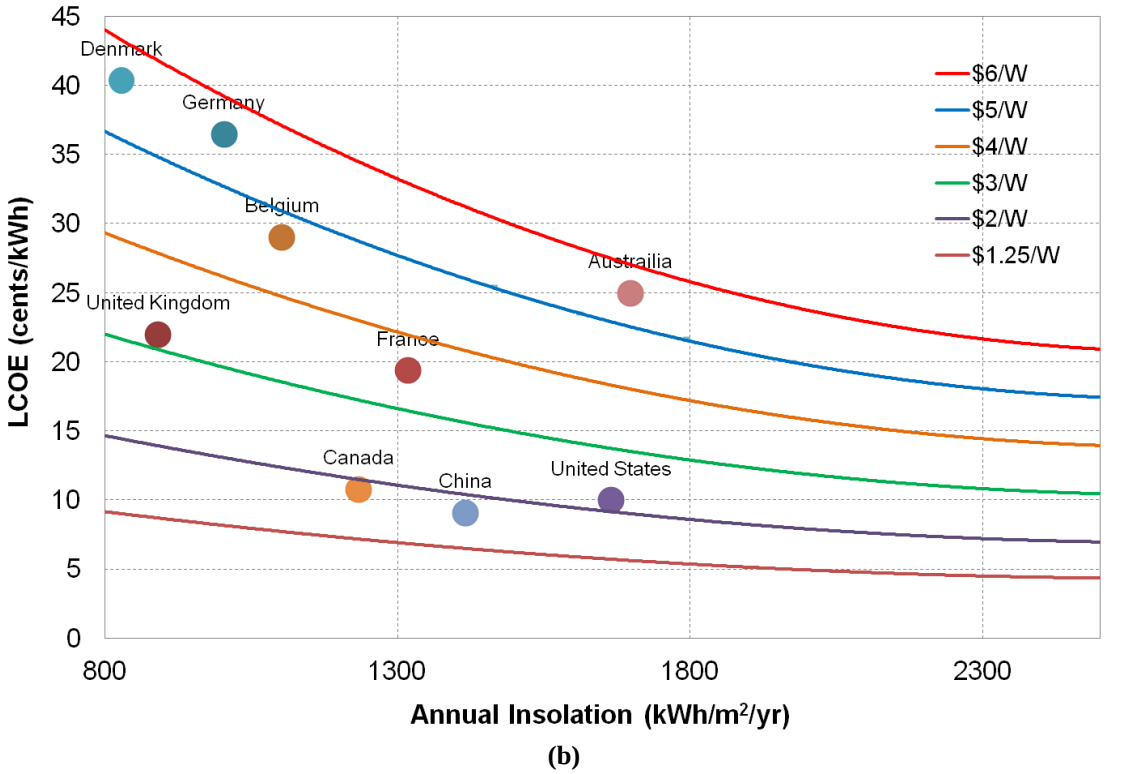

(b)

Figure 9.2: LCOE plot as a function of installed system cost and solar insolation with current market price of electricity (a) of the US and (b) the world.

For example, Figure 9.2 indicates that in the US, installed system cost needs to be below $3/W to start encroaching grid parity in most regions except for Hawaii where PV is already below grid parity today because of the high price of electricity. To reach the grid parity in the entire US without incentives, installed system cost should be $1.25/W, which happens to be the goal of SunShot initiative by 2020. A similar plot is generated for the world which shows that some countries are already below grid parity for the inputs in Table 9.1, however, further decline in PV cost is needed for grid parity in other countries. The good news is that we are within the striking distance of grid parity for most countries.

9.4 Effect of system lifetime and loss mechanisms on LCOE

System lifetime and loss mechanisms (system derate losses) dictate the cumulative energy production from a PV system. System derate losses include wiring, mis-match, soiling (dust), shading, AC to DC (inverter), and DC to DC (transformer) losses [83]. In order to quantify these and transform the results into a user friendly contour plot, LCOE calculations were performed using the SAM model with system derate losses in the range of 5–50% and system lifetime from 10–50 years. Note, a typical number for system losses is ~20% and system lifetime is ~30 year for silicon modules. Figure 9.3 shows the contour plot of LCOE as a function of system lifetime and system derate losses for an installed system cost of $3/W in Atlanta, GA, which represents average solar insolation in the US. All other parameters are shown in Table 9.1.

Contour plot in Figure 9.3 conveys two important messages. First, it quantifies the impact of reduced system lifetime on LCOE. For example, a decrease in the system

lifetime from 30 to 20 year will increase the LCOE by 1.7¢/kWh (from 13 to 14.7¢/kWh) for a fixed system derate losses of 20%. Secondly, Figure 9.3 shows the magnitude of increase in LCOE from higher derate losses. For example, an increase in system derate losses from 20 to 30% will increase LCOE by 1.8¢/kWh (from 13 to 14.8¢/kWh) for a 30 year system lifetime. Similarly, for a 20 year life and 30% system derate, LCOE will increase by 1.9¢/kWh to 16.6¢/kWh. It is interesting to note that since the absolute LCOE value is proportional to the installed system cost, so one can transform these numbers from a \$3/W to a \$1/W system by multiplying by factor of 1/3. For example, if the installed system cost was \$1/W, then a decrease in system life from 30 to 20 years would increase the LCOE by 1.7/3 or 0.57¢/kWh. This shows the value and versatility of the contour plots.

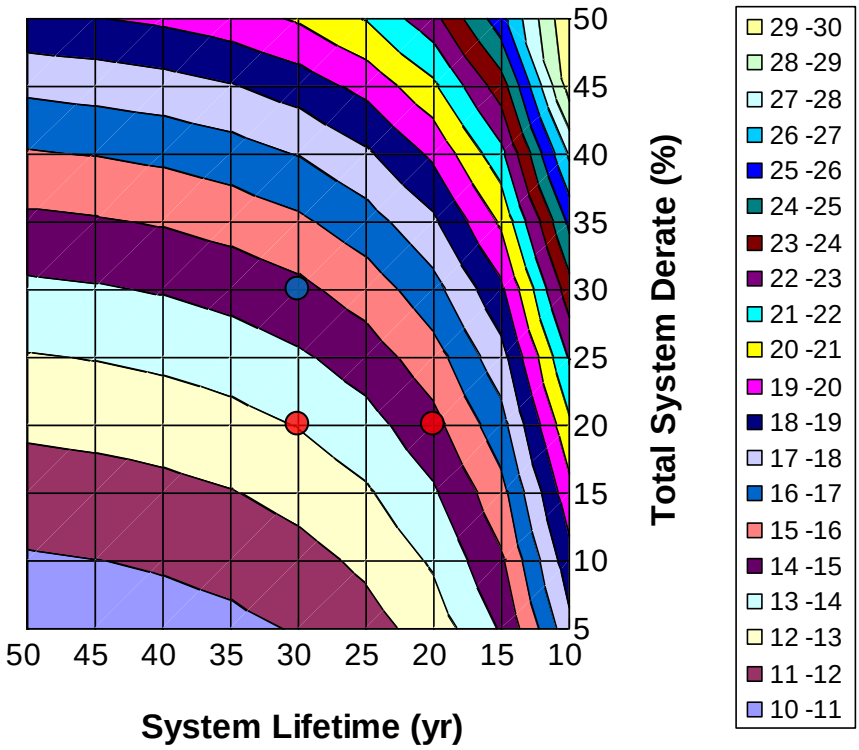

Figure 9.3: LCOE contour plot for Atlanta area as a function of system lifetime and system derate losses for installed system cost of \$3/W.

9.5 Impact of module cost and module efficiency on LCOE

Module efficiency influences LCOE because it dictates for how much solar energy is converted into electricity. Higher efficiency module is desirable because it produces more power per unit area, so a fewer modules are required for a fixed size (kW) system. This reduces wiring and mounting hardware and installation labor cost (area-related BOS cost) resulting in a decrease in BOS cost and LCOE [47]. In order to assess their impact quantitatively, again user friendly contour plots were generated by varying module efficiency from 6–24% and module cost from $0–2.4/W. Model calculations were performed using the SAM model, and LCOE contours were plotted as a function of module cost and efficiency. Figure 9.4 shows the change in LCOE as a function of module cost and module efficiency in the Atlanta area. Figure 9.4 shows that using the inputs in Table 9.1, $1/W 16% efficient PV modules [6] can provide LCOE of 13.0¢/kWh for an area-related BOS cost of $0.80/W and fixed BOS cost of $1.20/W [6, 78]. If the cost of 16% efficiency module reduces from $1/W to $0.25/W without the change in efficiency, the LCOE will decrease from 13.0 to 10.0¢/kWh. Figure 9.4 also provides information about efficiency premium, which is defined as allowed increase in price of higher efficiency module to offset the BOS cost reduction, resulting in same LCOE. For example, using the inputs in Table 9.1, an LCOE of 10¢/kWh can be achieved in Atlanta with 20, 16, and 12% efficient modules at a cost of 0.43, 0.25, and $0/W, respectively, as indicated by red circles in the Figure 9.4. This implies that a 20% efficient module can be sold at a premium of +18¢/W while a 12% module must sell a premium of -25¢/W. It also reveals that even if a 12% efficient silicon module is free (zero cost), it cannot reach 10¢/kWh in Atlanta because the BOS cost associated with a

12% module alone results in 10¢/kWh. Thus, the user friendly contour plots can provide great insight and useful information. It is important to note that the above contour plot is quite sensitive to the BOS cost assumptions, therefore, in the next section LCOE contours for various BOS costs are plotted.

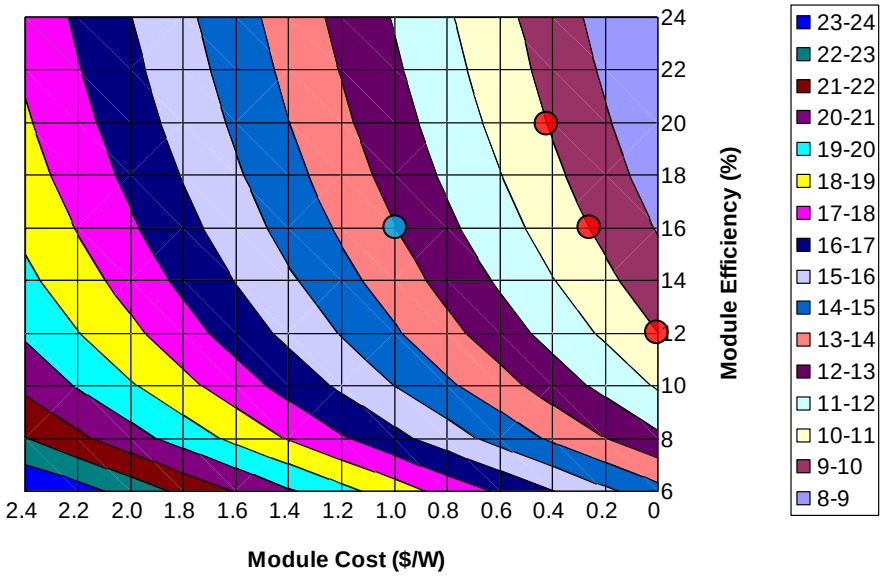

Figure 9.4: LCOE contour plot for Atlanta area as a function of module cost and module efficiency with area-related BOS cost of $0.80/W and fixed BOS cost of $1.20/W for a 16% efficient reference module.

9.6 Impact of BOS cost on LCOE

Module cost and efficiency is relatively independent of region, but the BOS cost today varies significantly around the globe because of the difference in policies and labor cost etc. Since module efficiency alters the BOS which in turn affects the LCOE, therefore, relationship between module cost and efficiency for different BOS costs is investigated. This is done by plotting the LCOE contours for varying BOS costs ranging from $1–6/W. For these calculations, area-related and fixed BOS costs were assumed to be equal. As

expected, Figure 9.5 shows that the BOS cost has a huge impact on the absolute value of LCOE. For example, contour plots in Figure 9.5 show that $1/W 16% efficient module in combination with a BOS cost of 6, 4, 2, and $1/W produces electricity at 30.4, 21.7, 13.0, and 8.7¢/kWh (red circles), respectively.

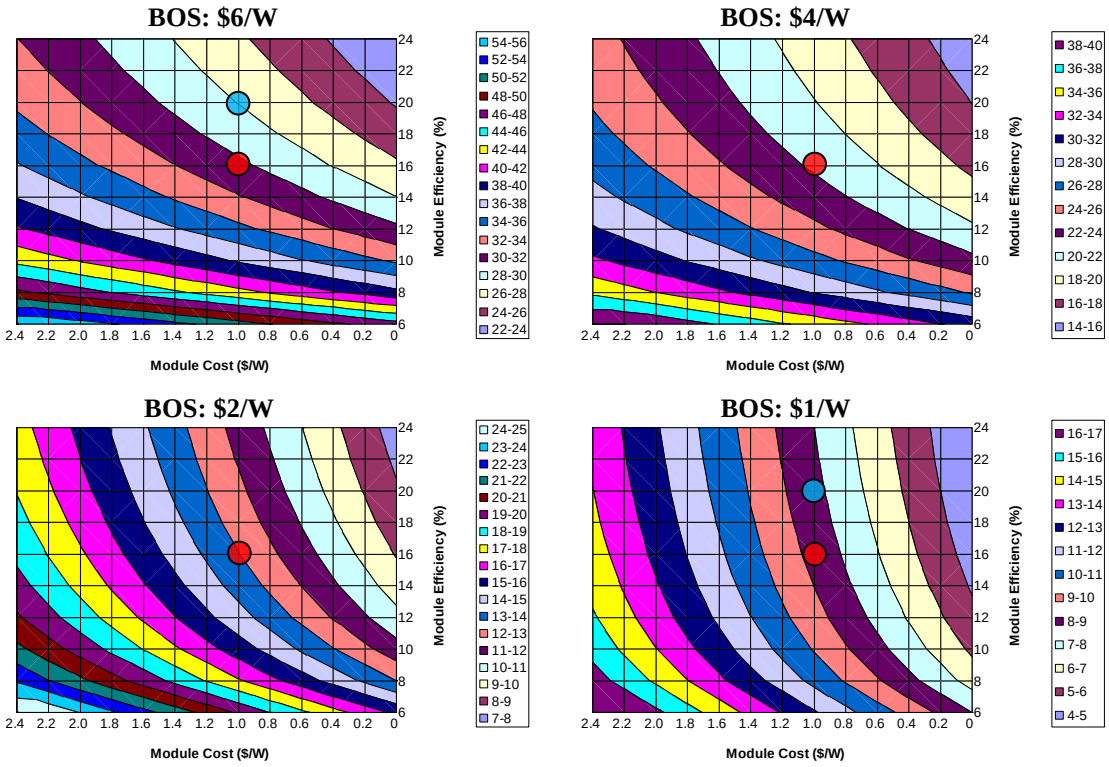

Figure 9.5: LCOE contour plot for Atlanta area as a function of module cost and module efficiency for different BOS cost ranging from 6 to $1/W.

Notice that as the area-related BOS cost decreases, the LCOE contours become steeper. This is because impact of module efficiency enhancement on absolute value of LCOE decreases. This is because efficiency premium shrinks with the decrease in variable BOS cost (Chapter 8), so the slope of contours becomes steeper. For example, Figures 9.5(a) and (d) show that if the module efficiency increases from 16 to 20% without the increase in module cost ($1/W), the LCOE decreases by 2.5¢/kWh for a $6/W BOS but only by

0.4¢/kWh for a BOS of $1/W (blue circles). Even though the absolute change in LCOE shrinks with BOS, relative change remains significant.

9.7 Impact of inflation and real discount rate on LCOE

Financial parameters also have a significant impact on LCOE. Accurate assessment of LCOE involves consideration of time value of money and power which is strongly influenced by inflation and discount rate [48]. Net present value, which translates future value into present value via nominal or real discount rate, is used in the LCOE calculations [47]. Nominal discount rate accounts for opportunity cost of money or the money that could be earned from the cash if it is invested and not used for buying PV. Real discount rate is inflation adjusted nominal discount rate [48]. These numbers also vary significantly around the globe. A 2.5% inflation [85] with 8% real discount rate represents the situation in the US while some developing countries have much higher inflation rate than the US. In addition, a bad economy can decrease the discount rate. Figure 9.6 shows quantitatively that higher inflation rate and lower discount rate tend to reduce LCOE. In Figure 9.6, LCOE contours are plotted as a function of inflation and real discount rate. Increase in inflation rate from 2 to 4% lowers LCOE by 0.4¢/kWh when real discount rate is 8%. Likewise, decrease in real discount rate from 8 to 6% lowers LCOE by 1.8¢/kWh when inflation rate is 2%.

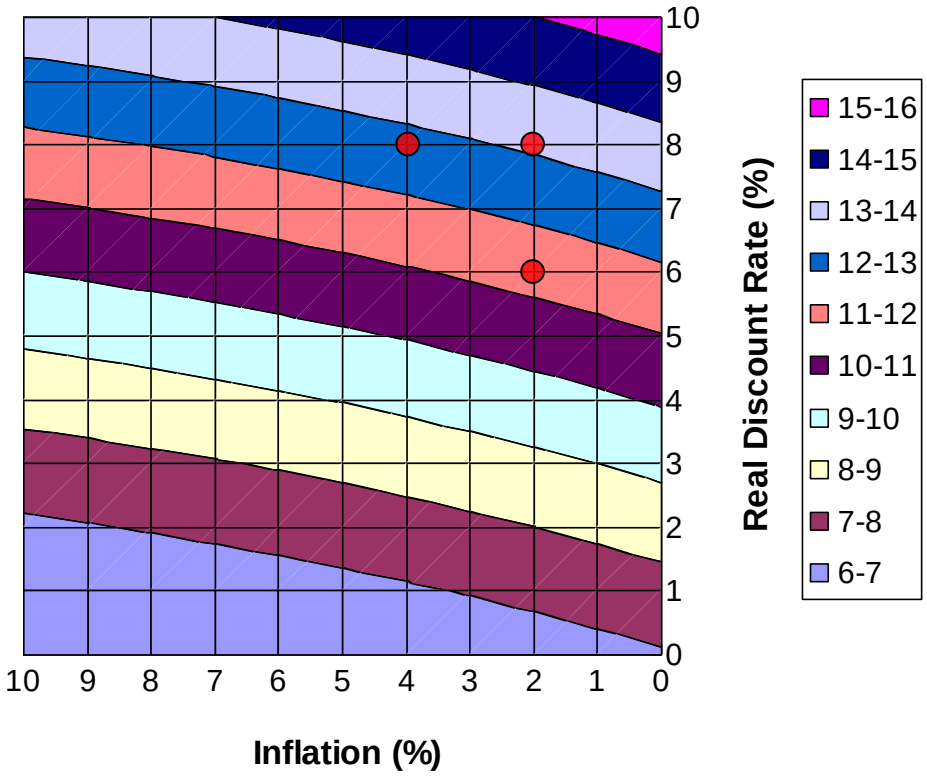

Figure 9.6: LCOE contour plot for Atlanta area as a function of inflation rate and real discount rate for installed system cost of $3/W.

9.8 LCOE as a function of debt fraction and loan rate

Since LCOE is cost per unit energy produced, financing and borrowing terms can significantly alter LCOE. Down payment and interest rate are two key financial parameters. Higher down payment reduces mortgage payment but also lowers the opportunity to make money if the down payment was invested elsewhere. Opportunity cost is calculated from discount rate. Therefore, as loan rate decreases or debt fraction increases, LCOE decreases. Figure 9.7 shows the LCOE contour plots as a function of debt fraction (1- down payment) and loan rate for a $3/W system using the input parameters from Table 9.1 in the Atlanta area. Figure 9.7 shows that a decrease in the loan rate from 7 to 5% lowers LCOE by 0.5¢/kWh for a 50% down payment. Likewise,

increase in debt fraction from 50 to 100% lowers LCOE by 2.4¢/kWh for a fixed loan rate of 7%. This is because you can make more money by investing the down payment since the discount rate (opportunity cost) of 8% is higher than the loan rate of 7%.

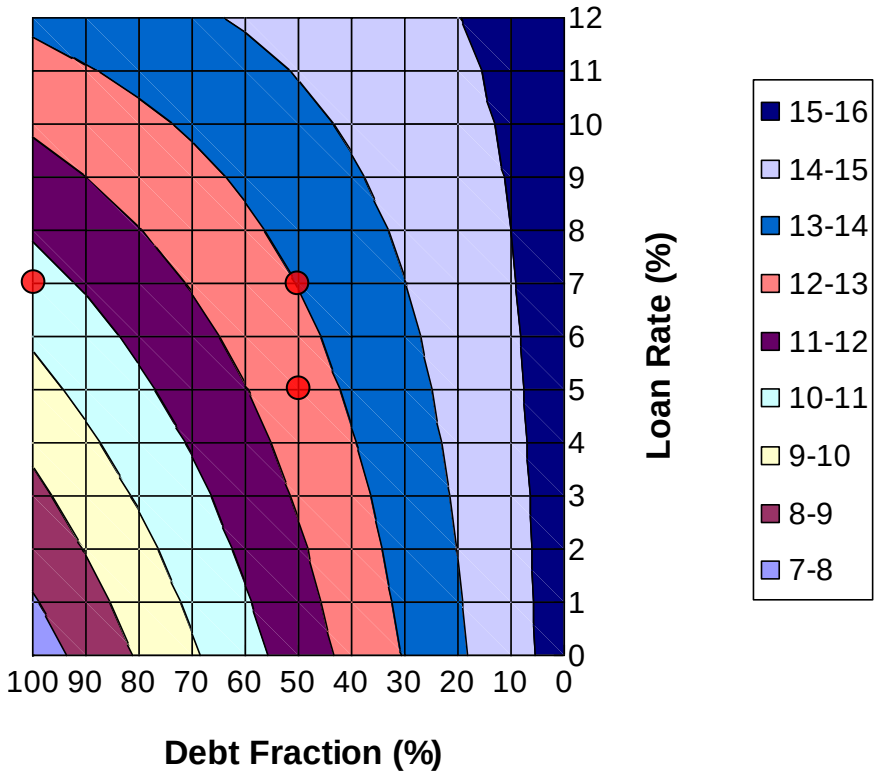

Figure 9.7: LCOE contour plot for Atlanta area as a function of debt fraction and loan rate for installed system cost of $3/W.

9.9 A roadmap to LCOE of 6¢/kWh

After establishing the impact of all key system parameters individually on LCOE, this section uses the guidelines from the previous sections to establish a roadmap to attain grid parity at ~6¢/kWh. Using the input parameters in Table 9.1, Figure 9.8 starts with an installed system cost of $3/W and LCOE of 13.0¢/kWh in Atlanta which is close to the current situation. If the system lifetime is increased from 30 to 35 years, and system

derate losses are reduced from 20 to 15%, LCOE will decrease by 0.3¢/kWh and 0.7¢/kWh, respectively, resulting in an LCOE of 12.0¢/kWh. Now, if the BOS cost can be decreased by $1.0/W, it will lower the installed system cost from $3/W to $2/W and the LCOE will drop to 8¢/kWh. At this point, if the loan rate is reduced from 7 to 5%, LCOE will decrease to 7.7¢/kWh. Finally, if we increase the debt fraction from 50 to 100%, LCOE will decrease by additional 1.8¢/kWh, attaining a value of 5.9¢/kWh. Figure 9.1 shows that LCOE of 5.9¢/kWh can also be achieved simply by lowering the installed system cost to $1.36/W while keeping all other parameters same. This will require some combination of module and BOS cost reduction.

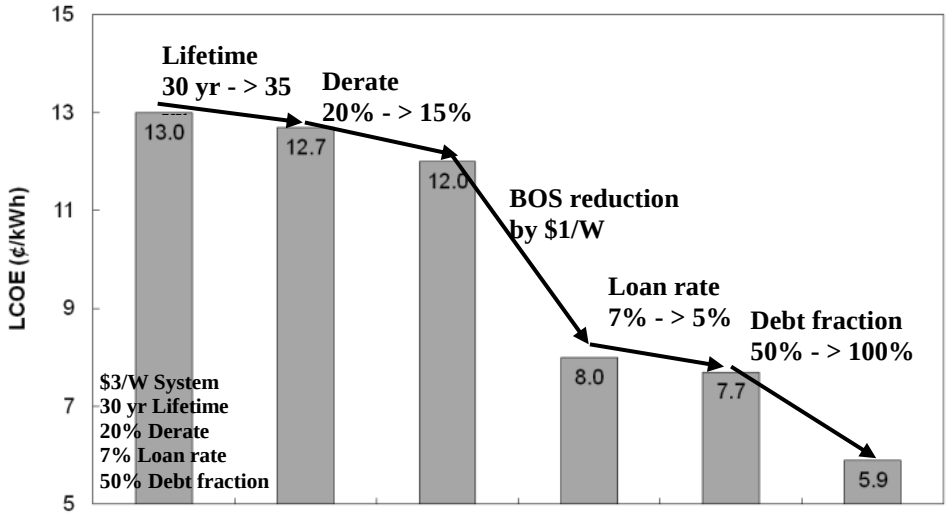

Figure 9.8: A roadmap toward LCOE of 6¢/kWh.

9.10 Conclusion

Quantitative analysis of LCOE from PV is conducted in detail. The impact of key parameters such as installed system cost, solar insolation, system lifetime, system derate losses, module cost, module efficiency, BOS cost, inflation, discount rate, and loan rate

on LCOE is quantified using the SAM program. Study is conducted using the best available system and financial parameters today (2012). Calculations are performed to provide guidelines to attain the 2020 DOE SunShot goal of 6¢/kWh. The impact of key parameters is plotted in the form of contour plots. Generated contour plots show the impact of technology, loss mechanism, and financing on LCOE and can also be used to define roadmaps for grid parity.

CHAPTER 10

CONCLUSIONS AND FUTURE WORK

The goal of this thesis is to develop low-cost high-efficiency crystalline silicon (Si) solar cells which are at the right intersection of cost and performance to make photovoltaics (PV) affordable. The goal was addressed by improving the optical and electrical performance of Si solar cells through process optimization, device modeling, clever cell design, fundamental understanding, and minimization of loss mechanisms. To define the right intersection of cost and performance, analytical models to assess the premium or value associated with efficiency, temperature coefficient, balance of system (BOS) cost, and solar insolation were developed, and detailed cost analysis was performed to quantify the impact of key system and financial parameters in the levelized cost of electricity (LCOE) from PV.

In the first task of this thesis, a SiC_xN_y based antireflection (AR) coating and passivation film was deposited from a silane-free source in an effort to reduce cost and enhance performance of Si solar cells. A detailed characterization and analysis of this film was performed along with its impact on emitter saturation current density (J_{oe}) and the Si solar cell performance. Lower J_{oe} value gives higher cell efficiency. It was found that SiC_xN_y based films provide refractive index in the rage of 1.9–2.0. In addition, high surface charge density and hydrogen concentration of SiC_xN_y films provided comparable surface passivation and J_{oe} values on a 45 Ω/sq emitter cells. However, J_{oe} values were found to be slightly higher on high performance 80 Ω/sq emitter, resulting in 11 mV loss in open circuit voltage (V_{oc}) and ~0.2% loss in cell efficiency. Although there is a small

tradeoff in efficiency at high end, the solid polymer source for SiC_xN_y deposition provides considerable safety and cost benefits compared to SiN_x films grown by silane gas.

Second task involves the investigation of bulk lifetime and efficiency degradation under illumination in boron-doped Czochralski (Cz) solar cells coated with conventional SiN_x and SiC_xN_y AR coatings. This light-induced degradation (LID) phenomenon is well known and is attributed to the formation of boron (B) and oxygen (O) complexes under illumination which lead to factor of 2–5 reduction in bulk lifetime and 0.2–0.6% loss in absolute cell efficiency. Limited data in the literature shows that carbon (C) in Si may retard LID because C likes to form complexes with oxygen which may reduce the concentration of B-O complexes. Therefore, possible injection of C from the SiC_xN_y AR coating into the bulk Si was examined during high temperature deposition and contact firing. Indeed SiC_xN_y-coated p-type Cz solar cells showed a slight lower light-induced efficiency degradation (0.1%) compared to the conventional SiN_x-coated solar cells (0.3%), which have no source of additional carbon.

Third task dealt with the investigation of possible improved performance of SiC_xN_y AR-coated solar cells under low illumination due to the observed higher shunt resistance (R_{sh}). Theoretical calculations were performed to demonstrate how and why R_{sh} value < 30 Ω can reduce the cell efficiency at lower insolation. It was found that cells coated with carbon-containing SiC_xN_y film have much higher R_{sh} value after contact firing compared to the carbon-free SiN_x film. R_{sh} of SiC_xN_y-coated 239 cm^2 cells was found to be generally above 60 Ω compared to the SiN_x-coated cells, which averaged around 23 Ω. Model calculations and detailed cell analysis revealed that better low-light performance

of SiC_xN_y-coated cells. This makes up for the slightly lower starting efficiency of SiC_xN_y-coated cells compared to the SiN_x-coated cells.

Fourth task in this thesis involved optimization of refractive index (n) and thickness of the conventional SiN_x based AR coating to provide best performance under a glass module. The performance of various SiN_x films was investigated by a combination of geometrical ray tracing simulation program Sunrays and widely used PC1D device modeling program. Simulations showed that SiN_x film with n = 2.03 and thickness of 78 nm provides the highest cell efficiency under glass/EVA (ethylene vinyl acetate) encapsulation for the pyramid textured Si solar cells, even though index of 2.4 has the best match with glass (n = 1.5). This is because a cell coated with an index of 2.4 SiN_x has a much lower starting efficiency in air due to the absorption. Identical optical analysis for planar cells shows that the n = 2.20 and thickness of 68 nm gives the highest encapsulated cell efficiency.

Fifth task in this thesis involved passivation of Si surface with Al_2O_3 films grown by atomic layer deposition (ALD). Lower surface recombination velocity (SRV) is highly desirable for better cell performance. Deposition and annealing conditions for ALD Al_2O_3 films on Si were investigated for achieving stable and high-quality passivation for commercial ready solar cells. Recently, it has been reported that ALD Al_2O_3 can provide excellent passivation on p-type Si surface due to high negative charge, which creates an accumulation layer at the p-type Si surface to reduce recombination. This task shows that plasma-assisted ALD Al_2O_3 provides excellent passivation after optimized deposition, annealing, and firing. It gave SRV of 57 cm/s after annealing and 150 cm/s after firing cycle on a textured Cz wafer which is quite superior to the SiO_2 film. Commercial-ready

screen-printed n^+-p Cz solar cells with textured back were fabricated with plasma-assisted ALD Al_2O_3 coating on p-surface and compared with SiO_2 passivated solar cells. All these cells had local aluminum-back-surface field. About 0.9% absolute efficiency gain was observed for textured n^+-p cells with using plasma-assisted ALD Al_2O_3 compared to textured back SiO_2 passivated cells. Such dielectric passivated p-type cells are generally fabricated with planar backs for higher efficiency where the absolute efficiencies is much higher and the gap between Al_2O_3 and SiO_2 passivated cells is much smaller. In the case of p^+-n-n^+ n-base cells, textured p^+ emitter was passivated with both Al_2O_3 and SiO_2, and the Al_2O_3passivated cells showed ~0.3% higher efficiency with maximum approaching 20%.

To define the right intersection of cost and performance of PV cells to attain grid parity, various cost models were developed and used to assess the economical impact of cell efficiency enhancement on module cost and LCOE. Higher-efficiency modules not only produce more power, but they also reduce the BOS cost because some BOS components decrease as module efficiency increases. In addition, it is also important to know how much more one should pay for higher-efficiency modules. For example, methodology and calculations used in this study showed that a $1/W 16% efficient Si module is equivalent to a $0.86/W 14% efficient module as well as $1.11/W 18% efficient Si module because all three result in same installed system cost and LCOE because of the difference in BOS cost due to module efficiency.

LCOE is the most important parameter to assess the cost effectiveness of a PV system. Ultimate goal of PV is to attain LCOE equal to or lower than the current market price of electricity in a given location (grid parity). Correct value of LCOE is dependent on the

accuracy of multiple inputs which makes it challenging to assess the precise value. Extensive PV system modeling was conducted in this research to quantify the sensitivity and impact of several key system parameters such as installed system cost, BOS cost, module efficiency, operating performance loss, module cost, and system lifetime as well as financial parameters such as loan fraction, interest rate, and depreciation etc. Calculations showed that to reach the grid parity in the entire US without incentives, installed system cost should be $1.25/W, which also happens to be the goal of SunShot initiative by 2020.

This thesis addressed several technology development and process optimization for tasks to enable low-cost high-efficiency Si solar cells that can lead to grid parity. It is shown that grid parity in the entire world can be achieved when the installed PV system cost reaches below $1.25/W (module-cost of $0.5/W + BOS cost of $0.75/W). Today, the installed system cost ranges from $2.5–5/W. Therefore, further cost reduction is necessary by a combination of reduced module and BOS cost and module efficiency enhancement.

Future work may involve use of emerging Si materials like mono-cast or continuous melt replenishment of Cz. In addition, technologies for kerfless thin wafers need to be developed. Market share of n-type Cz will also grow because of the potential for higher bulk lifetime and efficiency. However, technologies for boron emitter formation and its passivation via Al_2O_3 dielectrics need to be investigated. In addition, technologies for reduced reflection and shadow losses need to be developed at low cost. Finally, a lot needs to be done in the area of raising module efficiency > 20% and lowering the BOS cost below $1/W.

APPENDIX A:

MODELING & ANALYSIS OF THE GEORGIA TECH CLOUGH COMMONS PV SYSTEM

Georgia tech installed an 86.4 kW photovoltaics (PV) system on the roof of Clough Commons at 2011. System consists with 360 × 240 W crystalline-Si panels (Suniva, Inc.) and 12 × 7200 kW inverters (Sunny Boy 6000US) to convert DC current to AC current. Panels are tilted at 15° facing south. Installed system cost was $4.18/W including tax, installer margins, and module cost of $2.05/W.

Figure A.1: Pictures of 86.4 kW PV system on Clough Commons.

Energy produced from this PV system was tracked for the whole year (Sep. 2011 ~ Aug. 2012) and compared with simulated result from System Advisor Model (SAM) (Figure A.2). Actual energy produced matches well with the simulated power output assuming 20% total system derate and 10 down days per year. Simulations showed that 86.4 kW PV system in Atlanta, GA (annual solar insolation of 1821 kWh/m^2) with 15° tilt produced 123 MWh electricity in the first year. More detailed simulated results are listed

in Table A.1. Using the financial assumptions of Table 9.1 (which is not how the Clough system was financed), LCOE from the Clough Commons PV system should be 19.52¢/kWh, which is a factor of two higher than the grid parity in Atlanta. More recently installed commercial system cost in Atlanta has declined to ≤ $3/W, bringing it much closer to the grid parity (14.0¢/kWh).

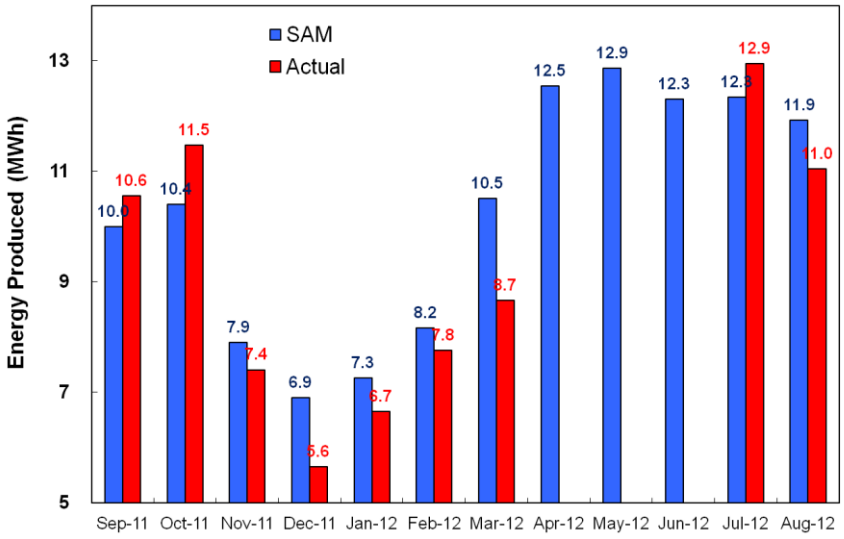

Figure A.2: Energy produced from 86.4 kW PV system on Clough Commons.

Table A.1: SAM simulation results.

LCOE nominal (¢/kWh)	24.36
LCOE real (¢/kWh)	19.52
Payback period (yr)	12.4
DC-to-AC capacity factor (%)	15.8
First year kWhac/kWdc	1383
System performance factor	0.77

REFERENCES

[1] M. Grubb, C. Vrolijk, and D. Brack, *The Kyoto Protocol: a guide and assessment*: Earthscan, 1999.

[2] B. Metz, *Climate change 2007: mitigation of climate change: contribution of Working Group III to the Fourth Assessment Report of the IIntergovernmental Panel on Climate Change*: Cambridge University Press, 2007.

[3] R. Dones and R. Frischknecht, "Life-cycle assessment of photovoltaic systems: results of Swiss studies on energy chains," *Progress in Photovoltaics: Research and Applications,* vol. 6, pp. 117-125, 1998.

[4] E. Nieuwlaar and E. Alsema, "Environmental aspects of PV power systems," *IEA PVPS Task,* vol. 1.

[5] D. E. Carlson, "Fossil fuels, the greenhouse effect and photovoltaics," *Aerospace and Electronic Systems Magazine, IEEE,* vol. 4, pp. 3-7, 1989.

[6] "SunShot Vision Study," U.S. Department of Energy2012.

[7] G. Barbose, "Tracking the Sun III; The Installed Cost of Photovoltaics in the United States from 1998-2009," 2011.

[8] A. Goodrich, T. James, and M. Woodhouse, "Residential, commercial, and utility-scale photovoltaic (PV) system prices in the United States: Current drivers and cost-reduction opportunities," National Renewable Energy Laboratory, Technical Report2012.

[9] Energy Information Administration (EIA) [Online]. Available: http://www.eia.gov/

[10] R. Hezel, "Plasma Si nitride-A promising dielectric to achieve high-quality silicon MIS/IL solar cells," *J. Appl. Phys.*, vol. 52, p. 3076, 1981.

[11] M. A. Green, *Solar Cells: Operating Principles, Technology and System Applications*. Kensington, NSW: The University of New South Wales, 1998.

[12] J. Schmidt, A. G. Aberle, and R. Hezel, "Investigation of carrier lifetime instabilities in Cz-grown silicon," in *Photovoltaic Specialists Conference, 1997., Conference Record of the Twenty-Sixth IEEE*, 1997, pp. 13-18.

[13] J. Schmidt and K. Bothe, "Structure and transformation of the metastable boron- and oxygen-related defect center in crystalline silicon," *Physical Review B*, vol. 69, p. 024107, 2004.

[14] N. Reich, W. van Sark, E. Alsema, S. Kan, S. Silvester, A. van der Heide, R. Lof, and R. Schropp, "Weak light performance and spectral response of different solar cell types," in *20th European Photovoltaic Solar Energy Conference*, Barcelona, Spain, 2005, pp. 2120-2123.

[15] G. E. Bunea, K. E. Wilson, Y. Meydbray, M. P. Campbell, and D. M. De Ceuster, "Low Light Performance of Mono-Crystalline Silicon Solar Cells," in *Photovoltaic Energy Conversion, Conference Record of the 2006 IEEE 4th World Conference on*, 2006, pp. 1312-1314.

[16] P. Grunow, S. Lust, D. Sauter, V. Hoffmann, C. Beneking, B. Litzenburger, and L. Podlowski, "Weak light performance and annual yields of PV modules and systems as a result of the basic parameter set of industrial solar cells," in *19th European Photovoltaic Solar Energy Conference*, Paris, France, 2004, pp. 2190-2193.

[17] E. Hecht and A. R. Ganesan, *Optics*, 4th ed.: Pearson Education, 2002.

[18] B. Hoex, "Ultralow surface recombination of c-Si substrates passivated by plasma-assisted atomic layer deposited Al2O3," *Appl. Phys. Lett.*, vol. 89, p. 042112, 2006.

[19] B. Hoex, "Silicon surface passivation by atomic layer deposited Al2O3," *J. Appl. Phys.*, vol. 104, p. 044903, 2008.

[20] P. Saint-Cast, J. Benick, D. Kania, L. Weiss, M. Hofmann, J. Rentsch, R. Preu, and S. W. Glunz, "High-Efficiency c-Si Solar Cells Passivated With ALD and PECVD Aluminum Oxide," *Electron Device Letters, IEEE*, vol. 31, pp. 695-697, 2010.

[21] J. Schmidt, A. Merkle, R. Brendel, B. Hoex, M. C. M. v. de Sanden, and W. M. M. Kessels, "Surface passivation of high-efficiency silicon solar cells by atomic-layer-deposited Al2O3," *Progress in Photovoltaics: Research and Applications*, vol. 16, pp. 461-466, 2008.

[22] V. Meemongkolkiat, "Development of high efficiency monocrystalline si solar cells through improved optical and electrical confinement," Georgia Institute of Technology, 2008.

[23] S. M. Sze, *Physics of Semiconductor Devices*, 2nd ed. New York, N.Y.: Wiley-Interscience, 1981.

[24] E. Lee, H. Lee, J. Choi, D. Oh, J. Shim, K. Cho, J. Kim, S. Lee, B. Hallam, S. R. Wenham, and H. Lee, "Improved LDSE processing for the avoidance of overplating yielding 19.2% efficiency on commercial grade crystalline Si solar cell," *Solar Energy Materials and Solar Cells,* vol. 95, pp. 3592-3595, 2011.

[25] K. R. Catchpole and A. W. Blakers, "Modelling the PERC structure for industrial quality silicon," *Solar Energy Materials and Solar Cells,* vol. 73, pp. 189-202, 2002.

[26] M. A. Green, K. Emery, Y. Hishikawa, W. Warta, and E. D. Dunlop, "Solar cell efficiency tables (version 39)," *Progress in Photovoltaics: Research and Applications,* vol. 20, pp. 12-20, 2012.

[27] M. A. Green, "Crystalline and thin-film silicon solar cells: state of the art and future potential," *Solar Energy*, vol. 74, pp. 181-192, 2003.

[28] R. Kyungsun, A. Upadhyaya, A. Das, S. Ramanathan, O. Young-Woo, H. Xu, L. Metin, A. Bhanap, and A. Rohatgi, "High efficiency n-type silicon solar cell with a novel inkjet-printed boron emitter," in *Photovoltaic Specialists Conference (PVSC), 2011 37th IEEE*, 2011, pp. 001131-001133.

[29] J. Zhao, A. Wang, and M. A. Green, "24·5% Efficiency silicon PERT cells on MCZ substrates and 24·7% efficiency PERL cells on FZ substrates," *Progress in Photovoltaics: Research and Applications*, vol. 7, pp. 471-474, 1999.

[30] P. Doshi, G. E. Jellison, and A. Rohatgi, "Characterization and optimization of absorbing plasma-enhanced chemical vapor deposited antireflection coatings for silicon photovoltaics," *Appl. Opt.*, vol. 36, pp. 7826-7837, 1997.

[31] S. C. W. Krauter, *Solar Electric Power Generation*: Springer, 1996.

[32] C.-C. Lee and C.-J. Tang, "TiO2-Ta2O5 composite thin films deposited by radio frequency ion-beam sputtering," *Appl. Opt.*, vol. 45, pp. 9125-9131, 2006.

[33] M. Sheoran, D. S. Kim, A. Rohatgi, H. F. W. Dekkers, G. Beaucarne, M. Young, and S. Asher, "Hydrogen diffusion in silicon from PECVD silicon nitride," in *Photovoltaic Specialists Conference, 2008. PVSC '08. 33rd IEEE*, 2008, pp. 1-4.

[34] A. K. Sinha, H. J. Levinstein, T. E. Smith, G. Quintana, and S. E. Haszko, "Reactive Plasma Deposited Si-N Films for MOS-LSI Passivation," *Journal of The Electrochemical Society*, vol. 125, pp. 601-608, 1978.

[35] M. A. Green, *High efficiency silicon solar cells*, 1986.

[36] M. H. Kang, K. Ryu, A. Upadhyaya, and A. Rohatgi, "Optimization of SiN AR coating for Si solar cells and modules through quantitative assessment of optical and efficiency loss mechanism," *Progress in Photovoltaics: Research and Applications*, vol. 19, pp. 983-990, 2011.

[37] P. Grunow and S. Krauter, "Modelling of the Encapsulation Factors for Photovoltaic Modules," in *Photovoltaic Energy Conversion, Conference Record of the 2006 IEEE 4th World Conference on*, 2006, pp. 2152-2155.

[38] S. O. Kasap, *Principles of Electrical Engineering Materials and Devices*: McGraw-Hill, 1997.

[39] A. Aberle, "Impact of illumination level and oxide parameters on Shockley?Read?Hall recombination at the Si?SiO2 interface," *J. Appl. Phys.*, vol. 71, p. 4422, 1992.

[40] J. Schmidt, A. Merkle, B. Hoex, M. C. M. van de Sanden, W. M. M. Kessels, and R. Brendel, "Atomic-layer-deposited aluminum oxide for the surface passivation of high-efficiency silicon solar cells," in *Photovoltaic Specialists Conference, 2008. PVSC '08. 33rd IEEE*, 2008, pp. 1-5.

[41] J. Schmidt, "Electronic properties of light-induced recombination centers in boron-doped Czochralski silicon," *J. Appl. Phys.*, vol. 86, p. 3175, 1999.

[42] K. Bothe, R. Sinton, and J. Schmidt, "Fundamental boron–oxygen-related carrier lifetime limit in mono- and multicrystalline silicon," *Progress in Photovoltaics: Research and Applications*, vol. 13, pp. 287-296, 2005.

[43] B. Lim, A. Liu, D. M. Fiacre Rougieux2, K. Bothe, and J. Schmidt, "BORON-OXYGEN-RELATED RECOMBINATION CENTERS IN COMPENSATED

SILICON," in *25th European Photovoltaic Solar Energy Conference*, Valencia, Spain, 2010.

[44] G. Coletti, C. Mulder, G. Galbiati, and L. Geerligs, "Reduced Effect of BO Degradation on Multicrystalline Silicon Wafers," in *21th European Photovoltaic Solar Energy Conference*, Dresden, Germany, 2006.

[45] P. Gilman, N. R. E. Laboratory, and S. N. Laboratories, *Solar advisor model user guide for version 2.0*: National Renewable Energy Laboratory, 2008.

[46] C. P. Cameron and A. C. Goodrich, "The levelized cost of energy for distributed PV: A parametric study," in *Photovoltaic Specialists Conference (PVSC), 2010 35th IEEE*, 2010, pp. 000529-000534.

[47] A. H. Ristow, "Numerical modeling of uncertainty and variability in the technology, manufacturing, and economics of crystalline silicon photovoltaics," Georgia Institute of Technology, 2008.

[48] M. H. Kang and A. Rohatgi, "Development and use of a simple numerical model to quantify the impact of key photovoltaics system parameters on the levelized cost of electricity," in *Photovoltaic Specialists Conference (PVSC), 2012 38th IEEE*, 2012, pp. 002932-002937.

[49] S. B. Darling, F. You, T. Veselka, and A. Velosa, "Assumptions and the levelized cost of energy for photovoltaics," *Energy Environ. Sci.*, vol. 4, pp. 3133-3139, 2011.

[50] K. Branker, M. J. M. Pathak, and J. M. Pearce, "A review of solar photovoltaic levelized cost of electricity," *Renewable and Sustainable Energy Reviews*, vol. 15, pp. 4470-4482, 2011.

[51] D. Powell, M. Winkler, H. Choi, C. Simmons, D. B. Needleman, and T. Buonassisi, "Crystalline silicon photovoltaics: a cost analysis framework for determining technology pathways to reach baseload electricity costs," *Energy Environ. Sci.*, 2012.

[52] H. Mäckel, "Detailed study of the composition of hydrogenated SiNx layers for high-quality silicon surface passivation," *J. Appl. Phys.*, vol. 92, p. 2602, 2002.

[53] M. Shibib, "Limitations on the open?circuit voltage imposed by P+ and N+ regions in silicon solar cells," *J. Appl. Phys.*, vol. 52, p. 1072, 1981.

[54] S. De Wolf, "Influence of stoichiometry of direct plasma-enhanced chemical vapor deposited SiNx films and silicon substrate surface roughness on surface passivation," *J. Appl. Phys.*, vol. 97, p. 063303, 2005.

[55] U. Goesele, P. Laveant, R. Scholz, N. Engler, and P. Werner, "Diffusion Engineering by Carbon in Silicon," *MRS Online Proceedings Library*, vol. 610, p. B7.1.1, 2000.

[56] R. Pinacho, "Carbon in silicon: Modeling of diffusion and clustering mechanisms," *J. Appl. Phys.*, vol. 92, p. 1582, 2002.

[57] B. Lim, S. Hermann, K. Bothe, J. Schmidt, and R. Brendel, "Permanent deactivation of the boron-oxygen recombination center in silicon solar cells," in *23rd European Photovoltaic Solar Energy Conference*, Valencia, Spain, 2008, pp. 1018-1022.

[58] R. C. Newman, "Carbon in Crystalline Silicon," *MRS Online Proceedings Library*, vol. 59, pp. 403-417, 1986.

[59] R. C. Newman, A. S. Oates, and F. M. Livingston, "Self-interstitials and thermal donor formation in silicon: new measurements and a model for the defects," *Journal of Physics C: Solid State Physics*, vol. 16, p. L667, 1983.

[60] A. R. Bean and R. C. Newman, "The effect of carbon on thermal donor formation in heat treated pulled silicon crystals," *Journal of Physics and Chemistry of Solids*, vol. 33, pp. 255-268, 1972.

[61] N. Magnea, "Luminescence of carbon and oxygen related complexes in annealed silicon," *Appl. Phys. Lett.*, vol. 45, p. 60, 1984.

[62] U. Gösele, K. Y. Ahn, B. P. R. Marioton, T. Y. Tan, and S. T. Lee, "Do oxygen molecules contribute to oxygen diffusion and thermal donor formation in silicon?," *Applied Physics A: Materials Science & Processing*, vol. 48, pp. 219-228, 1989.

[63] S. Hahn, "Effects of high carbon concentration upon oxygen precipitation and related phenomena in CzSi," *J. Appl. Phys.*, vol. 64, p. 849, 1988.

[64] J. Lu, "Impact of oxygen on carbon precipitation in polycrystalline ribbon silicon," *J. Appl. Phys.*, vol. 97, p. 033509, 2005.

[65] W. Taylor, "Carbon precipitation in silicon: Why is it so difficult?," *Appl. Phys. Lett.*, vol. 62, p. 3336, 1993.

[66] M. H. Kang, D. S. Kim, A. Ebong, B. Rounsaville, A. Rohatgi, G. Okoniewska, and J. Hong, "The Study of Silane-Free SiCxNy Film for Crystalline Silicon Solar Cells," *Journal of The Electrochemical Society*, vol. 156, pp. H495-H499, 2009.

[67] C. Ballif, D. M. Huijic, A. Hessler-Wyser, and G. Willeke, "Nature of the Ag-Si interface in screen-printed contacts: a detailed transmission electron microscopy study of cross-sectional structures," in *Photovoltaic Specialists Conference, 2002. Conference Record of the Twenty-Ninth IEEE*, 2002, pp. 360-363.

[68] M. B. EDWARDS, "Screen and stencil print technologies for industrial n-type silicon solar cells," University of New South Wales, 2008.

[69] M. M. Hilali, M. M. Al-Jassim, B. To, H. Moutinho, A. Rohatgi, and S. Asher, "Understanding the Formation and Temperature Dependence of Thick-Film Ag Contacts on High-Sheet-Resistance Si Emitters for Solar Cells," *Journal of The Electrochemical Society*, vol. 152, pp. G742-G749, 2005.

[70] M. M. Hilali, K. Nakayashiki, C. Khadilkar, R. C. Reedy, A. Rohatgi, A. Shaikh, S. Kim, and S. Sridharan, "Effect of Ag Particle Size in Thick-Film Ag Paste on the Electrical and Physical Properties of Screen Printed Contacts and Silicon Solar Cells," *Journal of The Electrochemical Society*, vol. 153, pp. A5-A11, 2006.

[71] A. Van der Heide, A. Schönecker, G. Wyers, W. Sinke, and E. C. N. S. Energy, "Mapping of contact resistance and locating shunts on solar cells using resistance analysis by mapping of potential (RAMP) techniques," in *16th European Photovoltaic Solar Energy Conference*, Glasgow, United Kingdom, 2000, pp. 1438-1442.

[72] R. Brendel, "Sunrays: a versatile ray tracing program for the photovoltaic community," in *12th European Photovoltaic Solar Energy Conference*, Amsterdam, Netherland, 1994.

[73] E. Yablonovitch, "Statistical ray optics," *J. Opt. Soc. Am.*, vol. 72, pp. 899-907, 1982.

[74] K. R. McIntosh, R. M. Swanson, and J. E. Cotter, "A simple ray tracer to compute the optical concentration of photovoltaic modules," *Progress in Photovoltaics: Research and Applications*, vol. 14, pp. 167-177, 2006.

[75] J. Schmidt, F. Werner, B. Veith, D. Zielke, R. Bock, V. Tiba, P. Poodt, F. Roozeboom, A. Li, and A. Cuevas, "Industrially relevant Al2O3 deposition techniques for the surface passivation of Si solar cells," in *25th European Photovoltaic Solar Energy Conference*, Valencia, Spain, 2010.

[76] R. Sinton and A. Cuevas, "A quasi-steady-state open-circuit voltage method for solar cell characterization," in *16th European Photovoltaic Solar Energy Conference*, 2000, pp. 1-5.

[77] S. C. Baker-Finch and K. R. McIntosh, "The contribution of planes, vertices, and edges to recombination at pyramidally textured surfaces," *Photovoltaics, IEEE Journal of*, vol. 1, pp. 59-65, 2011.

[78] "Solar Energy Technologies Program: Multi-Year Program Plan 2007-2011," U.S. Department of Energy2007.

[79] S. Price, "2008 Solar Technologies Market Report," 2010.

[80] A. Luque and S. Hegedus, *Handbook of photovoltaic science and engineering*: Wiley, 2010.

[81] X. Deng and E. A. Schiff, "Amorphous silicon–based solar cells," *Handbook of Photovoltaic Science and Engineering*, pp. 505-565, 2003.

[82] D. L. King, J. A. Kratochvil, and W. E. Boyson, *Photovoltaic array performance model*: United States. Department of Energy, 2004.

[83] *PVWatts*. Available: http://www.nrel.gov/rredc/pvwatts/

[84] Greentechmedia, "German Solar Installations Coming In at $2.24 per Watt Installed, US at $4.44," E. Wesoff, Ed., ed, 2012.

[85] United States Inflation Rate [Online]. Available: http://www.tradingeconomics.com/united-states/inflation-cpi

PUBLICATIONS FROM THIS WORK

JOURNAL PUBLICATIONS:

1. **M. H. Kang**, D. S. Kim, A. Ebong, B. Rounsaville, A. Rohatgi, G. Okoniewska, and J. Hong, "The Study of Silane Free Silicon Carbon Nitride (SiC_xN_y) Film as Antireflection Coating, Surface and Bulk Passivation for Silicon Solar Cells", Journal of The Electrochemical Society, Vol. 156, Issue 6, pp. H495 (2009)

2. **Moon Hee Kang**, Junegie Hong, Ian Cooper, Abasifreke Ebong, Brian Rounsaville, and Ajeet Rohatgi, "Reduction in Light Induced Degradation (LID) in B-doped Cz-Si solar cells with SiC_xN_y antireflection (AR) coating", Journal of The Electrochemical Society, Vol. 158, Issue 7, pp. H724 (2011)

3. **Moon Hee Kang**, Kyungsun Ryu, Ajay Upadhyaya, Ajeet Rohatgi, "Optimization of SiN AR coating for Si Solar cells and modules through quantitative assessment of optical and efficiency loss mechanism", Progress in Photovoltaics: Research and Applications, Vol. 19, Issue 8, pp. 983, (2011)

4. **Moon Hee Kang**, Ajeet Rohatgi, Junegie Hong, Brian Rounsaville, Vijaykumar Upadhyaya, and Abasifreke Ebong, "Effect of carbon containing SiN_x antireflection coating on the screen-printed contact and low illumination performance of silicon solar cell", Progress in Photovoltaics: Research and Applications, DOI: 10.1002/pip. 1184 (2011)

5. Kyungsun Ryu, A. Upadhyaya, Y.-W. Ok, **Moon Hee Kang**, V. Upadhyaya, L. Metin, H. Xu, A. Bhanap, and A. Rohatgi, "High Efficiency N-type Si Solar Cells With Novel Inkjet-printed Boron Emitters", IEEE Electron Device Letters, Vol. 33, Issue 6, pp. 854 (2012)

6. Ian B. Cooper, Keith Tate, **Moon Hee Kang**, Alan F. Carroll, Kurt R. Mikeska, Robert C. Reedy, and Ajeet Rohatgi, "Development of $POCl_3$ Emitters which Enable Ag

Reduction while Increasing Cell Efficiency: Assessing the Impact on Manufacturing and System Costs", Photovoltaics International, 18th Edition, pp. 41 (2012)

7. Chia-Wei Chen, **Moon Hee Kang**, Vijaykumar Upadhyaya, Aditya Kapoor, Keith Tate, Jim Keane, Steven Ning, and Ajeet Rohatgi, "Understanding and Development of Screen-Printed Front Metallization for High Efficiency Low to Medium Concentrator Silicon Solar Cells", IEEE Journal of Photovoltaics – Accepted (2012)

8. **Moon Hee Kang**, Ajeet Rohatgi, and Alan Ristow, "Development of a Simple Analytical Model to Quantify the PV Module Cost Premium Associated with Module Efficiency and Cell Technology", Renewable & Sustainable Energy Reviews – Submitted (2012)

9. **Moon Hee Kang** and Ajeet Rohatgi, "Quantitative Analysis of Levelized Cost of Electricity (LCOE) of Commercial Scale Photovoltaics System", Progress in Photovoltaics: Research and Applications – Submitted (2013)

CONFERENCE PROCEEDINGS:

1. D. S. Kim, **M. H. Kang**, B. Rounsaville, A. Ristow, A. Rohatgi, Y. Awad, G. Okoniewski, A. Moore, M. Davies, R. Smirani, M. A. El Khakani, and J. Hong, "High performance solar cells with silicon carbon nitride (SiC_xN_y) antireflection coatings deposited from polymeric solid source," in Photovoltaic Specialists Conference (PVSC), 33rd IEEE, pp. 1-4 (2008)

2. J. Renshaw, **M. H. Kang**, V. Meemongkolkiat, A. Rohatgi, D. Carlson, and M. Bennett, "3D-modeling of a back point contact solar cell structure with a selective emitter," in Photovoltaic Specialists Conference (PVSC), 34th IEEE, pp. 000375-000379 (2009)

3. **M. H. Kang**, A. Ebong, B. Rounsaville, A. Rohatgi, and J. Hong, "Silane-free PECVD silicon carbon nitride (SiC_xN_y) passivation and anti-reflection coatings for high efficiency

silicon solar cells," in Photovoltaic Specialists Conference (PVSC), 34th IEEE, pp. 001724-001726 (2009)

4. **M. H. Kang**, A. Ebong, B. Rounsaville, A. Rohatgi, and J. Hong, "Optimization of Silane Free PECVD SiC_xN_y as Passivation and Antireflection Coating of Silicon Solar Cell", in 24th European Photovoltaic Solar Energy Conference, Hamburg, Germany, pp. 369 - 372 (2009)

5. **M. H. Kang**, J. Hong, A. Ebong, B. Rounsaville, V. Upadhyaya, and A. Rohatgi, "Reduction of light induced degradation (LID) in B-doped Cz-Si solar cells by SiH_4-free SiC_xN_y film," in Photovoltaic Specialists Conference (PVSC), 35th IEEE, pp. 003196-003199 (2010)

6. J. Hong, **M. H. Kang**, A. Ebong, B. Rounsaville, M. Davies, G. Okoniewska, X. Yang, S. Navala, and A. Rohatgi, "Simple and cost-effective reduction of light induced degradation in B-doped Cz-Si solar cells by Silexium PECVD SiCN antireflective passivation coatings", in 25th European Photovoltaic Solar Energy Conference, Valencia, Spain, pp. 1200-1204 (2010)

7. **Moon Hee Kang** and Ajeet Rohatgi, "Development and Use of a Simple Numerical Model to Quantify the Impact of Key Photovoltaics System Parameters on the Levelized Cost of Electricity", in Photovoltaic Specialists Conference (PVSC), 38th IEEE, pp. 002932-002937 (2012)

VITA

Moon Hee Kang was born on June 13, 1979 in South Korea. He received Bachelor degree in Electrical Engineering from Korea University, Seoul, in 2005 and Master degree in Electrical and Computer Engineering from University of Florida, FL in 2007. After completing his master degree, he started work on his Doctorate in Electrical and Computer Engineering at Georgia Institute of Technology, GA, where he joined the University Center of Excellence for Photovoltaics Research and Education as a Graduate Research Assistant under advisory from Dr. Ajeet Rohatgi. He is also trainer at the Institute for Electronics and Nanotechnology, Georgia Institute of Technology, GA. His research focused on fabrication and modeling of high-efficiency silicon solar cells. During his research, he produced over 15 technical papers in the prestigious journals and proceedings.